Vertical dependences

In swash-zone flows and sand transport

Vertical dependences in swash-zone flows and sand transport

Joost W.M. Kranenborg

Joost W.M. Kranenborg

Invitation

For the public defense of my PhD dissertation

Vertical dependences in swash-zone flows and sand transport

Thursday 29 June, 2023
10:30

Location:
Prof.dr. G. Berkhoffzaal
De waaier
University of Twente

Joost Kranenborg
joost.kranenborg@gmail.com

Paranymphs:
Wessel van der Sande
Felix Agner

Propositions

accompanying the dissertation

Vertical dependences in swash-zone sand transport

by

Joost Willem Martijn Kranenborg

1. Specialized knowledge based on experience is necessary to correctly apply, maintain, and develop detailed CFD models.
2. It has been found that during years of research on sand transport, one can be primarily engaged with water and air.
3. To improve depth-averaged model predictions of suspended sand transport in the swash zone, the effects of turbulence and vertical variability in flow and sand concentrations are essential.
4. Model calibration must be physically supported, otherwise it can obscure the interpretation of results and unjustifiably instil confidence in the model predictions.
5. Investments in natural science and technical education and research should not be funded by cuts in the humanities and social sciences.
6. The notion that we should solve the climate crisis through individual responsibility has been the most successful marketing strategy employed by companies in the oil, gas, and bio-industries.
7. It is puzzling that the Dutch consume so much bread when Dutch bread lacks character and flavour.

These propositions are regarded as opposable and defendable,
and have been approved as such by the promotors
prof. dr. S.J.M.H. Hulscher and prof. dr. ir. A.J.H.M. Reniers.

Stellingen

behorende bij het proefschrift

Vertical dependences in swash-zone sand transport

door

Joost Willem Martijn Kranenborg

1. Specialistische kennis gebaseerd op ervaring is noodzakelijk om gedetailleerde CFD modellen correct toe te passen, te onderhouden en te ontwikkelen.
2. Gebleken is dat je in ruim vier jaar onderzoek naar zandtransport toch vooral met water en lucht bezig kan zijn.
3. Om dieptegemiddelde modelvoorspellingen van suspensief zandtransport in de swash zone te verbeteren zijn de effecten van turbulentie en verticale variabiliteit van de stroming en zandconcentraties essentieel.
4. Kalibratie van modellen moet fysisch onderbouwd zijn, anders kan het de interpretatie van resultaten vertroebelen en misplaatst vertrouwen geven in de modelvoorspellingen.
5. Investeringen in natuurwetenschappelijk en technisch onderwijs en onderzoek moeten niet bekostigd worden door bezuinigingen in de geestes- en sociale wetenschappen.
6. De gedachte dat we met eigen verantwoordelijkheid de klimaatcrisis zouden moeten oplossen is de beste marketingslag geweest van bedrijven in de olie-, gas- en bio-industrie.
7. Het is een raadsel dat Nederlanders zo veel brood eten terwijl Nederlands brood zo weinig karakter en smaak heeft.

Deze stellingen worden opponeerbaar en verdedigbaar geacht
en zijn als zodanig goedgekeurd door de promotoren
prof. dr. S.J.M.H. Hulscher en prof. dr. ir. A.J.H.M. Reniers.

VERTICAL DEPENDENCES IN SWASH-ZONE FLOWS AND SAND TRANSPORT

Joost Willem Martijn Kranenborg

Vertical dependences in swash-zone flows and sand transport

DISSERTATION

to obtain
the degree of doctor at the University of Twente,
on the authority of the Rector Magnificus
Prof. dr. ir. A. Veldkamp,
on account of the decision of the graduation committee,
to be publicly defended
on Thursday June 29, 2023 at 10:45

by

Joost Willem Martijn Kranenborg

born on the 22nd of April, 1994
in Utrecht, The Netherlands

This dissertation has been approved by:

Supervisors:

prof. dr. S.J.M.H. Hulscher

prof. dr. ir. A.J.H.M. Reniers

Co-supervisors:

dr. ir. J.J. van der Werf

dr. ir. G.H.P. Campmans

Cover: Frans Baake with input from Anne Baake en Joost Kranenborg, Enschede 2023.
Printed by: Ipskamp printing (ipskampprinting.nl)
Layout: Joost kranenborg
ISBN (print): 978-90-365-5684-2
ISBN (digital): 978-90-365-5685-9
DOI: 10.3990/1.9789036556859

Graduation committee:

Chair/Secretary:

prof. dr. ir. H.F.J.M. Koopman
University of Twente

Supervisors:

prof. dr. S.J.M.H. Hulscher
University of Twente

prof. dr. ir. A.J.H.M. Reniers
Delft University of Technology

Co - Supervisors:

dr. ir. J.J. Van der Werf
University of Twente & Deltares

dr. ir. G.H.P. Campmans
University of Twente

Committee members:

prof. dr. K.M. Wijnberg
University of Twente

prof. dr. A.R. Thornton
University of Twente

prof. dr.-ing. N. Goseberg
Technische Universität Braunschweig

prof. N. Dodd
University of Nottingham

dr. M.F.S. Tissier
Delft University of Technology

Contents

Preface

It was during my exchange semester in 2017 that I decided I wanted to pursue a PhD. I was attending courses on numerical analysis, fluid dynamics and nonlinear dynamical systems and thought that the intersection between advanced mathematical techniques and practical applications would be an attractive academic field to work in. While I was working on my Msc thesis, an intriguing PhD position at the University of Twente caught my eye. The advert mentioned familiar topics, such as computational fluid dynamics, but also unfamiliar terminology such as "swash zone". The last five years were spent on unravelling the complexities of both these topics, or at least to give it a try. This is something that I would not have managed on my own. I'd like to reserve a page or two about you who made this such an unforgettable and so thoroughly enjoyable experience for me.

Ten eerste mijn begeleiders! Ik wil jullie heel erg bedanken voor het vertrouwen in mij en de tijd en steun die jullie mij gegeven hebben tijdens dit onderzoek. Suzanne, bedankt voor het vertrouwen dat je in me had om dit onderzoek te doen. Ook tijdens periodes wanneer het onderzoek moeizaam verliep was jouw vertrouwen, trots en optimisme een bron van energie om door te zetten. Ad, superbedankt voor de goede feedback en kritiek die altijd zeer scherp maar ook uiterst vriendelijk gegeven was. Jouw kennis over golf- en swashprocessen zijn cruciaal gebleken. Daarnaast kan ik me geen beter persoon bedenken om een zomerschool zo goed en vol gezelligheid te organiseren. Jebbe, bedankt voor alle goede overleggen en inhoudelijke gesprekken. Jij was altijd enthousiast om mijn resultaten te bespreken. Wat mij echter het meeste bij zal blijven is hoe jij zag waar ik goed in was en waar ik mijn plezier uit haalde in mijn werk. Daar heb je me heel erg mee gesteund en dat waardeer ik echt superveel! Geert, als dagelijks begeleider heb ik jou het meest gesproken. Je nam altijd de tijd voor me, ook als je die eigenlijk niet echt had. Je hebt veel en zeer preciese feedback geleverd op al mijn werk, met aanzienlijk beter geschreven publicaties tot gevolg. Ook was het heel fijn om iemand op de gang te hebben die mijn interesse in de wat fundamentelere kant van de natuur- en wiskunde deelde. Het moet ook niet altijd alleen maar over de toepassing gaan...

Apart from my supervisors, I would also like to thank everyone else involved in the Shaping the Beach project. Sara, thank you for being my partner in PhD, letting me taste Portuguese cuisine and sharing the brunt of the research burden together. Thank you Weiqiu for the OpenFOAM collaborations and for picking up the swash zone sediment research on larger scales. I'd also like to express my

gratitude towards all the users, especially Joep and Robert, who gave their input on my research. Finally, thank you Niels for all the support and time you reserved for me. I thoroughly enjoyed working together with you. After every meeting with you I felt that I had made leaps of progress. Without you this project would simply not have been possible. Your confidence in me was one of my key sources of inspiration.

I want to thank all colleagues and friends at the Water Engineering and Management group. Bedankt Anke, Dorette, Dominique en Joke voor alle ondersteuning, de lekkere koffie en de leuke gesprekken. Bedankt Vera voor de leuke samenwerking rondom OpenFOAM en de gezellige koffiepauzes. Wessel, Daan en Koen, bedankt voor de biertjes en de spelletjesavonden. Dank Mathijs voor de coronaafleidende wandelingen en politieke discussies. Thanks all my roomies Sara, Yared, Koen, Fatemeh, Harriëtte en Wout for all the chats. Pauline, Rutger en Rik, superbedankt voor de fantastische vakantie in Australië, en het niet-filmen terwijl ik door een emu achterna werd gezeten.

Luckily, I had many hobbies and friends who distracted me from productivity. Abba had it right: "Thank you for the music"! Ik wil graag heel Vocaal Ensemble Cordier bedanken voor de fantastische repetities en de supermooie concerten. Samen zingen met jullie is het mooiste wat er is. Daarnaast heeft de uit het koor ontstane eetclub met Jurriaan, Sebas en Irene ook aan de culinaire behoefte voldaan. Met jullie voelden de eerste coronamaanden een stuk minder eenzaam (al dan niet wat zwaarder op de maag). Enschede also taught me some new skills. Who would've thought that throwing plastic would be this much fun! Thank you Disc Devils Twente for the many trainings, competitions, tournaments and the beers in the park. Rino, Enno en Jesse, laten we nog eens een strandtournooi aan de Middellandse zee spelen!

Lieve familie, bedankt voor de lieve kaartjes, vele telefoongesprekken, krantenknipsels, sushi-avonden, barbecues, discussies over autobanden, en de betrokkenheid bij mijn onderzoek. In het bijzonder bedankt Papa, Mama, Bart en Pieter voor de gezelligheid; geen ander woord vat het beter samen denk ik.

Als allerlaatst maar ook allerliefst, mijn Anne. Jou leren kennen was het absolute hoogtepunt van de afgelopen jaren. Al had ik het druk of liep het onderzoek weer eens niet goed, dat deed er niet meer toe als ik bij jou was. We hebben al zo veel leuks samen beleefd. Samen met jou de toekomst ingaan is de fijnste gedachte die er is.

Samenvatting

Stranden zijn zeer dynamische gebieden en bewegen aanzienlijk onder invloed van golven, stromingen en getijden. De resulterende verandering van de vorm van de kust, de kustmorfodynamica, heeft belangrijke gevolgen voor de veiligheid van nabijgelegen steden en dorpen, maar ook voor kustecosystemen en menselijke recreatie. Het is daarom van belang om kustprocessen goed te begrijpen en de kustmorfodynamica te kunnen voorspellen.

De swashzone is het gebied van het strand waar de golven op het strand heen en weer bewegen. Deze zone wordt gekenmerkt door sterke stromingen, veel turbulentie en intensieve sedimenttransporten. Aangezien de swashzone de grens vormt tussen land en zee, is het cruciaal om de morfodynamica van dit gebied te doorzien als men de ontwikkeling van het strand en de kust als geheel wil begrijpen.

Toegepaste waterbouwkundige modellen die zijn ontworpen voor simulaties op de schaal van kilometers of groter hebben moeite om de morfodynamica in de swashzone te voorspellen. Dit komt doordat ze de dynamiek in dit gebied niet in voldoende detail kunnen beschrijven. Deze modellen berekenen alleen het indirecte gemiddelde effect van golven waarbij ze gebruik maken parametrisaties. In de praktijk blijkt dat deze aanpak de complexiteit van de swashzone niet voldoende kan beschrijven en hebben deze modellen de neiging om erosie te overschatten.

In plaats van deze golfgemiddelde modellen worden golfoplossende modellen doorgaans gebruikt voor het bestuderen van de dynamiek van de swashzone. Deze modellen kunnen wel direct de individuele golven en swashstroming beschrijven, maar hebben meer rekenkracht en langere rekentijden nodig. De meeste modellen die hiervoor gebruikt worden zijn zogenaamde dieptegemiddelde modellen. Deze modellen kunnen niet expliciet de verticale variatie in snelheid en sedimentconcentratie modelleren. In plaats daarvan modelleren ze de gemiddelde snelheid en gemiddelde sedimentconcentratie over de diepte en passen ze parametrisaties voor de bodemwrijving en sedimentopname en afzetting toe. Deze aanpak is echter verre van nauwkeurig voor de swashzone, waar verticale afhankelijkheden in sedimentconcentratie en stroming van groot belang kunnen zijn.

Het hier beschreven onderzoek heeft als doel verticale afhankelijkheden beter te begrijpen door zowel gedetailleerde numerieke modellering als gecontroleerde laboratoriumexperimenten te gebruiken. Wat betreft de modellering is een zogenaamd diepteoplossend model gebouwd. Een dergelijk model kan variaties in de verticale richting van de verdeling van stroming, turbulentie en sediment in

detail beschrijven. Dit diepteoplossend model werd eerst toegepast op een relatief eenvoudig geval van een enkele golf (Hoofdstuk 2) zonder interactie met meerdere golven. Hiervoor werd de modelcode OpenFOAM® aangepast om op de juiste manier om te gaan met het in suspensie brengen van sediment aan de bodem. De resultaten van het model tonen aan dat de stroming en sedimentconcentraties in de swashzone verre van verticaal uniform zijn.

De verticale structuren werden vervolgens in meer detail bestudeerd voor een bichromatische golf in Hoofdstuk 3. Bichromatische golven (twee golven die verschillende frequenties en golfhoogtes hebben) maken het mogelijk om complexere stromingsfenomenen te bestuderen die zich voordoen wanneer binnenkomende golven inwerken op de stroming in de swashzone in zogenaamde golf-swashsinteracties. Dit hoofdstuk toont aan dat verticale structuren zeer belangrijk zijn om rekening mee te houden, anders kan het sedimenttransport met ongeveer de helft worden overschat. Dit is belangrijker in de swashzone dan de brandingszone waar de stromingen en turbulentie veroorzaakt door brekende golven het sediment effectief verticaal mengen. De dieptegemiddelde aanpak lijkt dus meer geldig in de brandingszone dan in de swashzone. Verder is ook onderzocht welke rol de door golfbreking veroorzaakte turbulentie speelt en hoe dit gemodelleerd kan worden. Bovendien werd vastgesteld dat luchtbellen in 2DV-simulaties te lang dicht bij de bodem blijven. Deze bellen zorgen voor veel lagere wrijving tussen de bodem en de stroming en verhinderen sediment om in suspensie te komen. Wanneer deze bellen werden verwijderd en golfbrekingsturbulentie werd gemodelleerd, verbeterden de voorspellingen van sedimentconcentratie aanzienlijk.

Tot slot beschrijft Hoofdstuk 4 de verticale veranderlijkheid van de bodemdruk. Deze drukgradiënten kunnen de mobiliteit van sedimentkorrels verhogen of verlagen. Om de drukgradiënten te bestuderen werden grootschalige golfbakexperimenten uitgevoerd met druksensoren in de bodem. Vervolgens werd met behulp van de gemeten gegevens een analytisch model toegepast om drukgradiënten aan het oppervlak van de bodem te berekenen. Deze berekeningen toonden aan dat drukgradiënten het effectieve gewicht van de zandkorrels tijdens de stroming aanzienlijk verhogen, waardoor het sedimenttransport wordt belemmerd. Het tegenovergestelde gebeurt tijdens het terugspoelen.

Het in dit proefschrift beschreven onderzoek toont het belang van gedetailleerde processen met betrekking tot verticale structuren in de swash zone. Het toont verder de bruikbaarheid aan van gedetailleerde modellen en grootschalige golfbakexperimenten voor het onderzoeken van gedetailleerde swashprocessen.

Summary

Beaches are highly dynamic regions and move substantially under the force of waves, currents and tides. These changes of the coastline, the coastal morphodynamics, have important implications not only the safety of coastal communities, but also for coastal ecosystems and human recreation. Therefore, it is important to understand coastal processes and be able to predict coastal morphodynamics.

The swash zone is the region where waves run up and down the beach, and is characterised by strong flows, presence of high amounts of turbulence and large sediment transport rates. As the swash zone forms the boundary between land and sea, it is crucial to understand the morphodynamics of this region if one wants to understand the morphodynamics of the beach overall.

Currently, practical engineering models, made for large-scale simulations on the order of kilometres or larger, have difficulty predicting the correct morphodynamics in the swash zone as they cannot resolve the dynamics in this region sufficiently. For instance, such models do not resolve individual waves. Instead, they rely on parametrisations of these detailed processes. However, even with parametrisations, these models tend to overpredict erosion and have difficulty modelling accretive conditions.

Because of this, wave-resolving models that can resolve the individual waves and swash events are typically used for studying the dynamics of the swash zone. The most commonly used swash-model are depth-averaged. These models do not explicitly model the vertical variation in velocity and sediment concentration. Instead, they model the evolution of these quantities averaged over depth and apply parametrisations of the bed friction and sediment erosion pickup and deposition based on assumptions of the vertical structures. However, these assumptions are far from accurate for the swash zone, where vertical dependences in sediment concentration and flows are present.

This thesis aims to understand such vertical processes better by the use of both detailed numerical modelling and controlled laboratory experiments. As for the modelling, a depth-resolving model is built. Such a model can explicitly resolve variations in the vertical direction and as such does not need to make assumptions on the vertical distribution of flow, turbulence and sediment. This depth-resolving model was first applied to a relatively simple solitary wave (Chapter 2) wave case without wave-swash interactions. To do this, the model code OpenFOAM® was improved to correctly deal with sediment suspension at the bed. The model results

showed that the flow and sediment concentrations in the swash zone were indeed not vertically uniform.

The vertical structures were further studied in more detail for a bichromatic wave case in Chapter 3. Bichromatic waves allowed for studying more complex flow phenomena that happen when incoming waves interact with the swash in so-called wave-swash interactions. This chapter shows that vertical structures are very important to account for, otherwise the sediment transport can be overpredicted by approximately 50%. This is especially important in the swash zone compared to the surf zone, where the currents and turbulence induced by the breaking waves effectively mix the sediment vertically, making the uniform assumption more valid in this region. Apart from these conclusions, the role of wave-breaking induced turbulence and how this can be modelled was investigated. Also, it was found that bubbles tend to linger close to the bed for too long in 2DV simulations. These bubbles lead to much lower friction between the bed and the flow and also inhibit sediment pickup. When these bubbles were removed and wave-breaking turbulence was modelled, sediment concentration predictions improved significantly.

Finally, Chapter 4 investigates pore pressure gradients in the soil. These pressure gradients can influence sediment grains and increase or decrease their mobility. To study the pressure gradients, large-scale flume experiments were conducted with pressure sensors within the bed. An analytical model was then fitted to the measured data, and was subsequently used to calculate pressure gradients at the bed surface. These calculated pressure gradients showed that pressure gradients significantly increase the effective weight of particles during the uprush, thereby inhibiting sediment transport. The opposite happens during the backwash.

Overall, this thesis shows the importance of detailed processes concerning vertical structures. It further demonstrates the usefulness of detailed depth-resolving models and large-scale wave-flume experiments in investigating detailed swash processes.

Chapter 1

Introduction

Figure 1.1
Washaway beach in Sydney, photo by the author.

1.1 Background

Sandy beaches make up a substantial part of the world's coastlines. These beaches are dynamic regions, continually hit by waves and tides. These conditions can induce strong currents and lead to large amounts of sediment being transported. Figure 1.1 shows a view of Washaway beach in Sydney, Australia. It shows some important coastal processes. For instance, the breaking waves lead to large amounts of air bubbles, presenting themselves as the regions of white water. Furthermore, the photo also shows the turbulent and nonuniform nature of the flow on the beach. Lastly, and perhaps most relevant for this thesis, there is a pronounced difference between the colour of the water further from the beach, which is a clear blue hue, and closer to the beach, which shows a brown colour from all the sand suspended in the water.

Sand (sometimes referred to as sediment in this thesis) can move between different regions along the coast, but also across the profile leading to erosion or accretion of the beach. Making accurate predictions of the morphodynamics of the coast is paramount for a variety of reasons. For instance, coastal erosion can jeopardize the safety of people living near the coast. Furthermore, the coastal

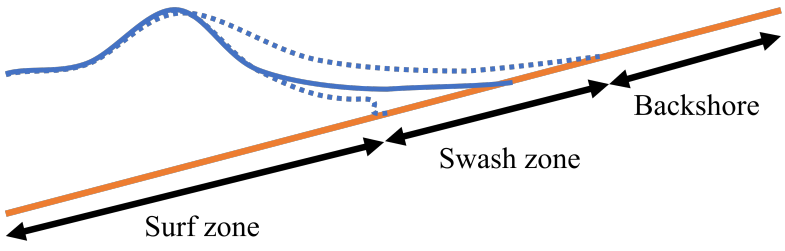

Figure 1.2
Schematic overview of the different cross-shore regions of the beach. The dashed lines show the minimum and maximum runup.

region is an important habitat for many animal and plant species. Also, the beach provides a place for recreation. Changes to the coastline can have a large impact on these stakeholders, nature included. Therefore, it is of great interest to understand how the beach evolves and develops over time.

To this end, it is important to be able to predict the development of the beach. There are multiple practical engineering tools available in the form of numerical models for this purpose. These models are comparatively efficient and applicable for spatially large-scale simulations. Here, large-scale refers to simulations on the order of hundreds of metres, kilometres or longer and a timescale of days, months or longer. Due to their application to large-scale problems, these models do not resolve individual waves and thus cannot resolve the more detailed and small-scale processes happening on the beach. Instead, these models use parameterisations to calculate wave-averaged sediment transport and morphodynamics. At present, these large-scale models have great difficulty in providing sufficiently accurate predictions of beach morphodynamics, especially regarding cross-shore transport at the boundary between the sea and the dry coast (Van Rijn et al., 2011). To improve these practical models, better parameterisations for sediment transport and morphodynamics are needed. However, to get there, we first need to improve our fundamental understanding of the small-scale processes driving sediment transport in the swash zone.

1.2 The swash zone

Figure 1.2 shows a schematic overview of the different cross-shore zones of the beach. This thesis focusses on cross-shore transport in this upper region of the beach, specifically the swash zone. This is the part of the beach that is alternately covered and exposed by the incoming waves. Further offshore, the swash zone is connected to the surf zone. This is the region where waves break, generating alongshore currents and sand transport. Further onshore of the swash zone, sediment transport is dominated by aeolian (wind driven) transport. As such, the connection between the submerged and exposed parts of the beach makes the swash zone an important region for understanding coastal sediment transport in general.

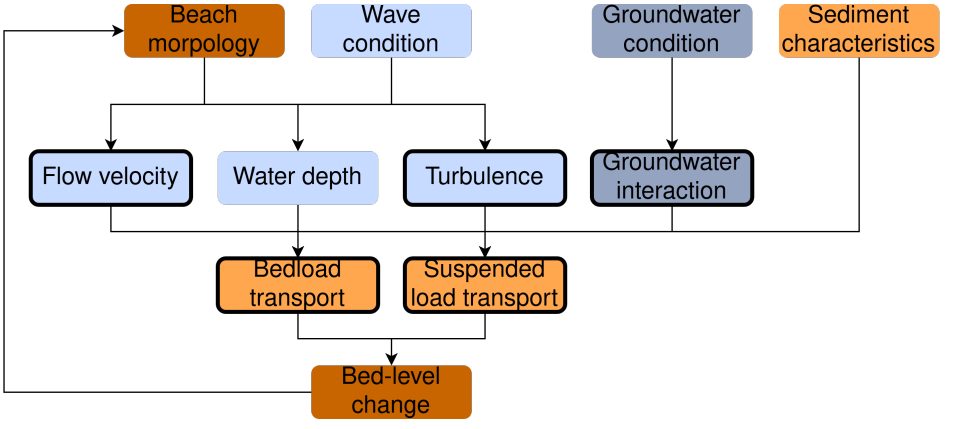

Figure 1.3
Conceptual model showing a simplified overview of important swash-zone processes and characteristics. Light blue boxes show hydrodynamic quantities and processes, orange boxes relate to sediment, brown boxes relate to morphology and grey-blue boxes relate to groundwater processes. Boxes with a thick boundary are processes and characteristics where vertical structures are present that are investigated in this thesis.

Figure 1.3 shows a conceptual model of the morphodynamics of the swash zone. The dynamics in the swash zone are mainly driven by incoming waves. These waves interact in the swash zone to generate the up-and-down swash motion. This motion is usually characterised by two phases. The uprush phase is the period of the swash where the water moves up the beach. This is followed by the backwash (sometimes called downrush) which is the period where water runs down the beach back towards the sea. After the backwash, a new uprush forms and the swash cycle starts again. The hydrodynamics of these swash cycles is highly dependent on the characteristics of the incoming waves, such as the wave height, wavelength, wave skewness and wave asymmetry, but also beach properties such as the slope. Furthermore, complex interactions can happen when a wave reaches the swash zone and interacts with a backwash from a previous wave.

Apart from the aforementioned wave properties, other beach properties such as the beach morphology, sediment properties and interactions with groundwater are also important (Wright and Short, 1984; Horn, 2002). All these characteristics influence the swash flow properties such as the velocities, water depths and turbulence. These hydrodynamic conditions form the basis for the transport of sediment. This transport is induced by hydrodynamic drag and lift forces acting on the sediment. Generally, the higher the water velocities and turbulence levels the more sand is being transported.

Coastal sediment transport is often characterised into two modes, namely bedload and suspended load transport. Bedload transport refers to the movement of sediment particles along the bed surface. These particles move by rolling or saltating along the bed, or when the flow is strong, can move in a dense layer near the bed called sheet flow. Suspended sediment transport refers to sediment

particles that are transported whilst held in suspension in the flow. These particles are kept in suspension by turbulent mixing and fall back to the bed due to gravity. The balance between the mobilising effect of turbulent mixing and gravitational settling determines the amount of suspended material in the water column. Finally, gradients in sediment transport lead to a change in the bed level, which closes the morphodynamic system.

Additionally, interactions with the groundwater are also important to consider. Especially for larger particle sizes, the porous space between particles can let water flow through (Masselink and Li, 2001). For smaller grain sizes other effects become important. For instance, the flow velocity and levels of turbulence in the bed boundary layer change in the presence of infiltration and exfiltration (Conley and Inman, 1994; Lohmann et al., 2006). Furthermore, pressure gradients in the bed can lead to increased or decreased sediment mobility (Baldock and Holmes, 1998).

Some of the processes and characteristics described above are not vertically uniform over the water column. For instance, wave-related velocities are typically higher near the free surface than near the drag-inducing bed. Similarly, sediment concentrations are generally higher near the bed compared with concentrations near the free surface. This is true both for suspended load (Puleo et al., 2000) as well as bedload in the form of sheet flow (Lanckriet and Puleo, 2015). Similarly, turbulence levels can vary vertically depending on the effects of wave-breaking and bed friction (Van der Zanden et al., 2016).

Finally, it is important to consider the fact that the swash zone presents strong variability on both long and short timescales. For instance, the location of the swash zone depends on wave and tidal conditions. On shorter timescales, large quantities of sediment are moved instantaneously (Masselink and Puleo, 2006) and the bed level can change centimetres in seconds (Van der Zanden et al., 2015).

1.3 Research and model approaches

One way of acquiring detailed insights is to conduct measurements, both in the field and in the lab. Such studies have led to important insights into sediment transport and morphodynamics, such as the importance of turbulence due to the presence of breaking waves (Butt et al., 2004), the influence of wave skewness and asymmetry as well as bed slope on sediment transport and morphodynamics (Walstra et al., 2007; Van Rijn et al., 2013) or the importance of infiltration and subaqueous processes on sediment transport (Horn, 2006). However, it is difficult to measure all the detailed dynamics through experiments alone due to the strong currents, turbulence, a moving bed and presence of air bubbles (Masselink and Puleo, 2006). Provided that numerical tools show sufficient model skill, they complement measurements with more detailed insights into important processes. Furthermore, such models provide the opportunity to do detailed parameter studies. Also, their process-based nature means that they provide explanatory power in addition to their results.

There exist different types of numerical models for modelling morphodynamics. Because many important swash processes happen at short time-scales, this thesis

limits itself to models capable of resolving intraswash dynamics. Therefore, we do not consider wave-averaged models in this thesis.

A categorisation can be made into depth-averaged (and depth-integrated) models and depth-resolving models (Briganti et al., 2016). The former integrate model quantities in the vertical direction, meaning that any information pertaining to the vertical distribution must be parameterised or modelled separately. Depth-resolving models do not have this restriction, and as such enable the study of vertically dependent processes. The strength of depth-averaged models lies in their computational cost which is significantly lower than depth-resolving models when applied to the same case. On the other hand, while hydrodynamic predictions generally are good, depth-averaged models have difficulty predicting sediment transport fluxes correctly (e.g. Incelli et al., 2016; Jongedijk, 2017; Ruffini et al., 2020; Mancini et al., 2021).

Different approaches exist for depth-resolved modelling of sediment transport. The simplest approach is using depth-resolving hydrodynamics coupled with a stand-alone transport model. An example of such a study is the model of Bakhtyar et al. (2009) who used the solution of a depth-resolving Reynolds-Averaged Navier-Stokes (RANS) to force a bedload model. More complex, one can model both bedload and suspended load. One way to approach suspended load is to model it as a passive scalar, using an advection-diffusion approach with empirical formulas for sediment pickup at the bed. Jacobsen et al. (2014) used this approach in his sediMorph model. He coupled bedload and suspended load transport with a mobile bed, thus creating a fully coupled morphodynamic simulation. Even though this simulation now closes the morphodynamic loop on an intraswash timescale, the flow of water is only affected by sediment transport through the morphodynamic feedback. However, there are other interactions as well, such as sediment leading to higher effective fluid densities, higher effective fluid viscosities (Boyer et al., 2011) and dampened turbulence (Van Rijn, 2007). Still, if one incorporates these interactions, sediment is modelled as a semi-passive advection-diffusion equation where no momentum is exchanged between the sediment and the water flows.

The next step of complexity adds these interactions. These models, here called Euler-Euler models, model the flow of water and sediment as two different conserved phases, both with momentum equations with terms for interphase momentum exchange. An example is the model by Bakhtyar et al. (2010), who applied this technique to simulate small-scale swash zone dynamics under regular waves. This technique was also used by Mathieu et al. (2022) for modelling detailed sediment and turbulence interactions in the sheet flow layer. Although these models include more physics, the major downside is their relative computational inefficiency.

Apart from different approaches to modelling sediment transport, there are different techniques for modelling hydrodynamics as well. The main driver of complexity is the level of detail in the modelling of turbulence, where Direct Numerical Simulation (DNS) provides full coverage of the turbulent scales. However, DNS is impractical to use for anything but highly idealised simulations due to its computational cost. Instead, one can use a Large Eddy Simulation (LES) or Reynolds-Averaged Navier-Stokes (RANS) approach to parameterise turbulent

effects. Of the two, LES is more detailed as it is 3D and explicitly resolves turbulence except for the sub-grid scales which are parameterised. RANS is comparatively cheaper and can be used in 2D simulations. This approach models the time-averaged flow field and parametrises all turbulent scales at once. In the application of coastal engineering, LES is less prevalent and is usually applied in studies into detailed 3D flow phenomena (e.g. Zhou et al., 2017), whereas RANS is more popular and is often employed in 2DV simulations (e.g. Jacobsen et al., 2014; Torres-Freyermuth et al., 2013; Li et al., 2019).

1.4 Knowledge gap

Previous numerical experiments using depth-averaged intraswash morphodynamics models show great difficulty in the swash zone. The results of Jongedijk (2017), Ruffini et al. (2020) and Mancini et al. (2021) show that it is very difficult for an intraswash depth-averaged model to accurately predict time-series of suspended sediment concentrations. Furthermore, these studies tend to overpredict erosion and sometimes predict erosion for accretive conditions.

Depth-resolving swash model studies have mostly been limited to only modelling hydrodynamics. Only a few morphodynamic model studies exist. The aforementioned two-phase model by Bakhtyar et al. (2010) is one example. Also, the sediMorph model by Jacobsen et al. (2014) was used in a study of Li et al. (2019) who modelled the morphodynamics of subsequent solitary waves. These studies demonstrate the validity of the depth-resolving approach, but only limited new knowledge of sediment transport has been derived from them. For instance, there are to the author's knowledge no studies on the influence of vertical nonuniformities on intra-swash sediment transport.

Additionally, because of their limited application, the intricacies involved in depth-resolved modelling have not all been investigated, or even discovered. For instance, there exist different methods for modelling the air/water interface, and the ramifications of such a choice are not clear. Similarly, some studies (Brown et al., 2016) present recommendations about the choice of turbulence model. These studies are limited to a hydrodynamical validation. The effects of turbulence models on swash zone sand transport have not been studied.

Furthermore, it is known that for medium and fine sand, infiltration has little effect on the hydrodynamics (Masselink and Li, 2001). Instead, there are other important mobility effects relating to infiltration and exfiltration. For instance, subtle changes in boundary layer shape as water filtrates through the bed can influence the bed shear stress (Conley and Inman, 1994; Lohmann et al., 2006), but also pressure gradients can act on sediment grains, influencing the stability of the bed (Baldock and Holmes, 1998; Francalanci et al., 2008). Not many studies exist where the pore pressure gradients are measured in and around the swash zone, where the bed surface is sometimes exposed. Furthermore, practical models for the pore pressure often assume a permanently inundated bed. As this is not the case in the swash zone, we do not know to which extent these models are applicable here.

1.5 Goal and research questions

Based on the previously described knowledge gap, we formulate the following research goal and accompanying research questions.

The goal of this thesis is to improve understanding of depth-dependent processes in the swash zone and their impact on sediment transport and morphodynamics.

Q1 To what extent can a depth-resolving model predict intra-swash sand transport and morphodynamics and which processes are necessary to account for?

Q2 How do depth-dependent processes in the water column determine sediment transport in the swash zone?

Q3 How do pore pressure gradients behave in the swash zone, and how can they influence sediment mobility?

The first question is a methodological question that addresses the need for the implementation and accounting of additional physical processes and numerical improvements in order to achieve adequate model performance. The second question asks what we can learn from the model in terms of processes. The final question addresses the aforementioned importance of subsurface flow and pressure effects on sediment mobility.

1.6 Methodology and model

The first two questions are answered using a depth-resolving and wave-resolving model. In this case, as suspended sediment is important for the type of beaches this thesis aims to study, the one-way and bedload only approach by Bakhtyar et al. (2009) is insufficient. This leaves the passive scalar and Euler-Euler approaches. Although the Euler-Euler approach includes more fundamental physics, the passive scalar approach has seen more use previously in coastal sediment applications (e.g. Larsen et al., 2017; Fernandez-Mora et al., 2017). This approach also has the benefit of being similar to the typical approaches used in depth-averaged models. Furthermore, the relative computational efficiency of this approach enables more and longer model investigations. Therefore, we chose the sediMorph model by Jacobsen et al. (2014) as a basis for this research. This model is based on the open source OpenFOAM library. The model is applied to two different cases, which below are presented in Chapters 2 and 3.

1.6.1 Approach

First, we investigate the morphodynamics of non-interacting solitary waves on a beach in Chapter 2. Here, we use the experiments by Young et al. (2010) for validation and analysis. To do this, a minor but crucial improvement to the treatment of

the suspended sediment boundary condition is introduced. Furthermore, different ways of modelling the air/water interface are investigated. We use the validated model to analyse the spatial and temporal distribution of sediment for a solitary swash event.

Chapter 3 moves on to a more complex wave scenario. Here, we use the bichromatic wave experiments of Van der Zanden et al. (2019a) as a modelling case. First, to achieve satisfactory performance, the effect of wave-breaking induced turbulence and small air bubbles are investigated. The former has substantial impact on sediment mobility and the latter have great impact on the interaction between the swash flow and the bed. Subsequently, the predictive performance in terms of sediment concentrations, water depths and flow velocities is verified. The final model is then used to analyse the importance of vertical structures in the swash flow at different locations and different points in time.

Chapter 4 answers Q3 by performing large-scale laboratory experiments. In these experiments, pore pressure sensors are buried at different cross-shore locations and different depths. At the same cross-shore locations, measurements of water depths and flow velocities are also conducted. Using the measurements, a practical analytical model, based on the theory of Yamamoto et al. (1978) and Guest and Hay (2017) is calibrated and used to calculate the pressure gradients at the bed surface. These gradients are then used to analyse the sediment mobility at different phases in the swash.

1.6.2 Model description

This section briefly covers the most important equations used in the numerical model. It aims to condense elements of the model descriptions from Chapters 2 and 3 in one location. The model is largely based on the model by Jacobsen et al. (2014) which explains the morphodynamic part in more detail. Parts of the following model description are taken directly from these chapters. This section does not cover discretisation.

Hydrodynamics

The hydrodynamic model solves the 2DV two-phase incompressible RANS equations consisting of a momentum and a mass conservation equation:

$$\frac{\partial \rho u_i}{\partial t} + \frac{\partial \rho u_i u_j}{\partial x_j} = -\frac{\partial p^*}{\partial x_i} - g_j x_j \frac{\partial \rho}{\partial x_i} + \frac{\partial}{\partial x_j}\left(2 S_{ij} \mu + \tau_{ij}\right), \tag{1.1}$$

$$\frac{\partial u_i}{\partial x_i} = 0. \tag{1.2}$$

Here u_i are the Reynolds averaged velocity components, ρ is the density, p^* is the excess pressure over the hydrostatic potential, x_i are the cartesian components, S_{ij} is the mean strain rate tensor defined as

$$S_{ij} = \frac{1}{2}\left(\frac{\partial u_i}{\partial x_j} + \frac{\partial u_j}{\partial x_i}\right), \tag{1.3}$$

μ is the dynamic molecular viscosity and τ_{ij} is the Reynolds stress, which is defined using the dynamic eddy viscosity ν_t and using the Boussinesq hypothesis:

$$\tau_{ij} - \bar{u_i'u_j'} = 2\nu_t S_{ij} - \frac{2}{3}k\delta_{ij}, \tag{1.4}$$

where δ_{ij} is the Kronecker delta. The turbulent kinetic energy k is defined as

$$k = \frac{1}{2}\bar{u_i'u_j'}, \tag{1.5}$$

where the bar denotes ensemble averaging, and the prime signifies the fluctuating velocity component.

The turbulence closure equations for k and ω are defined as

$$\frac{\partial \rho k}{\partial t} + \frac{\partial \rho u_j k}{\partial x_j} = P_k - \rho\beta^* k\omega + \frac{\partial}{\partial x_j}\left[\left(\mu + \rho\sigma^* \frac{k}{\omega}\frac{\partial k}{\partial x_j}\right)\right], \tag{1.6}$$

$$\frac{\partial \rho \omega}{\partial t} + \frac{\partial \rho u_j \omega}{\partial x_j} = P_\omega - \rho\beta\omega^2 + \rho\frac{\sigma_d}{\omega}\frac{\partial k}{\partial x_j}\frac{\partial \omega}{\partial x_j} + \frac{\partial}{\partial x_j}\left[\left(\mu + \rho\sigma \frac{k}{\omega}\frac{\partial \omega}{\partial x_j}\right)\right]. \tag{1.7}$$

Here P_k and P_ω are the production terms for k and ω respectively and defined as

$$P_k = p_0\nu_t, \quad P_\omega = \alpha\frac{\omega}{\tilde{\tilde{\omega}}}p_0, \quad p_0 = 2S_{ij}S_{ij}, \tag{1.8}$$

and

$$\sigma_d = H\left(\frac{\partial k}{\partial x_j}\frac{\partial \omega}{\partial x_j}\right)\sigma_{do}, \tag{1.9}$$

with H being the Heaviside function.

In accordance with Larsen and Fuhrman (2018) the eddy viscosity is defined as

$$\nu_t = \frac{k}{\tilde{\omega}}, \tag{1.10}$$

where

$$\tilde{\tilde{\omega}} = \max\left(\omega, \lambda_1\sqrt{\frac{p_0}{\beta^*}}\right), \quad \tilde{\omega} = \max\left(\tilde{\tilde{\omega}}, \lambda_2\frac{\beta}{\beta^*\alpha}\frac{p_0}{p_\Omega}\omega\right), \tag{1.11}$$

with $p_\Omega = 2\Omega_{ij}\Omega_{ij}$, where Ω_{ij} is the mean rotation rate tensor. The constants are defined with their default values: $\alpha = 0.52$, $\beta = 0.00708$, $\beta^* = 0.09$, $\sigma = 0.5$, $\sigma^* = 0.6$, $\sigma_{do} = 0.125$, $\lambda_1 = 0.2$ and $\lambda_2 = 0.05$.

The VoF method is incorporated using an indicator field φ which is used to determine the density and viscosity of the air/water mixture in each cell. No surface tension effects are employed in this model.

Sediment transport

The model separately calculates bedload and suspended load. Both bedload and suspended load formulations require the Shields number θ and the critical Shields number θ_c.

$$\theta = \frac{|\tau_b|}{(\rho_s - \rho)gD_{50}}, \tag{1.12}$$

where τ_b is the bed shear stress as calculated from the turbulence model and ρ_s is the sediment density. The critical Shields number is calculated as

$$\theta_c = \theta_{c0} f_{slope}, \tag{1.13}$$

where $\theta_{c0} - 0.05$ is the critical Shields parameter for a horizontal bed and f_{slope} is a function that takes the slope into account (see Roulund et al. (2005) for details).

Bedload transport q_{b_i} is calculated on the bed faces using (Engelund and Fredsoe, 1976):

$$q_{bi} = \frac{1}{6}\pi d^3 \frac{P_{EF}}{d^2} U_{bi}, \tag{1.14}$$

where d is the grain size, here taken as the median grain size D_{50}, U_{bi} is the velocity near the bed, which is calculated using the method of Roulund et al. (2005), and P_{EF} is the percentage of particles in motion in the surface layer of the bed:

$$P_{EF} = \left[1 + \left(\frac{\frac{1}{6}\pi\mu_d}{\theta - \theta_c}\right)^4\right], \tag{1.15}$$

where $\mu_d = 0.51$ is the dynamic friction coefficient and θ_c is the c

accounting for bed slope effects as described by Roulund et al. (2005). Suspended load is calculated on a subset of the mesh used for the hydrodynamic model. In this subset, the cells nearest to the bed that are closer than the reference concentration height y_a are removed. This means that the bottom boundary condition for the suspended sediment concentration is defined at the reference height. The evolution of the concentration c is modelled using an advection-diffusion approach, here in vector notation as

$$\frac{\partial c}{\partial t} + (\alpha u_i + w_s \delta_{i2})\frac{\partial c}{\partial x_i} - \frac{\partial}{\partial x_i}\left[\alpha(\nu + \nu_t)\frac{\partial c}{\partial x_i}\right] = 0, \tag{1.16}$$

where w_s is the fall velocity which can be calculated or prescribed. The reference concentration c_a can be calculated using different reference concentration models. In this thesis, both the Engelund and Fredsoe (1976) and the Zyserman and Fredsøe (1994) concentration models are used.

Zyserman and Fredsøe (1994) provide the following relation for the concentration at the bed:

$$c_b = \frac{A(\theta - \theta_c)^{n_c}}{1 + \frac{A(\theta-\theta_c)^{n_c}}{c_m}}, \tag{1.17}$$

where $A = 0.331$, $n_c = 1.75$ and $c_m = 0.46$. The formulation of Engelund and Fredsoe (1976) gives the following relation for c_b (according to Larsen et al. (2017)):

$$c_b = \frac{c_0}{(1 + 1/\lambda_b)^3}, \tag{1.18}$$

where

$$\lambda_b^2 = \frac{\kappa^2 \alpha_1^2}{0.013 s\theta} \left(\theta - \theta_c - \frac{\pi}{6} \mu_d P_{EF} \right), \tag{1.19}$$

where $\kappa = 0.41$, $\alpha_1 = y_a/d$ and $s = \frac{\rho_s}{\rho}$.

Boundary conditions

The model typically has four boundaries. At the offshore part of the model, waves are generated using the waves2Foam module Jacobsen et al. (2012). This module uses relaxation zones to generate incoming waves and dampen outgoing waves. At the top of the domain, an atmospheric boundary condition is imposed. This condition defines the total pressure p as

$$p = \begin{cases} p_0 - u_i u_i & \text{if inflow;} \\ p_0 & \text{if outflow,} \end{cases} \tag{1.20}$$

where p_0 is a reference pressure, often put to zero. The velocity condition is defined as a zerogradient condition for outflow, and as the normal component of the cell boundary cell velocity for inflow. All other quantities use a similar boundary condition where a zerogradient condition is applied on outflow and the boundary value of the quantity is set to zero on inflow. The right wall of the domain uses a zerogradient condition in pressure and a no-slip condition for velocity. All other quantities are defined as a zero Dirichlet condition.

The bed boundary conditions are the most complicated. Here the velocity is a no-slip condition and the pressure is a zerogradient condition. The suspended sediment is defined as a special Dirichlet condition which represents the reference concentration as explained above, or in the case that the concentration in the cell above the bed is higher than the reference concentration, this concentration is prescribed on the boundary instead (this is referred to as an overload condition). For turbulent quantities, extra care is taken. These, and the friction velocity U_f, are modelled using wall functions. The friction velocity is calculated using the Cebeci and Chang (1978) approach, which accounts for bed roughness. The resulting shear at the bed is then modelled by modifying the eddy viscosity ν_t on the wall according to:

$$(\nu + \nu_t) \frac{\partial u_p}{\partial n} = \frac{\tau_b}{\rho} = U_f^2, \tag{1.21}$$

where $\frac{\partial u_p}{\partial n}$ is the wall-parallel velocity gradient in the wall-normal direction. For the turbulent quantities k and ω we use the boundary conditions by Fuhrman et al. (2010). These prescribe a zerogradient condition for k and ω as follows:

$$\omega = \frac{U_f^2}{\nu} S_R, \tag{1.22}$$

where

$$S_R = \begin{cases} \left(\frac{200}{k_N^+}\right)^2 & , k_N^+ \leq 5 \\ \frac{K_r}{k_N^+} + \left[\left(\frac{200}{k_N^+}\right)^2 - \frac{K_r}{k_N^+}\right] e^{5-k_N^+} & , k_N^+ > 5, \end{cases} \tag{1.23}$$

with

$$k_N^+ = k_N U_f / \nu \tag{1.24}$$

where k_N is the Nikuradse roughness and $K_r = 100$ is an empirical coefficient.

Bed update

The bed update has three components, the bedload contribution, the suspended load contribution and a sandsliding mechanism. The former two can be captured in the following continuity equation:

$$\frac{\partial h}{\partial t} = -\frac{1}{1-e_d}\left(\frac{\partial q_{bi}}{\partial x_i} + E + D\right), \tag{1.25}$$

where h is the bed level, e_d is the bed porosity and E and D are the erosion and deposition fluxes, calculated as

$$E = (\nu + \nu_t)\frac{\partial c}{\partial x_2} \tag{1.26}$$

and

$$D = c_b(w_s - u_2), \tag{1.27}$$

where $\boldsymbol{N}$ is the normal vector of the bed, pointing out of the model domain (i.e. pointing into the ground). The calculation of these fluxes as they occur in the cells of the discretised domain are described in more detail in Jacobsen et al. (2014) and Jacobsen (2015). The sandsliding mechanism is activated when the bed slope exceeds the critical bedslope β_c. Here the scheme of Niemann (2004) is used. This method works in three steps. First the upper most boundary point where the slope exceeds the critical slope is identified. This point is then lowered until the slope in that cell no longer exceeds the critical slope. The change in bed volume in the cell is calculated and the next point down from the previous point is raised such that this fulfills the mass balance. This procedure is then repeated until all bed faces have an slope that is shallower than the critical slope.

1.6.3 Software

Foam-extend is one of the variants of the open source OpenFOAM®toolbox, the trademark which is registered by OpenCFD®. It uses the Finite Volume Method on an unstructured mesh. Although OpenFOAM is often thought of as a numerical simulation tool for fluid dynamics, fundamentally it is a library for generally manipulating and applying differential operations on fields. For details in

implementation of the numerics and validation thereof, the reader is referred to Jasak (1996) and Qwist and Christensen (2023).

In this thesis, the foam-extend 4.0 version is used. Regardless of the version used, native OpenFOAM does not include sediment transport or bed-updating. Both were instead incorporated through the sediMorph model by Jacobsen et al. (2014). OpenFOAM sees wider use in coastal applications apart from morphodynamics. For instance, the theses of Van Bergeijk (2022) and Chen et al. (2020) used OpenFOAM-based models to investigate effects of transitions and roughness on dike stability. OpenFOAM has also been used to study airflow patterns around buildings on the beach (Pourteimouri et al., 2022). Apart from these engineering scale models, OpenFOAM is also at the basis of more fundamental models such as the aforementioned sedFoam (Cheng et al., 2017; Chauchat et al., 2017).

1.6.4 Outline

Following the introduction are three scientific chapters (see Figure 1.4) . Chapter 2 investigates morphodynamics of solitary waves using depth-resolved modelling. Chapter 3 uses the same model to investigate bubbles, turbulence and vertical structures for bichromatic waves. Finally, Chapter 4 investigates pore-pressures in the bed using large-scale laboratory experiments. In Chapter 5, the research approach and results are discussed. Subsequently, the research questions are answered in Chapter 6 alongside recommendations for future research and applications of the thesis results.

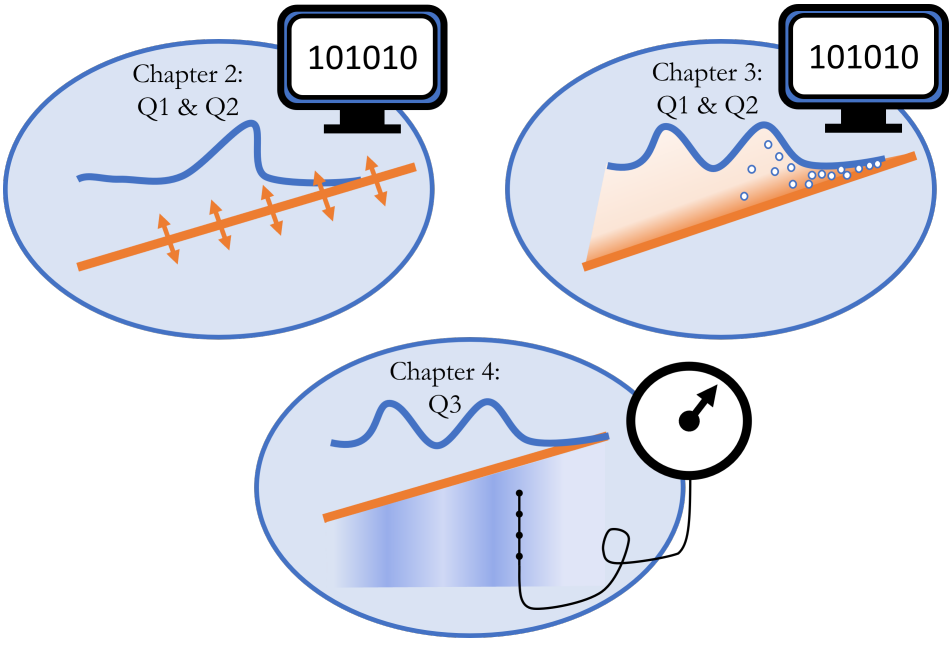

Figure 1.4
Graphical outline of the three scientific chapters in this thesis.

Chapter 2

Depth-Resolved Modelling of Intra-Swash Morphodynamics Induced by Solitary Waves

This chapter has been published as Kranenborg, J. W. M. , Campmans, G. H. P., Jacobsen, N. G., Van der Werf, J. J., Reniers, A. J. H. M., & Hulscher, S. J. M. H. (2022). Depth-Resolved Modelling of Intra-Swash Morphodynamics Induced by Solitary Waves. Journal of Marine Science and Engineering, 10(9), 1175

Abstract

We present a fully-coupled 2DV morphodynamic model, implemented in OpenFOAM that is capable of simulating swash-zone morphodynamics of sandy beaches. The hydrodynamics are described by the Reynolds-averaged Navier-Stokes (RANS) equations with a $k-\omega$ turbulence model and the Volume of Fluid (VoF) approach for discriminating between air and water. Sediment transport is described in terms of bedload and suspended load transport. We show that the default divergence scheme in OpenFOAM can become numerically unstable and lead to negative sediment concentrations, and propose a solution to avoid this problem. The model performance is assessed in terms of surface elevation, flow velocities, runup, suspended sediment concentrations, bed profile evolution and sediment transport volumes by comparing with measurements of field-scale (wave height of 0.6 m) solitary waves. The model shows reasonable agreement in terms of hydrodynamics and predicts the correct sediment transport volumes, although the deposition is predicted more onshore compared to the measurements. This is partially attributed to an overprediction of the runup. The model shows that the suspended sediment concentration displays a strong vertical dependence. These results show the potential of depth-resolving models in providing more insight into morphodynamic processes in the swash zone, particularly with respect to vertical structures in the flow and suspended sediment transport.

2.1 Introduction

The swash zone is the boundary between the surf zone and the dry part of the beach which is intermittently covered and exposed by waves. It is characterised by large amounts of sediment transport and rapid morphological change, that can be on the order of several centimetres in seconds (Blenkinsopp et al., 2011; Van der Zanden et al., 2015). Furthermore, through this region sediment is exchanged between the surf zone and the dry part of the beach (Masselink et al., 2005). Consequently, the swash zone is an important part for determining the overall beach morphology. However, though the swash zone is easily accessible for measurements, many processes governing sediment transport and morphology are not yet well understood. Examples of such processes are the vertical concentration profiles of suspended sediment and the influence of turbulence on sediment pick-up (Puleo and Torres-Freyermuth, 2016).

Numerical models can be used to give better insight into such processes. Typically, these wave resolving models implement depth averaged equations, coupled with a sediment transport equation and the sediment balance equation for the bed level change. Examples of the use of those models are the study of intra-swash solitary wave transport and morphodynamics (Zhu and Dodd, 2015), groundwater and morphodynamics of gravel beaches (McCall et al., 2015), the morphodynamics of sandy beaches (Incelli et al., 2016), the morphodynamics of a dambreak-induced swash on a coarse bed (Briganti et al., 2018) and morphodynamics and sediment transport by bichromatic waves on a sandy beach (Ruffini et al., 2020; Mancini et al., 2021). In these studies, the hydrodynamic model predictions are more accurate than the predictions of sediment transport and morphodynamics. This is often attributed to the lack of certain processes in the model formulation, such as turbulence and vertical sediment concentration profiles (Reniers et al., 2013; Mancini et al., 2021). Such processes are difficult to study experimentally because of the small scales, shallow flows and the presence of air bubbles and high sediment concentrations near the bed. Furthermore, measurements are mostly confined to a limited number of cross-shore locations (Van der Zanden et al., 2015).

Depth-resolving numerical models can provide valuable insights in such processes (Puleo and Torres-Freyermuth, 2016). Previous research using these models has mostly been reserved to studying aspects of hydrodynamics only. Most of these studies are based on the Reynolds-Averaged Navier-Stokes (RANS) approach, coupled with a Volume of Fluid (VoF) method to discriminate between air and water. Examples of such model studies include the study of boundary layer profiles and shear stresses (Torres-Freyermuth et al., 2013; Higuera et al., 2018), velocity profiles around bore collapse (Mory et al., 2011), infiltration and subaqueous flow (Pintado-Patiño et al., 2015) and turbulence production and dissipation (Desombre et al., 2013). More detailed studies of turbulent structures have been performed with Large Eddy Simulations (LES) (e.g. Zhou et al., 2017; Kim et al., 2017). Some studies use an uncoupled approach, where the hydrodynamic output produced by the model is used as input for a sediment transport formula. Bakhtyar et al. (2009, 2011) used the modelled bed shear stresses as input for the Meyer-Peter-Müller

sediment transport formula. The calculated transport was subsequently used to calculate a bed level change.

Depth-resolved morphodynamic models have been used for various applications in the coastal region. Examples include studying bar migration (Jacobsen et al., 2014; Jacobsen and Fredsoe, 2014b), the influence of sand nourishments on bar migration (Jacobsen and Fredsoe, 2014a), scour around monopiles (Larsen et al., 2017) and beneath pipelines (Li et al., 2020), and surf-zone sediment transport and morphodynamics (Fernandez-Mora et al., 2017). However, only a few studies applied such models to the study of swash-zone processes. Bakhtyar et al. (2010) use a two-phase approach that solves momentum equations for both the fluid and sediment phases which are coupled to account for the influence of sediment on the fluid flow and vice-versa. They studied sediment transport and morphodynamics induced by regular waves. Conversely, Li et al. (2019) use a model based on the model by Jacobsen et al. (2014), which separates the sediment transport in bedload and suspended load transport. They simulated the solitary wave experiments by Sumer et al. (2011) and investigated bed shear stresses, turbulence levels and morphodynamics. The model correctly predicted the erosive response, although a comparison could only be made at the discrete points where the bed level change was measured. Recently, García-Maribona et al. (2021) extended the existing IH2VOF model (Lara et al., 2011) by including sediment transport and morphology, and studied this model performance for both a solitary wave and regular waves.

These studies show the potential of using depth-resolving models to predict morphodynamics and analyse sediment-related processes in the swash zone. However, due to the limited number of model studies, the performance of such depth-resolving models is not yet well quantified and understood. Furthermore, numerical instabilities can lead to unwanted behaviour when modelling suspended sediment. In wave boundary layers, the ratio of eddy viscosity to the settling velocity can lead to numerical instabilities at the bed boundary (Jacobsen, 2011). This can lead to unphysical behaviour of suspended sediment concentrations near the boundary, such as negative sediment concentrations.

In this paper, we present an analysis of the sediment transport and morphodynamics of a fully-coupled morphodynamic model, based on the model by Jacobsen et al. (2014). As part of the model development, we pose a generally applicable solution to the numerical instability described above, which leads to physically consistent sediment concentrations near the bed. Furthermore, we analyse the model performance in terms of intra-swash sediment dynamics and morphodynamics. To do this, we use the solitary wave experiments by Young et al. (2010). These were chosen, as they include full bed profile measurements, sediment concentrations measurements and were conducted using field-scale swash waves ($H = 0.6\,\mathrm{m}$).

In the following section the model and the experiment are described. Section 3 presents the solution to the numerical instability. Section 4 presents the model results and a comparison with measurements. Subsequently, Section 5 provides an analysis of the intra-swash sediment transport and morphodynamics. Lastly, the results are discussed in Section 2.6 and the main findings are presented in Section 2.7.

2.2 Methodology

2.2.1 Model description

The morphodynamic model is a 2DV RANS model that is extended to include sediment dynamics and morphodynamics. The model is implemented using the open-source OpenFOAM® toolbox, specifically the foam-extend-4.0 version, which uses the finite volume method for solving flow-related problems. In this section the different aspects of the model are explained.

Numerical model

The hydrodynamic model implements the 2DV RANS equations for multiphase flow, using the VoF method for discriminating between air and water. The model uses the Wilcox (2008) $k-\omega$ turbulence model (k is the turbulent kinetic energy and ω is the specific rate of dissipation) to which the limiter proposed by Larsen and Fuhrman (2018) is added (see appendix 2.A for the hydrodynamic model equations). This limiter poses a solution to the instability in the standard turbulence model formulations for wave dominated flows, which leads to unphysical growth of turbulent kinetic energy in regions of (near) potential flow. Furthermore, the solitary waves are generated using the waves2Foam (Jacobsen et al., 2012) module. The sediment transport and morphology is calculated using the model by Jacobsen et al. (2014). We will briefly explain how this model works; for details we refer to the original paper by Jacobsen et al. (2014).

Sediment transport is modelled as bedload and suspended load separately. The bedload transport model implements the (Engelund and Fredsoe, 1976) bedload formula accounting for bed slope effects as implemented by Roulund et al. (2005). Suspended load transport is modelled with an advection diffusion approach, where a reference concentration is set at a reference height z_a above the bed. In this work we use both the Engelund and Fredsoe (1976) and Zyserman and Fredsøe (1994) formulas. For both we define the reference height at $z_a = 2.5D_{50}$, with D_{50} being the median grain size. The sediment is advected by the fluid flow to which a settling velocity is added. This settling velocity is calculated by the method of Fredsøe and Deigaard (1992, pages 198-199). The fluxes from both the bedload and suspended load are used to calculate the bed level change. This bed level change is then applied using a moving mesh, which moves the mesh points such that the boundary displacement corresponds to the calculated morphological change. This is done using the mass conserving interpolation method by Jacobsen (2015).

Two different VoF-methods are investigated, namely the MULES method (for details on the implementation see Deshpande et al., 2012) and the isoAdvector method (Roenby et al., 2016). MULES is the default VoF method in OpenFOAM. isoAdvector was designed to address a common issue with many VoF-schemes, including MULES, where the interface between the water and air phases in the solution is diffuse. Moreover, many methods, including MULES, are sensitive to mesh quality. For this reason we also ran simulations with isoAdvector instead of

MULES. However, this model led to instabilities in the bedload calculation, which led to local bed instabilities. These instabilities quickly resulted in crashes. To circumvent this issue, the bed level change induced by the bedload was smoothed using the local filtering operation, suitable for non-equidistant meshes, proposed by Jacobsen (2015):

$$V_i^* = \frac{1}{4}\left(V_{i-1} + 2V_i + V_{i+1}\right), \tag{2.1}$$

where V_i denotes the volume of bed level change, the star $*$ denotes the filtered volume and the subscript differentiates between neighbouring cells. This filtering procedure was iterated 16 times to achieve a smoother solution. This was decided after trying 1, 4 and 16 iterations respectively, where only the latter choice led to sufficiently stable simulations.

Initial and boundary conditions

The bed boundary, the paddle and the onshore flume walls are modelled using a no-slip boundary condition. At the top of the domain the pressure is kept to ambient atmospheric pressure from which the velocity then is derived, allowing air to flow in and out of the domain. At the bed boundary the turbulent quantities are set such that roughness effects are incorporated. For k and ω we follow the boundary condition of Fuhrman et al. (2010). This boundary condition includes the roughness into the turbulence boundary conditions. Furthermore the rough wall model by Cebeci and Chang (1978) as implemented by Larsen et al. (2017) is used to model the friction velocity in the bed-boundary cells. The roughness height is taken to be $k_N = 2.5D_{50}$ following the studies of Larsen et al. (2017) and Li et al. (2019).

The model will presently be used to study morphodynamics of solitary waves. The solitary waves were generated using the waves2Foam module (Jacobsen et al., 2012), by using the analytical formula by Chappelear (1962) to determine the initial surface elevation, pressure and velocity fields corresponding to a solitary wave with its crest at $x = 6$m. Because of this, the start time of the simulation does not correspond to the start time of the experiments. The time difference was determined to be 3.37 seconds by measuring the time when the wave crest passed the wave gauge at $x = 10$m. The simulations were run for 50 s.

Geometry and mesh

The model geometry is 54 m long in the cross-shore direction and two meters tall in the vertical-direction. The mesh, consisting of 830,400 cells in total, is generated in three layers, a 1 cm thick bottom boundary layer, a 39 cm transition layer and a top layer containing the top 1.6 m of the domain. The bottom layer contains 20 cells that are 0.5 mm thick in the vertical direction. This layer follows the bed morphology. The top layer contains 80 larger cells that are 0.02 m thick. This layer follows the straight top boundary of the domain. In between lies the transition layer that uses 73 cells to facilitate a smooth change between the two layers. The mesh

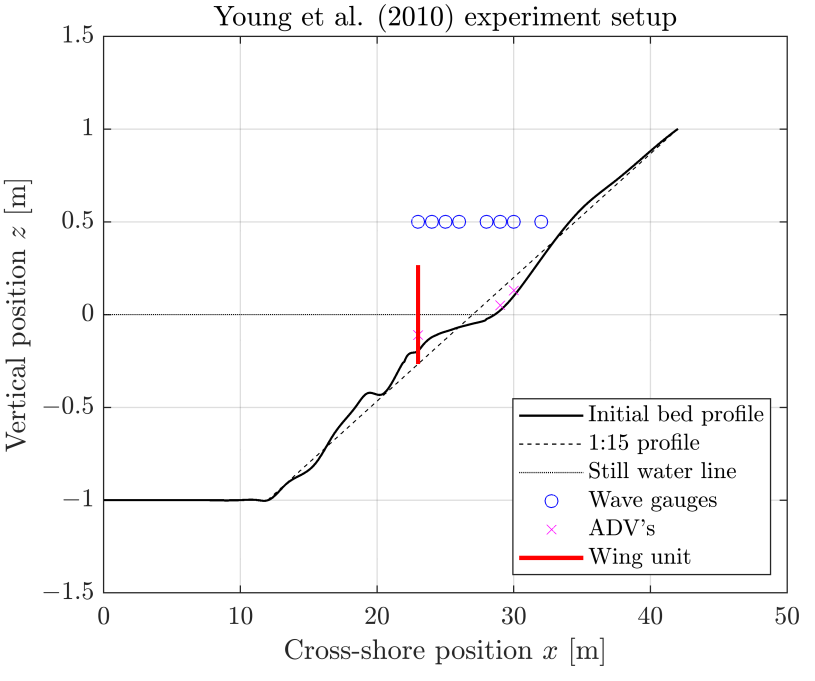

Figure 2.1
Schematic overview of the experiment setup of Young et al. (2010), including instrument locations.

uses two different cell widths for the straight and sloped sections of the domain. The sloped section uses 1cm wide cells while the straight section uses 2 cm wide cells. This mesh gives a high resolution mesh near the bed boundary to resolve boundary processes while also mostly keeping the mesh aspect ratio (here defined as Δ_x/Δ_y) at or below a maximum of 2. An aspect ratio near 1 is important for simulating wave breaking correctly (Jacobsen et al., 2012). Between successive runs the final bottom mesh from the previous simulation is used as the initial mesh for the next simulation.

2.2.2 Comparison with measurements

The analyses in this paper use the solitary wave experiments from Young et al. (2010) as a basis. An overview of the experimental setup is shown in Figure 2.1. In the experiment, nine independent consecutive solitary waves with a wave height of $H = 0.6\,\mathrm{m}$ were generated by a paddle and sent onto a beach consisting of fine sand ($D_{50} = 0.2\,\mathrm{mm}$). After a 12 m long straight immobile section, there is a sandy bed with a slope of roughly 1:15. The initial beach profile is not straight, because the experiment setup was used for different waves prior to the ones published in the study of Young et al. (2010). The water depth is 1m which gives a initial shoreline position of roughly $x = 27.5\,\mathrm{m}$.

The model results are compared with the physical measurements of wave gauges, ADV's (Acoustic Doppler Velocimeter) for measuring cross-shore velocities, OBS's (Optical Backscatter Sensor) to measure sediment concentrations and a profiler to measure the bed profile position. The location of these probes can be seen in Figure 2.1. Furthermore, a wing unit was placed in the flume at $x = 23\,\mathrm{m}$. On these units, four OBS's and four ADV's were mounted at four equidistant positions, from 9 cm to 39 cm above the bed. The other ADV's were mounted 3 cm from the bed. Finally, the profiler measured the bed profile after 3, 6 and 9 runs respectively. The measured change after 3 waves is used to compare the spatial distribution of the bed level change. Furthermore, the volume of sediment transported and the runup, here defined as the maximum shoreward location with a minimum depth of 1cm, are compared.

Time series of the surface elevation, velocity and sediment concentration are assessed using a Normalised Root-Mean-Square-Error (nRMSE) approach, where the RMSE is normalised by the maximum measured surface elevation or velocity (absolute value). For this, the surface elevation η is defined as the increase of the water level above the initial surface elevation or above the dry bed. The assessment of the bathymetric evolution is done in two ways, namely by using the Root Mean Squared Transport (RMST) metric introduced by Bosboom et al. (2020), and by calculating the integral erosion and deposition volumes I_{ero}, I_{dep} respectively. The RMST is calculated on a domain from $x = 13\,\mathrm{m}$ to $x = 39\,\mathrm{m}$ which corresponds to the domain on which the bed level was measured by Young et al. (2010). For the calculation the sea boundary is assumed closed and the beach boundary is assumed to be open for sediment to pass through. The erosion and deposition integrals are calculated using

$$\begin{aligned} I_{\mathrm{ero}} &= -\int_0^L \min(0, \Delta z_b)\mathrm{d}x, \\ I_{\mathrm{dep}} &= \int_0^L \max(0, \Delta z_b)\mathrm{d}x, \end{aligned} \tag{2.2}$$

where Δz_b is the bed level change relative to the initial morphology (positive Δz_b means deposition) before the first wave as a function of cross-shore location x. The integrals are calculated numerically using the trapezoidal method.

2.3 New boundary divergence scheme

When modelling suspended sediment using an advection equation and a reference concentration one can run into a common numerical instability. This instability stems from the ratio of advective and diffusive transport at the boundary. This is described by the boundary cell-Peclet number Pe:

$$Pe = u_c \Delta / K_c, \tag{2.3}$$

where u_c, Δ and K_c are the local cell velocity normal to the boundary face, cell width normal to the boundary face and diffusion coefficient. When $Pe > 2$ the

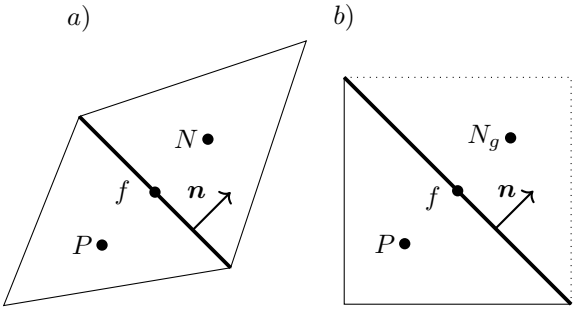

Figure 2.2
Schematic figure of a) two cells P (parent) and N (neighbour) and b) a boundary cell P with its ghost cell N_g. f is the face between two cells and $\boldsymbol{n}$ defines the normal vector .

regular 2nd order central difference discretisation of the advection-diffusion equation results in wiggly solutions (Boudet, 2011). To mitigate this, a different discretisation of the advection operator needs to be employed. For such applications, TVD (Total Variation Diminishing) schemes provide a good solution as they can remove the wiggles without sacrificing numerical accuracy. In OpenFOAM this is implemented for internal faces, however for boundary faces the issue persists. For suspended sediment applications, this can lead to regions of negative sediment concentration near the bed. In this section we describe this problem and show a solution, that effectively applies the method used for internal cells to boundary cells.

2.3.1 Discretisation of divergence operator

The finite volume method uses Gauss's theorem applied to control volumes (cells) to transform a divergence operator into a sum of fluxes over the volume boundaries. Here the quantity γ is advected by the flow $\boldsymbol{u}$:

$$\boldsymbol{\nabla} \cdot (\boldsymbol{u}\gamma)_{cell} = \frac{1}{V} \int_V \boldsymbol{\nabla} \cdot (\boldsymbol{u}\gamma) dV = \frac{1}{V} \oint_S \gamma(\boldsymbol{u} \cdot \boldsymbol{n}) dS, \tag{2.4}$$

where V and S are the cell volume and faces respectively. This last integral is approximated as the sum of fluxes accross the volume interfaces:

$$\sum_f \gamma_f \boldsymbol{u}_f \cdot \boldsymbol{n}_f S_f = \sum_f F_f \tag{2.5}$$

where the subscript f refers to the quantities associated with that face.

The only unknown in this equation is γ_f. This quantity needs to be defined. This can be done by interpolating between the two cell values γ_N and γ_P (see Figure 2.2). The interpolation is based on two things: the linear interpolation of the cell values and the contribution of upwinding.

The interpolation for faces between two cells is calculated as

$$\gamma_f = \gamma_N + w(\gamma_P - \gamma_N), \tag{2.6}$$

where w is the interpolation weight. When $w = 0$, the flux is fully described as first order upwind. Conversely when $w = 1$, the flux is fully first-order downwind. These interpolation weights are defined as

$$w = w_l\psi + (1 - \psi)_{upwind}, \tag{2.7}$$

where w_l are the linear interpolation weights (these result in a second-order central difference expression) and ψ the scheme weights. Also the $(1 + \psi)_{upwind}$ term only contributes in the upwind direction. These ψ weights can be calculated using various schemes (see e.g. Darwish and Moukalled (2003) for details on how to do this for unstructured meshes).

2.3.2 Treatment of boundary faces

There are multiple ways to define the flux F_f across the boundary faces. Per default OpenFOAM defines the flux as

$$F_f = \gamma_{BC}\boldsymbol{u}_f \cdot \boldsymbol{n}S_f, \tag{2.8}$$

where γ_{BC} is the prescribed value of γ on the boundary. However, this formulation does not take into account which scheme is used for the flux calculations on the rest of the domain (as defined in Eq. (2.6)), and hence upwinding is not taken into consideration. This can lead to unwanted effects when the flow $\boldsymbol{u}_f$ points out of the domain.

An alternative formulation would use a similar approach as Eq. (2.6). Here we will use a ghost-cell, where an artificial cell is added, to define fluxes across the boundary face (see Figure 2.2).

We define γ_{N_g} using the fact that we want $\gamma|_f = \gamma_{BC}$. Here we can use linear extrapolation to define

$$\gamma_{N_g} = \gamma_P + 2(\gamma_{BC} - \gamma_P) = 2\gamma_{BC} - \gamma_P. \tag{2.9}$$

Now we can use this result in Eq. (2.6) to obtain a value γ_f to use for the boundary flux:

$$\begin{aligned} \gamma_f &= \gamma_{N_g} + w(\gamma_P - \gamma_{N_g}) \\ &= 2\gamma_{BC} - \gamma_P + 2w(\gamma_P - \gamma_{BC}) \end{aligned} \tag{2.10}$$

The weighting coefficient w is easily calculated using Eq. (2.7) and the fact that the flux is defined exactly on the midpoint between the two cell centers:

$$w = \frac{1}{2}\psi + (1 - \psi)_{upwind}. \tag{2.11}$$

Equations (2.10) and (2.11) together define the new implementation of the Gauss convection scheme for suspended sediment.

2.3.3 1D example

Here we consider a 1D steady advection-diffusion problem with Dirichlet boundary conditions:

$$\begin{aligned} u\frac{\mathrm{d}\gamma}{\mathrm{d}x} + \frac{\mathrm{d}}{\mathrm{d}x}\left(K\frac{\mathrm{d}\gamma}{\mathrm{d}x}\right) = 0, \\ \gamma(x=0) = 0, \gamma(x=L) = 1, \end{aligned} \tag{2.12}$$

where γ is the transported scalar, L is the length of the domain, u is the advective velocity and K the diffusivity which are both constant in space and time. The analytical solution to this equation is

$$\gamma_a(x) = \frac{e^{Pe_L x/L} - 1}{e^{Pe_L} - 1}, \tag{2.13}$$

where $Pe_L = uL/K$. We solve the problem on an equidistant uniform mesh of length $L = 1\,\mathrm{m}$ and with constants $u = 0.1\,\mathrm{m/s}$ and $K = 2 \cdot 10^{-4}\,\mathrm{m^2/s}$. The numerical solution γ_n is compared with the analytical solution in three norms at the numerical grid points $\mathbf{x}$:

$$\|e\|_p = \|\gamma_a(\mathbf{x}) - \gamma_n(\mathbf{x})\|_p, \tag{2.14}$$

where $p = 1, 2, \infty$ denotes the type of norm. The problem is solved on different 1D-meshes with varying amounts of cells. This means that the simulations had different cell-Peclet numbers.

As can be seen in Figure 2.3 the new boundary condition retains the 2nd order properties when the mesh is refined (i.e. for lower Peclet numbers). Moreover, at coarser discretisations, the new scheme also correctly applies a limiter for higher Peclet numbers, which activates between $Pe = 0.5$ and $Pe = 1.667$. Because of this, the results from the new scheme do not exhibit the wiggles that are present in the results from the old scheme. This loss of wiggles translates into lower errors. Therefore, when one has limits on the boundary-cell size, the new scheme provides a way to mitigate wiggles and keep the error (locally) bounded.

2.3.4 2D Validation

To add further confidence to the applicability of the new scheme, we will investigate its behaviour when applied for a 2D steady flow situation, to which Hjelmfelt and Lenau (1970) derived an analytical solution. Their solution describes the spatial development of the suspended sediment concentration field $c[-]$ in a channel with uniform flow u and a parabolic eddy viscosity $K(y)$ in the vertical direction. Furthermore, at a reference height A above the bed, a reference concentration c_0 is applied, and the inflow is assumed to be free of sediment. By varying the reference height A, the eddy viscosity at the bottom boundary changes, thus influencing the Peclet number at the boundary. As such, the behaviour of the divergence schemes can be investigated by varying the reference height.

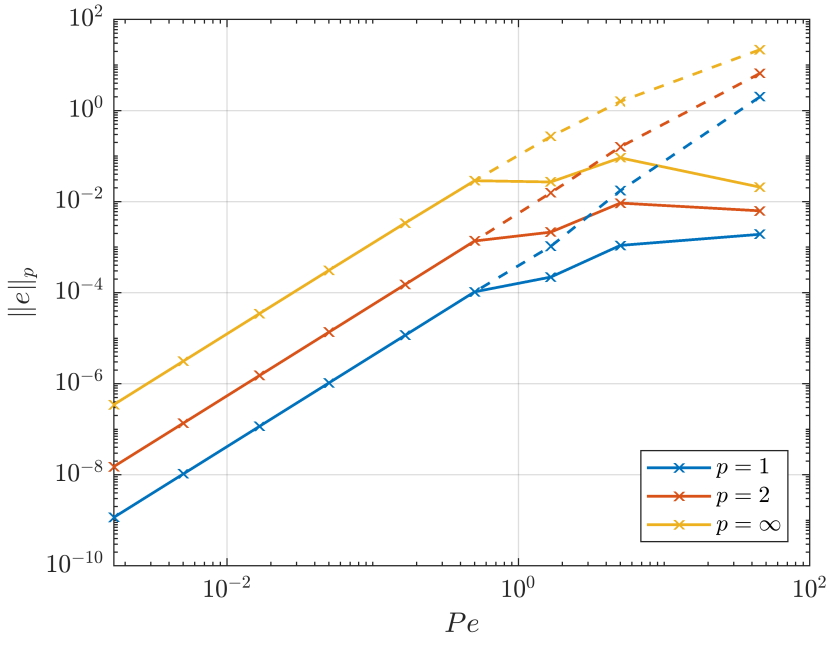

Figure 2.3
Figure showing the dependence error on the Peclet number, as measured in three different norms. The dashed lines show the performance of the old scheme and the full lines show the performance of the new scheme.

We use a case domain with length $L = 66\,\mathrm{m}$ and depth $D = 1\,\mathrm{m}$. The eddy viscosity is $K(y) = \kappa u_f y(1 - y/D)$, where $u_f = 0.055\,\mathrm{m/s}$, $\kappa = 0.4$, and the settling velocity is $w_s = 0.011\,\mathrm{m/s}$. The reference height is set at $A = 0.05\,\mathrm{m}$ and $A = 0.001\,\mathrm{m}$ which approximately corresponds to $Pe = 0.1$ and $Pe = 5$. The numerical calculations use 100 cells in the depth vertical and 400 cells in the horizontal direction. The results are shown in Figure 2.4. Panels (c) and (e) shows that the new and old schemes both work well in situations with low Peclet numbers. However, if we increase the Peclet number as in panel (d) and (f), the old scheme produces negative sediment concentrations. The new scheme correctly produces positive sediment concentrations in the whole domain although the sediment concentration is slightly underpredicted. These improvements are also reflected in the RMSE values. In the low Peclet number situation, the RMSE values for both schemes are very low and of a comparable magnitude. However, the RMSE for the new scheme in the high Peclet number situation is more than ten times lower. These values can be improved by (locally) refining the mesh. However, this defeats the purpose of this analysis, which is to show that the new scheme provides a consistently stable solution, even for a relatively coarse mesh.

2.3.5 Application to the morphodynamic model

To show the impact of the new scheme on morphodynamic simulations, two swash simulations using the different Gauss schemes were conducted for the Young et al. (2010) solitary wave case. The resulting near-bed sediment concentration profiles can be seen in Figure 2.5. It is important to note that the bottom cell is removed in the calculation of the suspended sediment transport as explained in Section 2.2.1. Instead, the bottom cell takes the concentration prescribed by the reference concentration model. The model using the old scheme produces leads to large negative sediment concentrations. This also results in spurious morphological development, since the negative concentrations effectively lead to deposition in the bed. The new Gauss scheme does not produce this region of negative concentration and instead leads to a well-behaved solution. To summarize, the new scheme mitigates nonphysical negative sediment concentrations and leads to the expected behaviour in the near-bed sediment concentration.

2.4 Model performance

Here the results of the morphodynamic model are presented. Per default the model uses the MULES VoF scheme and the Engelund and Fredsoe (1976) reference concentration model. However, the effect of isoAdvector on the hydrodynamics and morphodynamics is investigated. Furthermore the use of the Zyserman and Fredsøe (1994) reference concentration model and its effect on sediment concentrations and morphology is investigated.

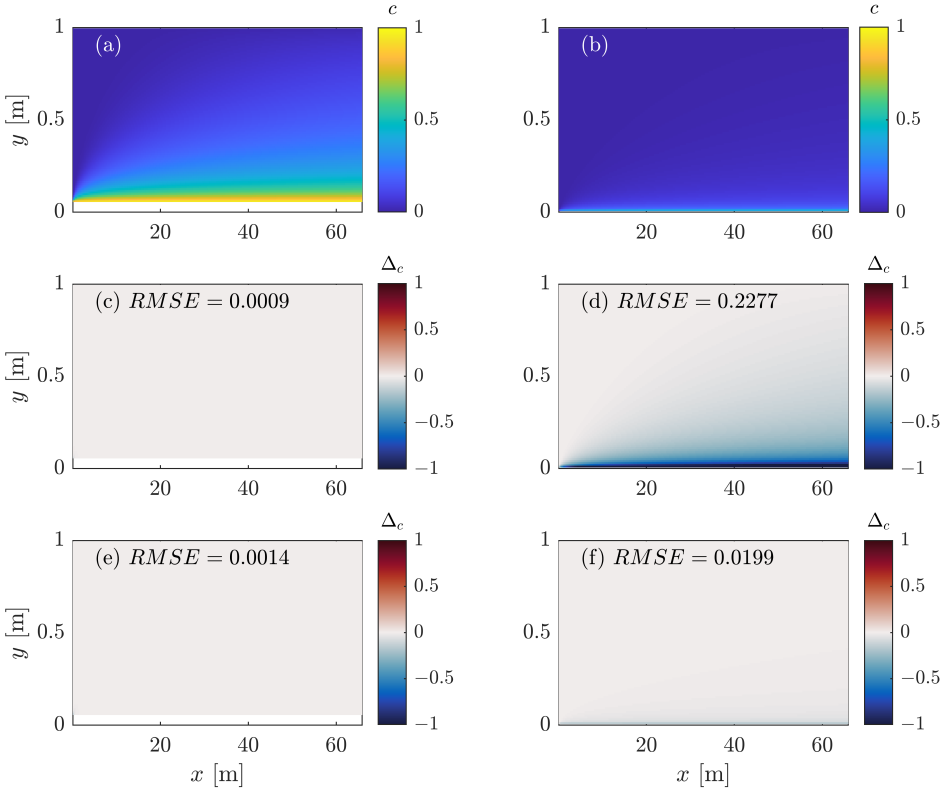

Figure 2.4
Comparison of the numerical and analytical solutions of channel flow as described by Hjelmfelt and Lenau (1970). Panels (a) and (b) show the analytical solution for $Pe = 0.1$ and $Pe = 5$ respectively. Panels (c) to (f) show the difference Δ_c between the analytical solution c and the numerical solution c_{num}. Panels (c) and (d) show the old scheme for both Peclet numbers, and panels (e) and (f) show the new scheme for both Peclet numbers.

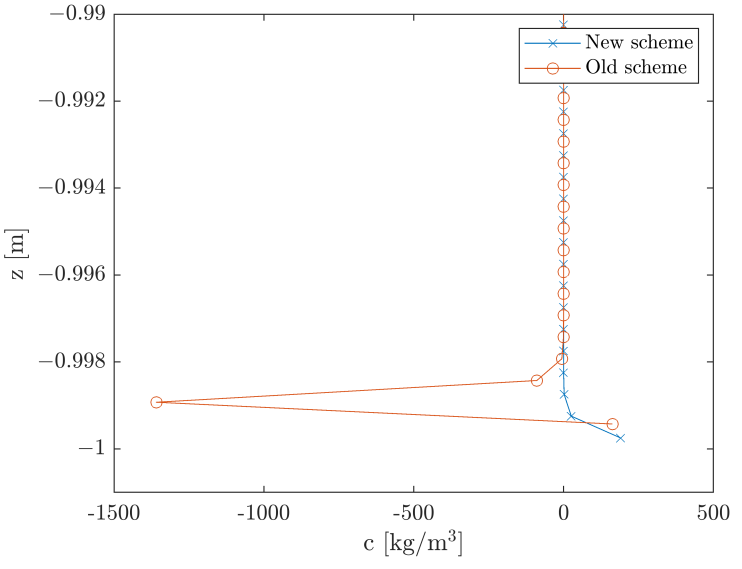

Figure 2.5
Comparison of the suspended concentration profiles near the bed produced by simulations using the old and new Gauss schemes.

2.4.1 Hydrodynamics

Figure 2.6 shows how the models compare to the measurements in terms of surface elevation. Here, two models using the different VoF methods, MULES and isoAdvector, are compared.

The incident wave is well captured by the models. After the wave breaks at around $x = 22\,\text{m}$, at about $x = 25\,\text{m}$ a bore is formed. This bore rushes up the beach, gradually slowing down. The maximum runup (not shown in the figure) is reached at around $x = 49\,\text{m}$ for the MULES model and $x = 47\,\text{m}$ for the isoAdvector model, corresponding to an overprediction of roughly 10 m and 8 m respectively. After the wave has slowed down the rundown phase begins. Most of the water runs back seaward, however a thin, slow moving layer of water was observed to remain near the bed. This is a common trait of two-phase RANS models (see e.g. Torres-Freyermuth et al., 2013; Li et al., 2019) . Figure 2.6 also shows that the rundown takes slightly longer in the model compared with the experiments. The backwash of the first swash event turns into a small wave travelling towards the paddle location. This wave then reflects at the paddle location, travels back to the beach and generates a second smaller swash event. Here the models predict a stronger and earlier reflected wave compared with the measurements (see for instance panels d-g in Figure 2.6), which also was seen in the model study by Mancini et al. (2021). This could be attributed to the paddle not being fully stationary or letting through some water at the wave reflection. It should be

Table 2.1
nRMSE figures for modelled surface elevations and velocities at different probe locations, both for the full 50 second time series and a shorter 25 second time series.

	Surface elevation							Velocity		
x [m]	24	25	26	28	29	30	32	23	29	30
MULES	0.168	0.185	0.165	0.174	0.203	0.191	0.207	0.168	0.247	0.215
MULES-25	0.152	0.124	0.106	0.102	0.126	0.114	0.222	0.151	0.280	0.264
isoAdvector	0.150	0.189	0.169	0.198	0.251	0.216	0.231	0.190	0.252	0.238
isoAdvector-25	0.116	0.106	0.099	0.089	0.122	0.124	0.237	0.178	0.300	0.292

Table 2.2
nRMSE figures for modelled sediment concentrations for two OBS probes. The values correspond to the full 50 second time series. Here E-F and Z-F refer to the transport formulations of Engelund and Fredsoe (1976) and Zyserman and Fredsøe (1994) respectively.

	$z = 0.09$ [m]	$z = 0.19$ [m]
E-F	0.104	0.458
Z-F	0.144	0.464

noted that the measured surface elevation also showed larger deviations between successive runs after the rundown phase (see for instance Figure 8 in Young et al., 2010). This is also reflected in the nRMSE values in Table 2.1, which shows better agreement during the first 25 seconds for most probes.

The comparison of the velocities can be seen in Figure 2.7. Here the cross-shore component of the velocity for the water phase is shown. The general velocity behaviour is modelled well. The breaking wave instantaneously increases the velocity. This peak velocity is higher at the two onshore locations than at the wing location. At the onshore locations, the modelled velocities are higher than the measurements. This is consistent with the observed overpredicted location of the maximum runup. However, this overprediction of velocity is not present at the wing location, suggesting that the deviation that leads to differences between the models and measurements sets in between these locations. Backwash velocities were also larger at the two onshore locations, which is explained by a backwash bore in the vicinity of the wing unit slowing down the flow. As the backwash progresses the water surface elevation drops below the vertical ADV position, which explains why the offshore locations show no data during this time (see panels b and c). From $t = 20\,\mathrm{s}$, the probe at $x = 23\,\mathrm{m}$ shows a more erratic velocity behaviour due to the presence of the bore. After $t = 34\,\mathrm{s}$ the reflected wave results in both the positive velocities and the presence of a velocity signal at the onshore probes, showing that the water depth is larger than 3 cm.

2.4.2 Suspended sediment and morphodynamics

To compare the sediment concentrations we use the two lower OBS probes at the wing unit, because the upper two did not give usable data as they were not

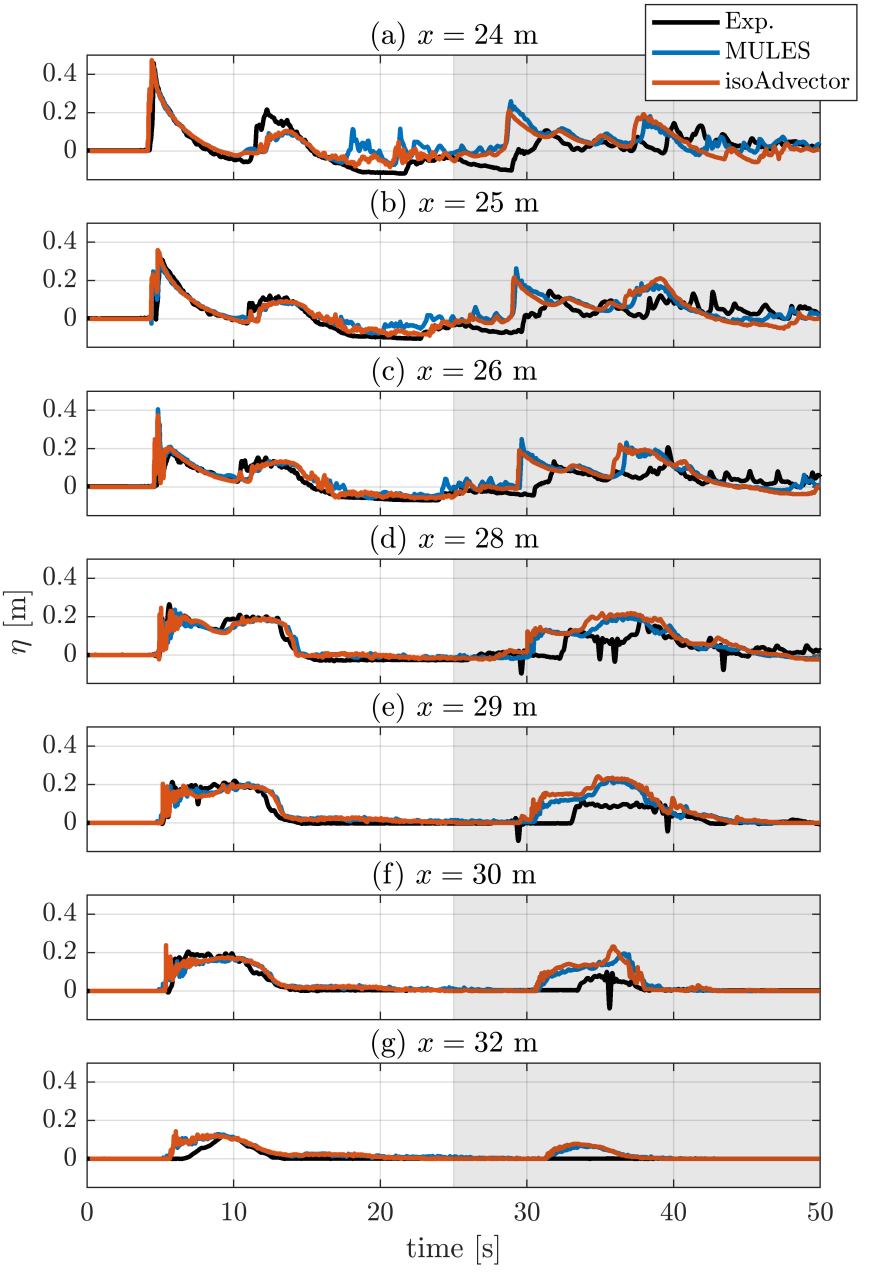

Figure 2.6
Comparison of surface elevation η between the experiments and two models. The last 25 seconds are shown with a gray background.

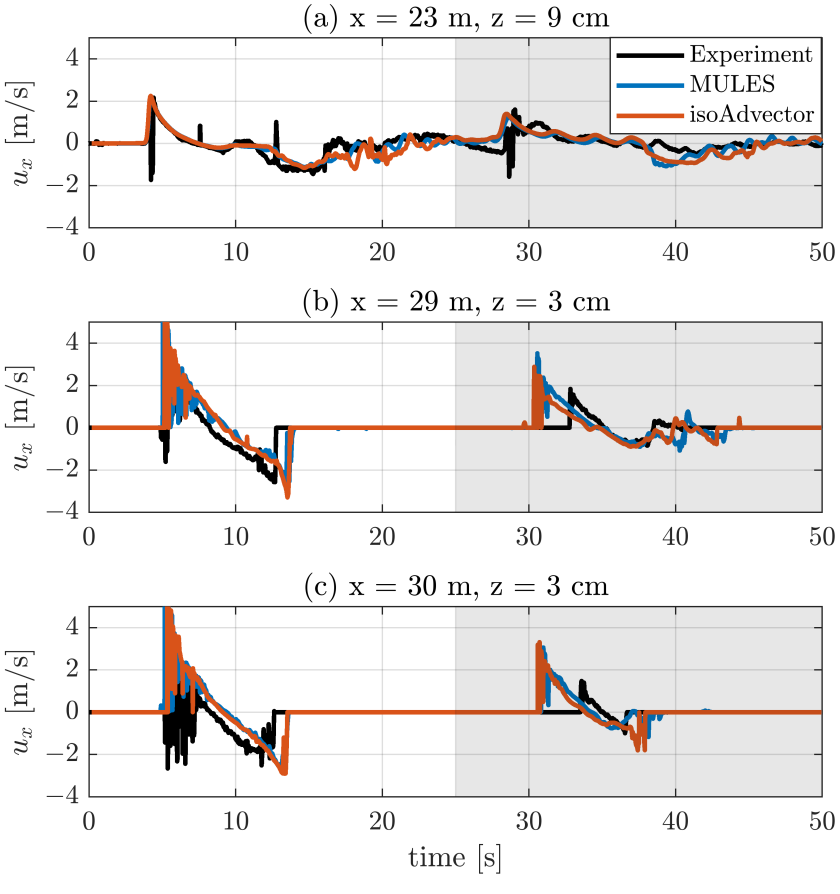

Figure 2.7
Comparison of cross-shore water velocity u_x between the experiments and two models, using MULES and isoAdvector respectively. Both models use the Engelund and Fredsoe (1976) reference concentration model. The last 25 seconds are shown with a gray background.

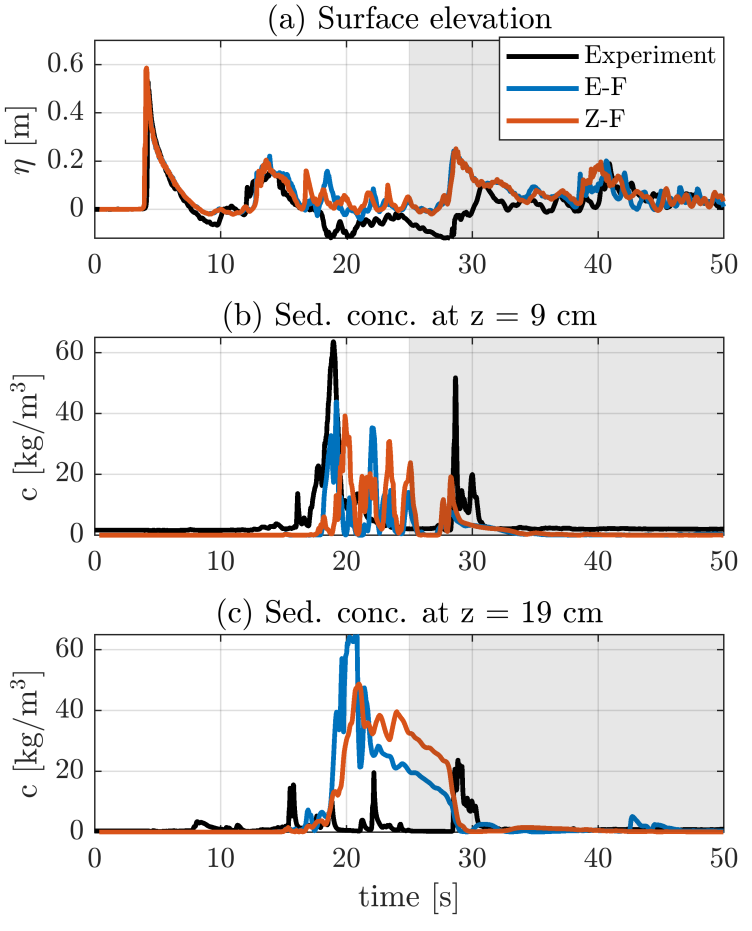

Figure 2.8
Comparison between measurements and models at the wing unit location ($x = 23\,\mathrm{m}$) showing surface elevation and sediment concentrations at 9 cm and 19 cm above the initial bed respectively. The sediment concentrations are modelled using the Engelund and Fredsoe (1976) and Zyserman and Fredsøe (1994) models respectively. Both models use the MULES VoF approach. The last 25 seconds are shown with a gray background.

continuously submerged (Young et al., 2010). A comparison between the measured and modelled concentrations at these locations can be seen in Figure 2.8, panels b and c. The corresponding nRMSE metrics are shown in Table 2.2. Since the cross-shore location is seaward of the breaking point, no sediment was entrained high enough in the water column during the uprush stage to be measured. During the backwash however, both the model and experiment features higher sediment concentrations. At 9 cm above the bed, the model and the experiments show peaks in concentration at around $t = 19\,\mathrm{s}$ and $t = 28\,\mathrm{s}$. However, in between these two peaks, the models both show peaks of higher concentrations which are not present in the measurements. Furthermore, at 19 cm the models overpredict the sediment concentration. Overall, the models do correctly predict no suspension of sediment during the uprush, and higher concentrations during the latter stages of the backwash. However, the details in the sediment concentrations are not well modelled. An explanation for this will be discussed in Section 2.6.3.

Figure 2.9 shows the morphodynamic change induced by the three consecutive solitary waves for the models using MULES and the two reference concentration models. Both models correctly predict that sediment has been picked up from the shore and deposited offshore. The models predict the correct location of maximum erosion, however the location of maximum deposition is more shoreward compared with the experiments. Both models show a slight underprediction of the maximum erosion depth and the maximum deposition height. They further develop small-scale bedforms between $x = 12\,\mathrm{m}$ and $x = 29\,\mathrm{m}$. These bedforms have a wavelength of $O(0.05\,\mathrm{m})$ and are roughly 1 cm high. The study by Young et al. (2010), however, does not mention the presence of ripples.

The modelled erosion and deposition volumes correspond well to the measurements (see Table 2.3). Specifically, the Engelund and Fredsoe (1976) model prediction comes very close to the experiments. The Zyserman and Fredsøe (1994) model, however, seems to slightly overpredict the transport volume. In that respect the model using Engelund and Fredsoe (1976) reference concentration is thus more accurate. It is important to recognize, however, that the measured erosion and deposition values differ quite significantly. This could be due to longshore nonuniformities not picked up over the measuring transect or inaccuracies in the measurement equipment. Still the erosion and deposition values provide a measure of the total amount of sediment moved. The RMST values similarly show that the profile produced by the EF model has better correspondence to the measured profile than the one produced by the ZF model.

Additional simulations were run where the MULES model was replaced by isoAdvector. The erosion and deposition volumes, and the RMST value for the isoAdvector model, are again shown in Table 2.3. As the table shows, the choice of VoF-scheme in this instance has a very limited impact on these metrics. The spatial differences between the profiles can be seen in Figure 2.10. Here, there are two clear differences between the profiles. Firstly, the morphology produced by the model using isoAdvector does not exhibit the small-scale bed undulations. Secondly, the isoAdvector model shows a slightly higher deposition and erosion peak. The fact that isoAdvector produces similar transport fluxes as MULES

Table 2.3
Integral transport volumes and Root-Mean-Square-Transport (RMST) values calculated for the experiments and models using Engelund and Fredsoe (1976) (EF), Zyserman and Fredsøe (1994) (ZF) and isoAdvector with EF (iso).

	Experiment	EF	ZF	iso
I_{ero} [m^2]	0.159	0.153	0.212	0.150
I_{dep} [m^2]	0.134	0.152	0.211	0.150
RMST [m^2]	-	0.0526	0.0750	0.0537

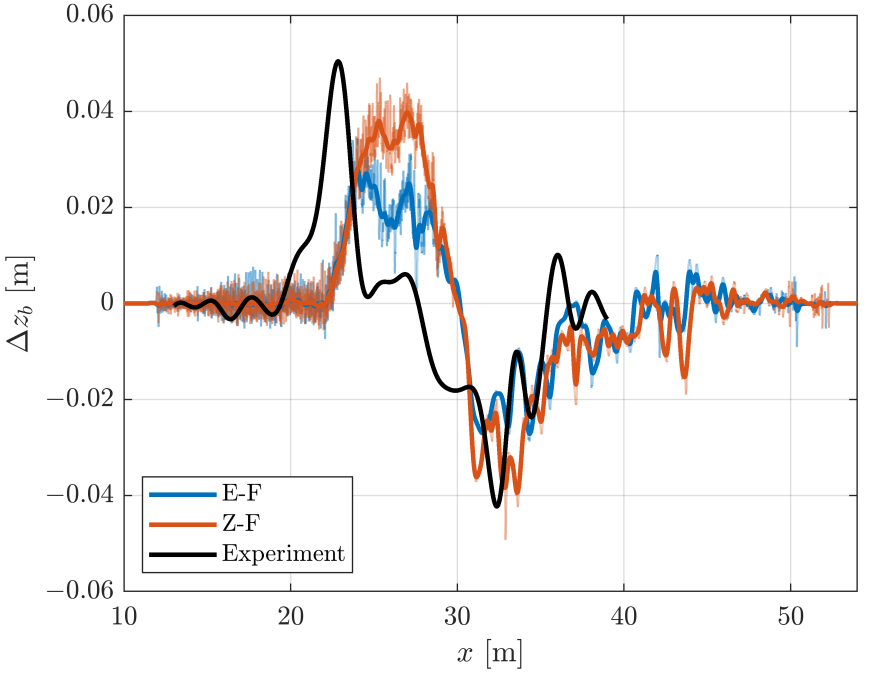

Figure 2.9
A comparison of measured and modelled bathymetric change (a) and the profiles (b) produced by the Engelund and Fredsoe (1976) (E-F) and Zyserman and Fredsøe (1994) (Z-F) models, after three consecutive solitary wave events. The thin line shows the original data and the thick line shows the same data after a Gaussian smoothing operation.

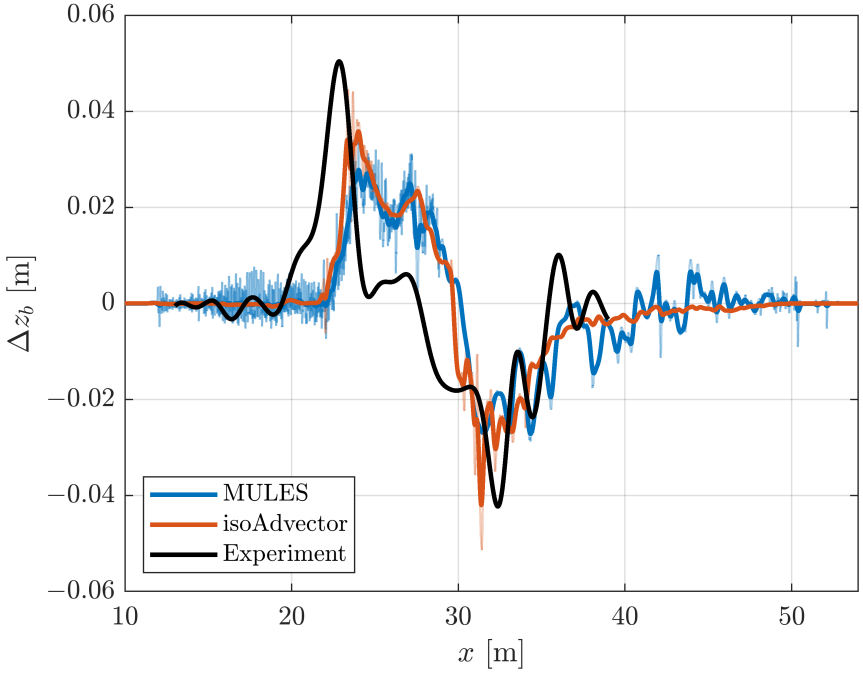

Figure 2.10
Comparison between morphology produced by models using MULES and isoAdvector. In both cases the Engelund and Fredsoe (1976) model was used to calculate the reference concentration. The thin lines show the original data and the thick lines show the same data after a smoothing operation.

confirms that the extra smoothing of the bedload in the isoAdvector simulations does not have a large influence on the overall transport. Given the extra cost in computational time and the comparatively small difference between the models, the remainder of the paper will use the MULES model.

2.5 Intra-swash sediment dynamics

The model allows us to investigate processes driving morphological change on different timescales. Here we will investigate the relative importance of bedload vs suspended transport, bed level change on an intra-swash timescale and the spatial distribution of suspended sediment. For this we use the MULES VoF method and the Engelund and Fredsoe (1976) model for the reference concentration to analyse intra-swash sediment dynamics for the first solitary wave.

Figure 2.11 shows spatial and temporal behaviour of the bed level, the runup

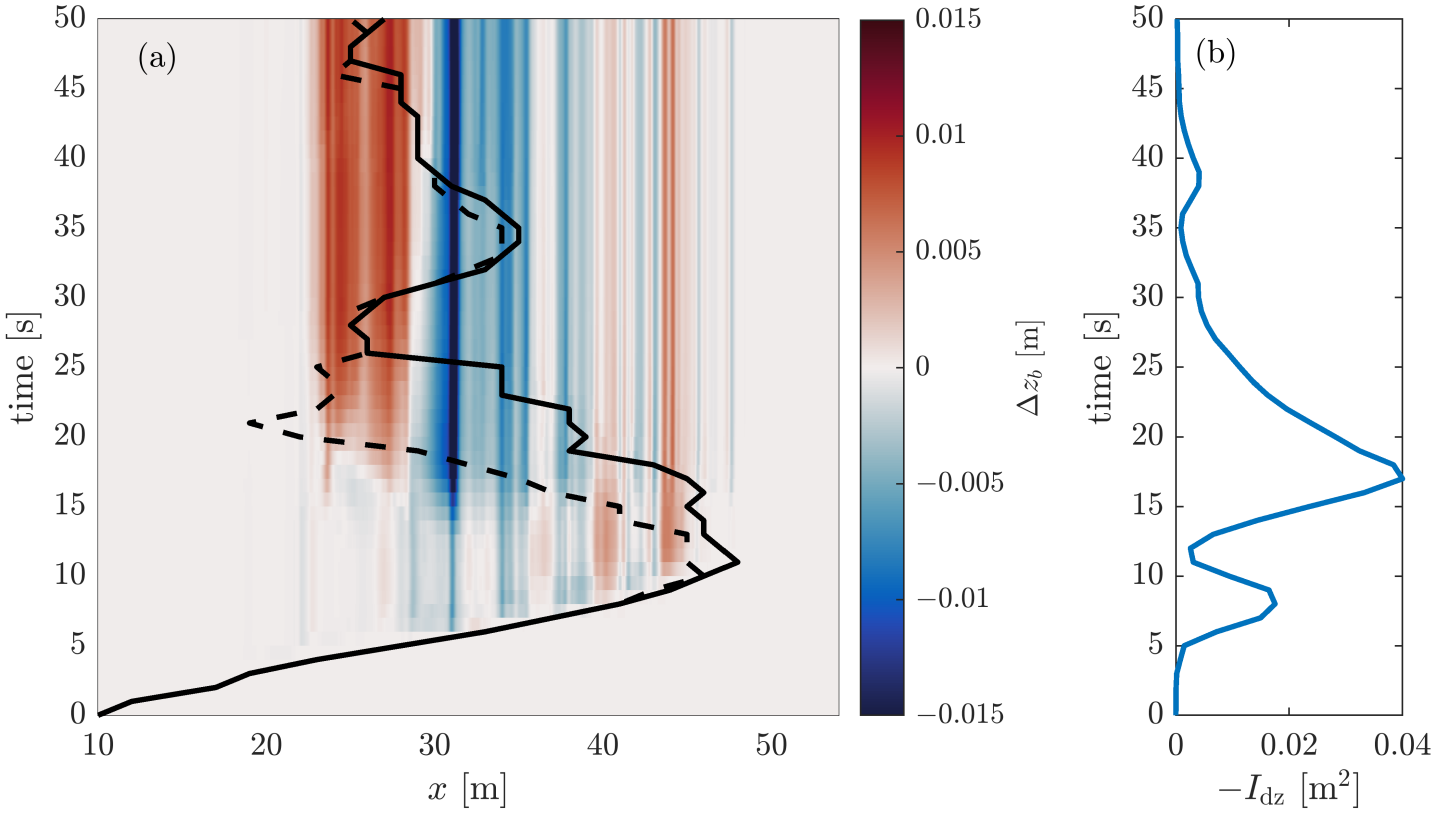

Figure 2.11
Figure showing the morphological change, runup and integrated bed level change over time, as predicted by the model. The black lines show the runup, defined as the maximum position where a certain increase in surface elevation compared with the initial condition is recorded (elevation of 1 cm for the straight line and 2 cm for the dashed line).

and the integrated bed level change, defined as

$$I_{\mathrm{dz}}(t) = \int_0^L \Delta z_b(t) \mathrm{d}x. \tag{2.15}$$

This can be thought of as a measure of the instantaneous amount of sediment in the water column. The figure shows that at $t = 5\,\mathrm{s}$, the first sediment starts to get into suspension. The majority of the uprush (between $t = 5\,\mathrm{s}$ and $t = 10\,\mathrm{s}$) is characterised by sediment being picked up from the bed. This leaves an area of erosion from roughly $x = 20\,\mathrm{m}$ to roughly $x = 43\,\mathrm{m}$. As the uprush decelerates at roughly $t = 9\,\mathrm{s}$ it loses its capacity to hold the sediment in suspension. Higher up the beach above $x = 43\,\mathrm{m}$ a small region of deposition forms. Meanwhile the integrated bed level change shows that the amount of suspended sediment briefly drops. $-I_{\mathrm{dz}}$ increases again after $t = 12\,\mathrm{s}$, when the backwash has become strong enough to pick up a larger volume of sediment. The suspended volume increases until $t = 16\,\mathrm{s}$. During this time significant erosion has occurred, mainly between $x = 30\,\mathrm{m}$ and $x = 40\,\mathrm{m}$. From this moment deposition starts to occur from around $x = 23\,\mathrm{m}$ to $x = 28\,\mathrm{m}$ and the amount of sediment in suspension steadily decreases. At around $t = 25\,\mathrm{s}$ the first swash event has ended and a second, smaller swash event is soon commencing. At this point there is still some sediment in suspension. The second swash event has a considerably smaller runup and its impact on the morphology is smaller; after roughly $t = 30\,\mathrm{s}$ the bed changes are minimal. Between $t = 35\,\mathrm{s}$ and $t = 40\,\mathrm{s}$ there is a small episode where the total suspended volume increases momentarily, but it soon drops again. At the end of the simulation the amount of sediment in suspension is negligible, allowing to perform subsequent model runs by starting with the final topography from the previous simulation.

The relative contributions of bedload and suspended load to the final bed morphology is shown in Figure 2.12. This shows that the majority of the large scale bed level change is due to suspended transport. Both modes of transport predict erosion and deposition at more or less the same locations. Because of the relative importance of suspended transport, we will further investigate how the suspended sediment is distributed in the water at different stages of the swash.

Figure 2.13 shows the water column and suspended sediment at different stages of the swash at the part of the beach where most sediment is deposited. Panels a and b show two snapshots of the uprush, just after the wave has broken. Here, near the swash tip at around $x = 32$ in panel (a), a region with high sediment concentration is seen. This region is followed by a region where plumes of sediment are formed by vortices that resulted from the wave-breaking process. Finally, behind the bore, a small layer of sediment, approximately 1 cm thick, can be seen at the bed. This layer does not reach high enough to be recorded at 9 cm above the bed, which explains the lack of a signal in Figure 2.8. These dynamics correspond well to the observed dynamics by Young et al. (2010) (see Figure 17 in their paper). Compared to panels $c - f$, showing the situation during backwash, the amount of sediment suspension is low. From around $t = 15\,\mathrm{s}$ to $t = 20\,\mathrm{s}$ the fast moving and sediment-rich backwash rushes into the slower moving water, generating a backwash bore. The subsequent deceleration of the flow leads to strong sedimentation in this

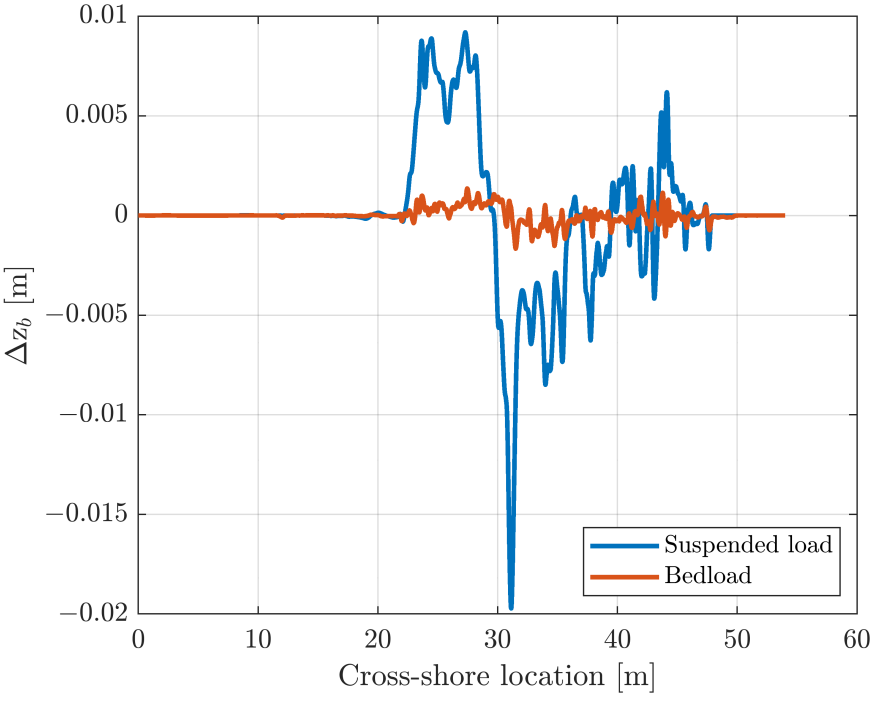

Figure 2.12
The relative contributions from bedload and suspended load to the total bed level change of the first modelled solitary wave. For clarity, the results have been smoothed using a Gaussian smoother.

region, which also can be seen in the decrease in $-I_{\mathrm{dz}}$ in Figure 2.11. Furthermore, just shoreward from $x = 23\,\mathrm{m}$ flow separation forces the sediment higher in the water column (Figure 2.13, panel *e*). From $t = 20\,\mathrm{s}$ to $t = 26\,\mathrm{s}$, much of the sediment slowly settles and gets diffused by turbulence, at the same times as the bore travels back up the beach.

2.6 Discussion

2.6.1 VoF and reference concentration models

The validation analysed two different VoF models and two different reference concentration models. Regarding the VoF models, isoAdvector showed a slight improvement over MULES in its morphodynamics (see Table 2.3) and resulting runup. This could be because MULES diffuses the interface between air and water, leading to the swash front having a high air content and thus experiencing less friction due to the lower effective density. The downside of using isoAdvector is that it makes the model less stable, presumably because of its sharper air-water interface producing larger gradients in density, making the solution less smooth. This could be extra pronounced due to the explicit time integration used to calculate the bed-level change. Still, the extra effort in stabilizing simulations with isoAdvector could be worthwhile due to its superior modelling of the interface.

Of the two reference concentration models, the Engelund and Fredsoe (1976) model performed better than the Zyserman and Fredsøe (1994) model in terms of the predicted erosion and deposition volumes. This is somewhat unexpected as the Zyserman and Fredsøe (1994) model was developed specifically to improve upon the sediment concentration predictions of Engelund and Fredsoe (1976) at higher Shields parameters. A possible explanation could be that the overpredicted runup means that a larger part of the beach is exposed to the swash flow and thus leads to larger amounts of sediment transport. This means that the present findings are likely affected by the discrepancies in the hydrodynamic predictions. Therefore, for future studies, an analysis of the performance of the reference concentration models is still warranted.

2.6.2 Runup and location of deposition

The validation also showed that the location of the deposition peak is predicted too far onshore compared to the measurements. A possible explanation for this is the overpredicted runup in the model. The overprediction effectively stretches out the uprush and backwash. This can be seen in Figure 2.6 where, after the uprush has passed, the water level takes longer time to decrease to the same level as in the experiments. Furthermore, the backwash velocities around $t = 12 - 16\,\mathrm{s}$ are underpredicted (see Figure 2.7). These two observations combined suggest that the strength of the backwash is weakened, which thereby influences the location of deposition to occur more onshore. The specific reason for the overpredicted runup

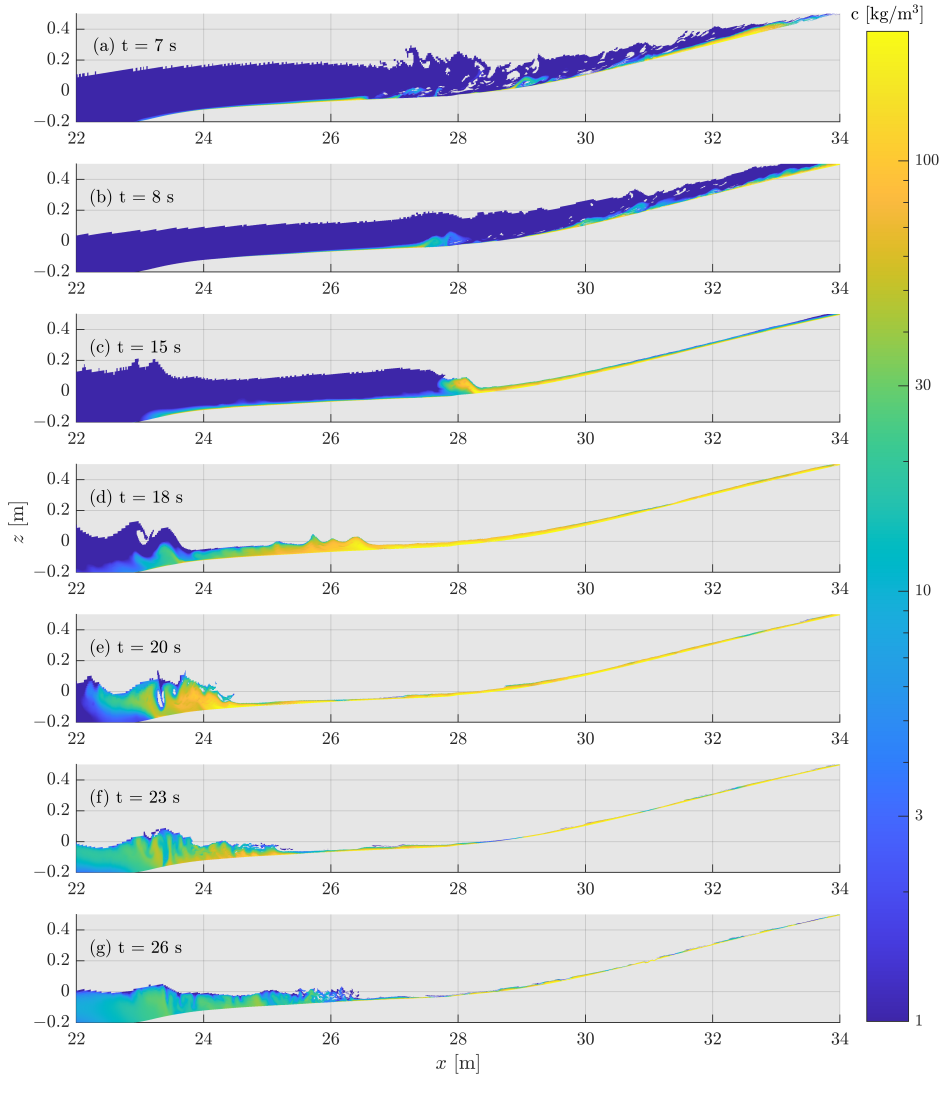

Figure 2.13
Figure showing snapshots at different times of the sediment concentration in the water. Here only cells containing at least 50% water are shown.

is unclear, however, it has been observed in other model studies. For instance, the study by Li et al. (2019), who used a similar model, also observed an overpredicted surface elevation higher up the beach.

One factor that influences the runup and is worth looking into is the bed roughness. Bed roughness has a great influence on hydrodynamics as well as on sediment transport and morphodynamics and is often used in morphodynamical models as a calibration parameter. Roughness is often thought of as a combined effect of skin-friction roughness and form-drag roughness. The former is incorporated in the model in terms of the Nikuradse roughness k_N. The latter is indirectly present due to small-scale bed forms generated by the model. However, the model can only represent bed forms that are larger than a couple of computational cells. This means that the model possibly neglects important contributions to the overall friction felt by the flow. Furthermore, effects that high sediment concentrations have on the local density and viscosity are not incorporated. Additionally, high amounts of turbulence could lead to an increased "apparent roughness" (Fredsøe et al., 2003).

To understand what possible influences an increased roughness could have, an additional simulation with a roughness of $k_N = 0.005\,\mathrm{m}$, 10 times larger than the previous case, was run. The morphodynamic results after three consecutive simulations using these two models are shown in Figure 2.14. The simulation with increased roughness produces substantially larger erosion and deposition volumes and an increased RMST value ($I_{ero} = 0.304\,\mathrm{m}^2$, $I_{dep} = 0.255\,\mathrm{m}^2$, RMST $= 0.091\,\mathrm{m}$). Additionally, the seaward limit of the modelled deposition peak now almost coincides with the measured deposition peak, which is an improvement over the case with default roughness values. Finally, the increased roughness has somewhat improved the maximum runup prediction from $x = 50\,\mathrm{m}$ to $x = 47\,\mathrm{m}$. From this it can be concluded that increasing the roughness comes at the cost of worse predictions in terms of the erosion and deposition volumes. The decrease in maximum runup stems directly from the additional friction in the model. The increase in sediment transport is expected, because the bed shear stress, driving sediment transport, is directly dependent on the skin-friction roughness.

The runup overprediction could stem from many different modelling and experimental aspects. Apart from bed friction, there are other processes that influence the runup that are not discussed in this paper. Possible candidates are the inclusion of infiltration and incorporating interparticle stresses present in high concentration flows. Furthermore, Kim et al. (2017) showed that the swash has pronounced 3D flow features. This affects both the measurements, where the runup depends on the transverse location (see the video provided with the paper of Young et al., 2010), and the model using a 2DV RANS approach where important 3D effects, such as 3D turbulence and the behaviour of air bubbles in the flow, are neglected. Further investigation of such processes is recommended to better understand their contributions to hydrodynamics and ultimately morphodynamics. However, given the morphodynamics results, we conclude that the runup in isolation is not necessarily an indicator of morphodynamic model performance.

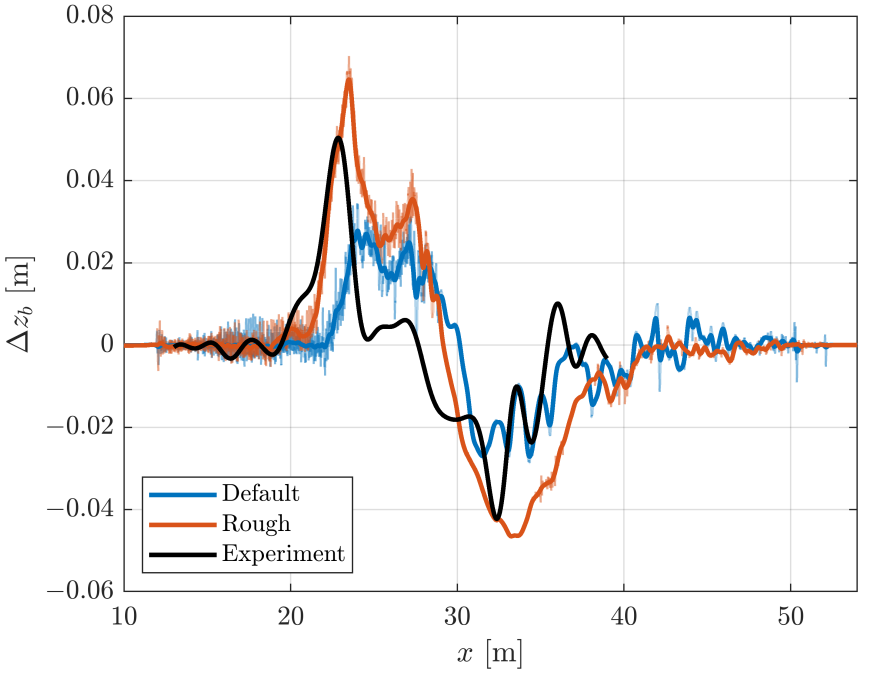

Figure 2.14
Modelled morphodynamic change when the roughness is increased by a factor of 10 compared to the default case. The thin lines shows the original data and the thick lines shows the same data after a smoothing operation.

2.6.3 Sediment transport and morphodynamics

The sampling of the concentration field is very sensitive due to variations in the simulated sediment concentration field that could lead to large differences in the sampled concentration. This could partially explain the discrepancies between the modelled and measured concentration time series (see Figure 2.8). It can be concluded that timing and order of magnitude of the sediment concentration are reasonably well modelled for the near bed sensor. However, at the upper sensor, the backwash induced sediment plume leads to high modelled sediment concentrations. To further add confidence to the sediment model, a comparison with a dataset containing more detailed sediment concentration measurements is desired, preferably measurements of vertical concentration profiles at different locations in the swash.

The ability to model sediment transport without making assumptions on sediment concentration profiles provides a great tool for better understanding sediment transport mechanisms (see for instance Figure 2.13). For instance, the model showed that the suspended sediment concentration displays large gradients and a strong vertical dependence. This extra information can be used to improve the predictions by depth-averaged models.

The suspended sediment concentration also varies strongly in time. As seen in Figure 2.11, during the latter stages of the uprush the suspended sediment volume reaches a maximum and declines as the flow reverses. Later, at the end of the backwash the suspended sediment volume reaches its global maximum. This metric does not give any information on the location of erosion and deposition. However, the fact that the suspended volume has a global maximum during the backwash is expected given the erosive bed response. It would be interesting to investigate how this metric behaves for different wave conditions, such as bichromatic or irregular waves. For instance, if the maximum of the suspension volume would occur during the uprush, this could be indicative of an accretive swash event. Particularly, given the difficulties of modelling accretive conditions (e.g. discussed in Ruffini et al., 2020), it would be interesting to analyse how the time series of sediment concentrations and swash velocities would differ between erosive and accretive wave conditions. The presented model is very suitable for such studies, since it can give both detailed temporal and spatial information on the suspended sediment load.

2.7 Conclusion

A depth-resolving model capable of modelling sediment transport and morphodynamics was applied to the morphodynamic modelling of a solitary wave on a sandy beach. To achieve this, an improvement to the modelling of boundary conditions was first necessary, as the default boundary implementation led to negative sediment concentrations near the bed. The new numerical scheme improves boundary behaviour under conditions of large Peclet numbers, which corresponds to the flow being advection dominated at the cell scale. This new scheme was validated

for both a 1D and 2DV analytical case. When this scheme was applied to the morphodynamic model, it no longer produced negative sediment concentrations.

The morphodynamic model was applied to the solitary wave experiments of Young et al. (2010). In terms of hydrodynamics, the model shows reasonable agreement in surface elevations and velocities, although a shallow layer of water leads to an overprediction of the runup by 8 to 10 m. Two different VoF models were assessed: MULES and isoAdvector. The latter showed much potential for use in the swash zone, but for a solitary wave the differences in hydrodynamics and sediment dynamics were not substantial.

In terms of sediment dynamics, the Engelund and Fredsoe (1976) reference concentration model produced the best results. The model showed good agreement with the measurements in terms of erosion and deposition volumes, however, the location of deposition is shifted landward. When the roughness was increased, the location of deposition and the runup improved. However, this came at the cost of the volume of sediment transported.

Although the runup is overpredicted, the improved numerics and adequate choice of reference concentration model means that the model can be used for temporal and spatial analysis of suspended sediment and morphodynamics, as demonstrated in this paper. Future studies could focus on how the model behaves for different wave scenarios, and what lessons can be learned for the improvement of depth-averaged models.

2.A Model equations

The hydrodynamic model solves the two-phase incompressible RANS equations:

$$\frac{\partial \rho u_i}{\partial t} + \frac{\partial \rho u_i u_j}{\partial x_j} = -\frac{\partial p^*}{\partial x_i} - g_j x_j \frac{\partial \rho}{\partial x_i} + \frac{\partial}{\partial x_j}\left(2 S_{ij} \mu + \tau_{ij}\right), \tag{2.16}$$

$$\frac{\partial u_i}{\partial x_i} = 0. \tag{2.17}$$

Here u_i are the Reynolds averaged velocity components, ρ is the density, p^* is the excess pressure over the hydrostatic potential, x_i are the cartesian components, S_{ij} is the mean strain rate tensor defined as

$$S_{ij} = \frac{1}{2}\left(\frac{\partial u_i}{\partial x_j} + \frac{\partial u_j}{\partial x_i}\right), \tag{2.18}$$

μ is the dynamic molecular viscosity and τ_{ij} is the Reynolds stress, which is defined using the dynamic eddy viscosity ν_t and using the Boussinesq hypothesis:

$$\tau_{ij} - \bar{u_i' u_j'} = 2\nu_t S_{ij} - \frac{2}{3} k \delta_{ij}, \tag{2.19}$$

where δ_{ij} is the Kronecker delta. The turbulent kinetic energy k is defined as

$$k = \frac{1}{2}\bar{u_i' u_j'}, \tag{2.20}$$

where the bar denotes ensemble averaging, and the prime signifies the fluctuating velocity component.

The turbulence closure equations for k and ω are defined as

$$\frac{\partial \rho k}{\partial t} + \frac{\partial \rho u_j k}{\partial x_j} = P_k - \rho\beta^* k\omega + \frac{\partial}{\partial x_j}\left[\left(\mu + \rho\sigma^* \frac{k}{\omega}\frac{\partial k}{\partial x_j}\right)\right], \tag{2.21}$$

$$\frac{\partial \rho \omega}{\partial t} + \frac{\partial \rho u_j \omega}{\partial x_j} = P_\omega - \rho\beta\omega^2 + \rho\frac{\sigma_d}{\omega}\frac{\partial k}{\partial x_j}\frac{\partial \omega}{\partial x_j} + \frac{\partial}{\partial x_j}\left[\left(\mu + \rho\sigma \frac{k}{\omega}\frac{\partial \omega}{\partial x_j}\right)\right]. \tag{2.22}$$

Here P_k and P_ω are the production terms for k and ω respectively and defined as

$$P_k = p_0 \nu_t, \quad P_\omega = \alpha\frac{\omega}{\tilde{\tilde{\omega}}} p_0, \quad p_0 = 2S_{ij}S_{ij}, \tag{2.23}$$

and

$$\sigma_d = H\left(\frac{\partial k}{\partial x_j}\frac{\partial \omega}{\partial x_j}\right)\sigma_{do}, \tag{2.24}$$

with H being the Heaviside function.

In accordance with Larsen and Fuhrman (2018) the eddy viscosity is defined as

$$\nu_t = \frac{k}{\tilde{\omega}}\sigma_{do}, \tag{2.25}$$

where

$$\tilde{\tilde{\omega}} = \max\left(\omega, \lambda_1\sqrt{\frac{p_0}{\beta^*}}\right), \quad \tilde{\omega} = \max\left(\tilde{\tilde{\omega}}, \lambda_2\frac{\beta}{\beta^*\alpha}\frac{p_0}{p_\Omega}\omega\right), \tag{2.26}$$

with $p_\Omega = 2\Omega_{ij}\Omega_{ij}$, where Ω_{ij} is the mean rotation rate tensor. The constants are defined to their default values: $\alpha = 0.52$, $\beta = 0.00708$, $\beta^* = 0.09$, $\sigma = 0.5$, $\sigma^* = 0.6$, $\sigma_{do} = 0.125$, $\lambda_1 = 0.2$ and $\lambda_2 = 0.05$.

The VoF method is incorporated using an indicator field φ which is used to determine the density and viscosity of the air/water mixture in each cell. No surface tension effects are employed in this model.

Acknowledgements

This work was carried out on the Dutch national e-infrastructure with the support of SURF Cooperative. We would like to thank Bjarke E. Larsen for the fruitful discussions about turbulence modelling and runup overprediction, as well as Johan Roenby for helping with the implementation of isoAdvector. We also thank one anonymous reviewer for their very informative and constructive feedback on an earlier version of the manuscript.

Chapter 3

Depth-resolved modelling of intra-swash sand transport by bichromatic waves: importance of bubbles, wave-breaking turbulence and vertical structures

Abstract

Depth-resolving models provide the ability to investigate vertical structures in the flow and sediment concentrations in the swash zone. These vertical structures are typically not included in the calculations of the cross-shore suspended transport flux in depth-averaged models, where instead the cross-shore velocity and sediment concentrations are assumed to be vertically uniform. To assess the validity of this assumption, we simulate the flow and suspended sediment transport induced by bichromatic waves using a 2DV depth-resolving RANS model. First, the model performance is verified. Here we show that special care needs to be taken to deal with bubbles in 2DV simulations. Furthermore, we show that turning off the Wilcox (2006, 2008) limiter for turbulence increases the modelled turbulent kinetic energy induced by wave-breaking, which improves predictions of sediment concentrations. The model shows that vertical structures are important in the swash zone and, if one assumes vertically uniform velocities and concentrations, one can overpredict the sediment flux by 50%. This is an important consideration for the use of depth-averaged models in the swash zone.

3.1 Introduction

The swash zone is the dynamic region of the beach where sea meets land. Here, waves intermittently cover and expose the beach face. This region is characterised by strong shallow flows, large amounts of turbulence and the presence of waves breaking and air bubbles (Masselink and Puleo, 2006). These dynamics can lead to large sediment transport fluxes and strong intraswash bed level changes on the order of centimetres in seconds (Blenkinsopp et al., 2011; Van der Zanden et al., 2019a), which make it difficult to study important morphological processes experimentally. Here, numerical models can provide a valuable tool to complement measurements for understanding and ultimately predicting the dynamics of the swash zone.

There exist many different model approaches for understanding intraswash dynamics. A summary of existing model techniques is given by Briganti et al. (2016). A distinction can be made between models are the so-called depth-averaged and depth-resolving models. Depth-averaged models are comparatively computational efficient due to them being of lower dimensionality. These models can give a lot of insight into important processes driving morphodynamics (see e.g. Reniers et al., 2013; Incelli et al., 2016; Zhu and Dodd, 2020). However, they have difficulty reproducing intraswash sediment dynamics, in particular suspended sediment transport (Ruffini et al., 2020; Mancini et al., 2021).

An important process for the suspended sediment transport is turbulence (Fredsøe and Deigaard, 1992). For instance, Sumer et al. (2013) showed experimentally that eddies created during the wave-breaking process can lead to strong sediment suspension. There also exist some depth-averaged model studies on turbulence and sediment interaction. For instance, Alsina et al. (2009) modelled turbulence using a modified version of the model by Deigaard et al. (1986) and found the contribution of bore-generated turbulence essential to achieve accurate cross-shore suspended sediment transport compared with measurements. Zhu and Dodd (2020) used a different approach by estimating the turbulent kinetic energy from data instead. They found that bore-generated turbulence dominated the sediment entrainment, being more important than entrainment from pure shear.

A different but related process is the vertical distribution of suspended sediment and the vertical velocity profile (Aagaard et al., 2021). For instance, the aforementioned study of Sumer et al. (2013) shows that turbulent eddies can rapidly entrain sediment high into the water column, putting clouds of sediment above regions with lower sediment concentration. This was also seen in the model results of Kranenborg et al. (2022), especially in the presence of a backwash bore. The recent depth-averaged study of Mancini et al. (2021) argued that, at least in-part, the difficulty in modelling suspended transport is due to uncertainties in the vertical structure of sediment transport.

Many depth-averaged models do incorporate parametrisations to deal with these vertical nonuniformities. For instance, Mancini et al. (2021) uses a bottom boundary layer model, based on a friction coefficient, to account for the vertical profile of the cross-shore velocity. Similarly, for calculating the sediment deposition,

they use a power-law profile (Soulsby, 1997) to calculate the near-bed sediment concentration. The method of Galappatti and Vreugdenhil (1985), as for instance used by Reniers et al. (2013), uses a different concept to account for the flow conditions, introducing an equilibrium sediment concentration and an adaptation time. These examples all implement information on the vertical profile in one way or another. However, crucially this is only applied for calculations of the erosion and deposition fluxes, not for the cross-shore flux of sediment. The importance of vertical structures in this latter term is not well understood.

Depth-resolving models do not have this fundamental issue. Because they include the vertical dimension explicitly in the model, no a-priori assumptions on vertical distribution of sediment concentrations and velocities are necessary. There are different ways of approaching both the flow and sediment modelling in a depth-resolving way. In this study we limit ourselves to using the Reynolds Averaged Navier Stokes approach, combined with modelling suspended sediment as a passive scalar that is transported and diffused with the flow. Such models have been used previously to analyse breaker bar morphodynamics (Jacobsen and Fredsoe, 2014a,b) and swash-zone morphodynamics induced by solitary waves (Li et al., 2019; Kranenborg et al., 2022). These studies all use roughly the same model, based on the original model by Jacobsen et al. (2014), implemented in the OpenFOAM framework. This model uses the Volume of Fluid (VoF) method to discriminate between air and water in the solution. Recently, a different model based on the IH2VOF model was used to study morphodynamics and intraswash suspended sediment dynamics under bichromatic waves (García-Maribona et al., 2021, 2022). An important difference between these two studies and the studies by Li et al. (2019) and Kranenborg et al. (2022), is that the latter uses a different implementation of the VoF method. Where typical VoF implementations compute the RANS equations in both the air and water phases, they instead compute the RANS equations in the water phase only. The presence of an air phase means that bubbles can be formed, which can influence the water part of the solution.

In this paper, we investigate the importance of wave-breaking turbulence and vertical nonuniformities for sediment transport in the swash zone. To this end we use the model by Kranenborg et al. (2022). First, we will investigate the effects of bubbles in the model on the swash flow. Furthermore, the effects of the turbulence limiter introduced by Wilcox (2006, 2008) (hereafter only referred to as Wilcox (2006)) are investigated. Finally, we use the depth-resolved model to study how nonuniform vertical structures in suspended sediment concentration and flow velocity are, and how these influence the calculated suspended sediment flux. To study these processes we formulate the following research questions for this paper:

- How do bubbles behave in a 2DV model and how does this influence sediment transport predictions by the model?
- What is the influence of the Wilcox (2006) limiter on wave-breaking turbulence and sediment transport?
- How do vertical structures in sediment concentration and flow velocity influ-

ence the sediment transport flux?

In the following sections the research methodology is described (Section 3.2). Section 3.3 presents the model verification and the role of bubbles and wave-breaking turbulence and in Section 3.4 uses the model to analyse the importance of vertical structures in the suspended sediment transport flux. The results are subsequently discussed in Section 3.5 and the research questions are answered in 3.6.

3.2 Methodology

We start by describing the experimental conditions used as a basis for the analysis. Subsequently, the model and its implementation, domain and initial and boundary conditions are described. Finally, the definitions of metrics and analysis tools are laid out.

3.2.1 Experiment description

To investigate sediment transport and vertical structures therein, we need an experiment that includes the relevant processes. To this end solitary waves are too simple as they do not produce wave-swash interactions, or the advection of pre-suspended sediment, both processes which are often thought to be important (Van der Zanden et al., 2019b). Furthermore, we need detailed time-series of suspended sediment concentrations and velocities to verify the model performance. For these reasons, we opt to use the bichromatic wave experiments by Van der Zanden et al. (2019a). This enables both an analysis of suspended sediment which includes processes mentioned above, and makes it possible to make averages over wave group repetitions.

Of the experiments done by Van der Zanden et al. (2019a), we specifically use wave run no 5, which starts at 180 minutes after the first wave run (see Figure 3.1 for the initial profile of run 5). The experiments were conducted in the large-scale CIEM wave flume at the Universitat Politéchnica de Catalunya in Barcelona, Spain. The flume is 100 m long and 3 m wide, in which a sediment bed with an initial slope of 1:15 was built. This bed consists of medium sand with sand characteristics $D_{50} = 0.25\,\mathrm{mm}$, $D_{10} = 0.15\,\mathrm{mm}$ and $D_{90} = 0.37\,\mathrm{mm}$. The mean sediment settling velocity was measured as $w_s = 0.034\,\mathrm{m/s}$.

The waves were generated as a first order bichromatic wave with two wave components. The wave group period was $T_{gr} = 14.8\,\mathrm{s}$ with a wave repetition period $T_r = 2T_{gr}$, meaning that every repetition consisted of two different wave groups. The individual wave components had periods $T_1 = T_r/7$ and $T_2 = T_r/9$ and wave heights $H_1 = H_2 = 0.32\,\mathrm{m}$. Together the wave components have a mean short wave period of $T_m = T_r/8 = 3.7\,\mathrm{s}$. Although the experimental facility has the capability of absorbing waves, this was not active during the experiments. This has effects on the local hydrodynamics in the experiments (see e.g. the discussion in Van der A et al., 2017), but also means that the waves in the model will be slightly different

as the relaxation zones in the model means that incoming waves are absorbed at the paddle.

The measurements featured an array of measuring equipment. The full description can be found in the original paper of Van der Zanden et al. (2019a). In this study we use the acoustic wave gauges, the ADV probes for measuring flow velocities and OBS probes for measuring sediment concentrations. Figure 3.1 shows the location of the instruments. The OBS and ADV probes were mounted 3 cm above the bed at the start of the wave run.

3.2.2 Model description

We use the model of Kranenborg et al. (2022), which was adapted from the model of Jacobsen et al. (2014), to use in the swash zone. Although the model is capable of morphodynamic simulations, in this study we limit ourselves to modelling suspended sediment transport only and not take intraswash morphodynamics into account. In other words, we run the model using a static bed but still allow suspended sediment to entrain and settle.

The model is defined on a 2D spatial domain $\mathcal{D} \subset \mathbb{R}^2$, where we define the Cartesian coordinates in two notations, $(x_1, x_2) = (x, y)$, with its origin at the still water line and positively directed towards the beach and up respectively. Throughout the paper we use the x and y coordinates for analysis, but for the description of the model equations we use Einstein notation. t refers to the time coordinate. In total, we run the simulations from $t_0 = 30\,\mathrm{s}$ to $t_{end} = 240\,\mathrm{s}$. This is because the paddle was essentially stationary for the first 30 s.

Implementation

The model solves the 2DV incompressible RANS equations and uses the Volume of Fluid (VoF) method for discriminating between air and water. Specifically, we use the isoAdvector approach of Roenby et al. (2016). This introduces a volume fraction field α with which in each cell fluid properties ψ are set using

$$\psi = \alpha\psi_{water} + (1-\alpha)\psi_{air}. \tag{3.1}$$

To close the flow equations we use the $k-\omega$ turbulence model, incorporating the Wilcox (2006) and Larsen and Fuhrman (2018) limiters, defined here in Einstein notation following the conventions of Larsen and Fuhrman (2018):

$$\frac{\partial \rho k}{\partial t} + \frac{\partial \rho u_j k}{\partial x_j} = 2\nu_t S_{ij} S_{ij} - \rho\beta^* k\omega + \frac{\partial}{\partial x_j}\left(\mu + \rho\sigma^* \frac{k}{\omega}\frac{\partial k}{\partial x_j}\right), \tag{3.2}$$

$$\frac{\partial \rho \omega}{\partial t} + \frac{\partial \rho u_j \omega}{\partial x_j} = \alpha_\omega 2\frac{\omega}{\tilde{\tilde{\omega}}} S_{ij} S_{ij} - \rho\beta\omega^2 + \rho\frac{\sigma_d}{\omega}\frac{\partial k}{\partial x_j}\frac{\partial \omega}{\partial x_j} + \frac{\partial}{\partial x_j}\left(\mu + \rho\sigma\frac{k}{\omega}\frac{\partial \omega}{\partial x_j}\right), \tag{3.3}$$

k being the turbulent kinetic energy density and ω being the specific dissipation rate. The mean strain rate tensor is defined as

$$S_{ij} = \frac{1}{2}\left(\frac{\partial u_i}{\partial x_j} + \frac{\partial u_j}{\partial x_i}\right), \tag{3.4}$$

with u_i and x_i are the velocity and spatial coordinate components. ρ is the density, μ and ν are the dynamic molecular viscosity and the kinematic viscosity respectively, which all depend on the volume fraction field α. Furthermore, $\beta = 0.708$, $\beta^* = 0.09$, $\sigma^* = 0.6$, $\sigma_{do} = 0.125$, $\sigma = 0.5$, $\alpha_\omega = 0.52$ and

$$\sigma_d = H\left(\frac{\partial k}{\partial x_j}\frac{\partial \omega}{\partial x_j}\right)\sigma_{do} \tag{3.5}$$

are all model parameters (with H being the Heaviside step function). Here the turbulent eddy viscosity ν_t is defined as

$$\nu_t = \frac{k}{\tilde{\omega}}. \tag{3.6}$$

It remains to define the two limited versions of ω:

$$\tilde{\tilde{\omega}} = \max\left(\omega, \lambda_1\sqrt{\frac{p_0}{\beta^*}}\right), \quad \tilde{\omega} = \max\left(\tilde{\tilde{\omega}}, \lambda_2\frac{\beta}{\beta^*\alpha}\frac{p_0}{p_\Omega}\omega\right), \tag{3.7}$$

where $p_0 = 2S_{ij}S_{ij}$, $p_\Omega = 2\Omega_{ij}\Omega_{ij}$, with

$$\Omega_{ij} = \frac{1}{2}\left(\frac{\partial u_i}{\partial x_j} - \frac{\partial u_j}{\partial x_i}\right). \tag{3.8}$$

Following Larsen and Fuhrman (2018) we use $\lambda_2 = 0.05$ and $\lambda_1 = 0.875$ by default. Later in the paper, the Wilcox (2006) limiter will be deactivated by setting $\lambda_1 = 0$.

We do not apply a buoyancy production term as this can lead to stability issues around wave-breaking and it does not lead to considerable differences in modelled morphodynamics (Christoffersen, 2019). For wave generation we use the waves2Foam module (Jacobsen et al., 2012), coupled with OceanWaves3D (OW3D) (Engsig-Karup et al., 2009; Paulsen et al., 2014).

We model suspended sediment transport using an advection diffusion approach where the evolution of the sediment concentration field c is modelled as

$$\frac{\partial c}{\partial t} + (\alpha u_i + w_s\delta_{i3})\frac{\partial c}{\partial x_i} - \frac{\partial}{\partial x_i}\left[\alpha(\nu + \nu_t)\frac{\partial c}{\partial x_i}\right] = 0, \tag{3.9}$$

where δ_{i3} is the kronecker delta and the sediment is advected by the sum of the flow velocity and the fall velocity w_s, which is calculated following the method of Fredsøe and Deigaard (1992). Sediment is diffused by the sum of the fluid kinematic viscosity and the eddy viscosity ν_t. For details of the implementation we refer to the initial publication on the model by Jacobsen et al. (2014).

Model geometry and mesh

Figure 3.1 shows the setup of the model, consisting of different zones where different models are run. The full model domain, reaching from the seaside to above the swash, is 87 m long. At the seaward side, the water depth is $h_0 = 2.5\,\mathrm{m}$. As

written above, the full model consists of two different models that are coupled together using a relaxation zone. The OW3D model is run on the full domain, from the seaward boundary at $x_p = -75.97\,\mathrm{m}$ up to $x = 11.03\,\mathrm{m}$. The domain of the depth-resolving OpenFOAM model starts at $x = -50.47\,\mathrm{m}$ and reaches to $x = 11.03\,\mathrm{m}$ at the upper swash boundary. The region between $x = -50.47\,\mathrm{m}$ and $x = -41.97\,\mathrm{m}$ defines the relaxation zone where the solution of OW3D is mapped onto the depth-resolving model. Details about the relaxation zone method and the mapping can be found in Jacobsen et al. (2012).

The geometry of the depth-resolving model domain follows the measured bed profile before the experiment run took place (see Section 3.2.1 below). The profile was measured from approximately $x = -22.3\,\mathrm{m}$ upward. The profile offshore from this point was assumed to be linear with a slope of 1:15 until the toe of the profile at depth $y = -h_0$. The domain height generally is 3.3 m, except at the sloped section where the top of the domain is a straight line, with endpoints 3.3 m above the bottom profile.

The mesh is created by rectangular cells with a cross-shore length of 4 cm. The vertical discretisation is done in three layers. This is done to facilitate a high resolution at the bed boundary while keeping the aspect ratio small in the majority of the domain. The bottom layer is 10 cells thick with all cells being 0.625 mm thick. This layer follows the bed geometry. The top layer is 2.3 m thick and consists of 140 cells with the same thickness (approximately 16.4 mm). This layer follows the top, linear boundary geometry. The middle layer, consisting of 177 cells, facilitates a smooth transition between the two outer layers.

The OW3D model is discretized in 1000 equidistant points in the x-direction.

Boundary conditions and wave generation

The boundary conditions are very similar to the Kranenborg et al. (2022) study, with no-slip boundary conditions at the bed, offshore and onshore boundaries, and an ambient atmospheric pressure condition at the top boundary, from which the velocity condition is calculated. We use the Fuhrman et al. (2010) boundary conditions for k and ω at the bed. We use the Cebeci and Chang (1978) rough wall model, implemented by Larsen et al. (2017) for modelling the friction velocity and incorporating the bed roughness. For this we use a Nikuradse roughness height of $k_N = 2.5D_{50}$, where D_{50} denotes the median grain size.

For sediment transport we use the Zyserman and Fredsøe (1994) reference concentration to determine the suspended sediment concentration C at the reference height y_a above the bottom boundary. Here we also use the new divergence scheme proposed in Kranenborg et al. (2022) to stabilise the sediment concentrations at the boundary, mitigating wiggles and negative sediment concentrations (Jacobsen, 2011). The Zyserman and Fredsøe (1994) approach requires the Shields parameter θ as input, which we here define as

$$\theta = \frac{|\tau_b|}{(\rho_s - \rho)gD_{50}}, \tag{3.10}$$

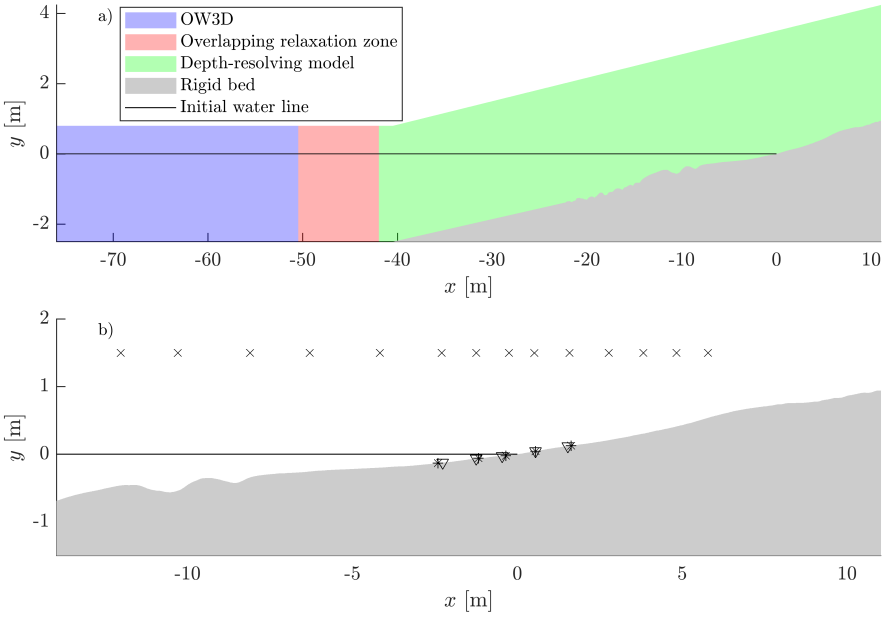

Figure 3.1
Schematic showing (a) the depth-resolving model domain and the regions where only the OW3D model is run, the overlapping relaxation zone and the depth-resolving model. Panel (b) shows the area around the still water line and the probes used in the paper. Here crosses show positions of wave gauges, triangles show ADV probes and stars show OBS probes.

where τ_b is the bed shear stress as calculated using the turbulence model, $\rho_s = 2650\,\mathrm{kg/m^3}$ is the sediment density, ρ is the fluid density and $g = 9.81\,\mathrm{m/s^2}$ is the magnitude of the gravitational acceleration. We here define the Shields parameter to always be positive.

We generate the waves at the offshore boundary in the domain. Similar to Chen et al. (2022); Jacobsen et al. (2018), we apply the OW3D model to incorporate the paddle velocity signal. In our study, we do not use the paddle velocity signal u_p directly but modify it by a scaling factor γ_p to create the model paddle velocity u_p^m:

$$u_p^m = \gamma_p u_p. \tag{3.11}$$

This is because the paddle in the experiments is of the wedge type, which has is different from the model paddle in two important ways. For one, the laboratory paddle has a vertical component in its stroke movement where the model paddle only allows horizontal movement. Secondly, because of the nonhorizontal paddle stroke, the laboratory paddle does not contact the water for the full flume depth h_0, which is the case in the model. The calibration process was done by comparing modelled surface elevations using paddle signals produced by a gamma varying between 1 and 0.7, with an interval of 0.05. In the end, $\gamma_p = 0.75$ gave the best results. We do not give more details on this calibration here, but refer to the general model verification in Section 3.3.

The OW3D model assumes a constant depth of h_0, and as such does not include the bottom geometry. This is not an issue, as the coupling between the models is one-way only, and this is done before the toe of the bed profile. At the landward end of the OW3D domain, a damping zone is used to absorb the waves.

3.2.3 Model verification

To aid in verification of the model performance, a normalised Root Mean Square Error (nRMSE) is calculated for the water surface, flow velocities and the sediment concentrations. For the free surface location we use the deviation from the initial water depth η. For the flow velocity comparison, the normalisation variable is the maximum of the absolute value of the velocity. Furthermore, dry periods in the measurement data (measurements were done at 3 cm above the bed) were removed from the data before comparison. The latter point also holds true for comparisons of sediment concentration

3.2.4 Analysis of cross-shore fluxes

To calculate the advective cross-shore flux F at a certain position we integrate the local sediment transport flux. This is done in the following manner:

$$F = \int_{y_b+y_a}^{y_{top}} c(y)u_x(y)\mathrm{d}y, \tag{3.12}$$

where $c(y)$ and $u_x(y)$ describe the suspended sediment concentration and the cross-shore velocity at depth y. Here y_b is the bed level, y_a is the reference height used

for the suspended sediment boundary condition and y_{top} is the upper bound of the domain at the particular cross-shore location. The integration bounds include parts of the domain that are filled with air. This works because effectively there is no sediment in the domain above the free surface.

As a proxy for depth-averaged models, we can similarly define a flux F_u by first averaging the velocity and integrating the sediment concentration over depth:

$$F_u = UC, \tag{3.13}$$

where U is defined as

$$U = \frac{1}{h - y_a} \int_{y_b + y_a}^{y_{top}} u_x(y)\alpha(y)\mathrm{d}y, \tag{3.14}$$

with α being the volume fraction of air and water, and the water depth h defined as

$$h = \int_{y_b}^{y_{top}} \alpha(y)\mathrm{d}y, \tag{3.15}$$

and the depth integrated concentration C is defined as

$$C = \int_{y_b + y_a}^{y_{top}} c(y)\mathrm{d}y. \tag{3.16}$$

Note that for ease of comparison, both fluxes are calculated in the suspension part of the domain only.

We then define the difference between these fluxes as

$$\Delta_F = F - F_u, \tag{3.17}$$

which means Δ_F can be interpreted as the signed remainder of the flux that is needed when modelling the flux assuming vertically uniform sediment and velocity distributions.

Depth-averaged models that model suspended sediment transport often employ a similar advection diffusion model where sediment is transported using the flow velocity. However, because of vertical nonuniformities, one could use a different velocity U_c, here called the effective transport velocity, as the advection velocity in the transport equation. Using this, we can redefine the depth-averaged flux given in Equation (3.13) by substituting the depth-averaged velocity U with the effective transport velocity U_c and equate it to the flux defined in equation (3.12):

$$U_c C = F \iff U_c = \frac{F}{C}. \tag{3.18}$$

This gives us a way to analyse the effective transport velocity in a depth-averaged approach, in terms of the depth-integrated sediment concentration and the depth-resolved sediment flux. Note that for small fluxes F this equation becomes very sensitive. This happens for instance when the water depth becomes very low. For

Table 3.1
The definitions of the four different model configurations.

Config	Wilcox (2006) limiter	Bubble modification
A	on	off
B	on	on
C	off	off
D	off	on

this reason, both fluxes and the effective transport velocity are assumed to be zero when the water depth is lower than 0.5 cm.

We define the difference between the velocities Δ_U as

$$\Delta_U = U - U_c. \tag{3.19}$$

It is important to note that, while we use the above defined metrics as methods to compare with a depth-averaged, or depth-uniform, approach, the calculation of F_u is still based on the depth-resolving model. These assumptions and their impact on the interpretation of the analyses using this is further discussed in Section 3.5.4

For all integrals above the numerical integration is achieved using the trapezoidal method.

In the remainder of the manuscript, time-averaging over a time interval T is denoted as $< . >_T$.

3.3 Model improvements and verification

This section deals with the model verification and the steps to improve the performance. Before going into detail about the results, we provide a quick background to give the reader some context before we dive into the issues discovered and the solutions found.

The starting point is the Kranenborg et al. (2022) model. However, when analysing the model results we quickly noticed that air bubbles would stick to the bed. These bubbles led to underpredicted friction and sediment transport, particularly in the uprush. Section 3.3.1 explains this issue in more detail, looks at the origin of this and proposes a temporary solution, here called the bubble modification.

A second issue found was that the prediction of suspended sediment concentrations was insufficient. More specifically, very little sediment was brought into suspension in the lower swash during uprush. Furthermore, when a suspension event happened it was very localised and short-lived. One important parameter contributing to the capacity of the flow to carry sediment is the eddy viscosity ν_t. For this reason, the influence of the Wilcox (2006) limiter in the turbulence model was analysed. The results of this analysis is written in Section 3.3.3.

These two modifications lead to four different model setups, as detailed in Table 3.1. The effect of the different configurations on sediment transport is shown in

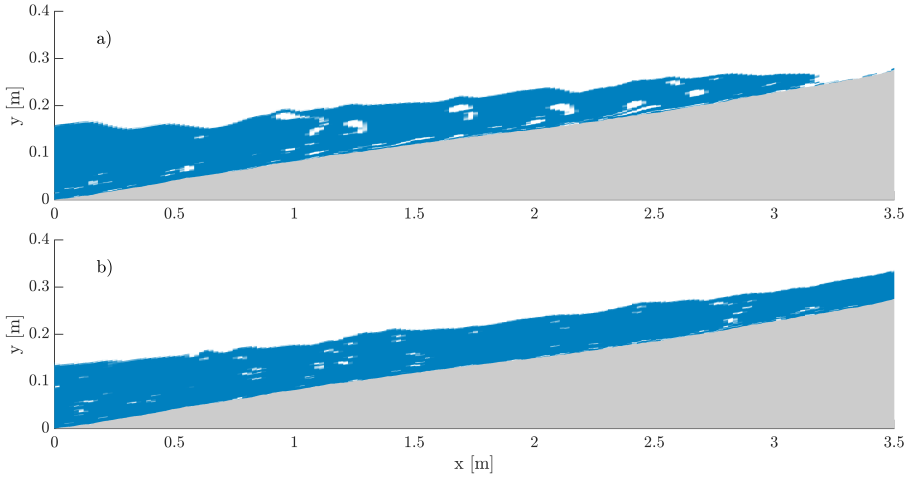

Figure 3.2
Figure showing the volume fraction field α between $x = 1\,\mathrm{m}$ and $x = 3.5\,\mathrm{m}$ at $t = 167.4\,\mathrm{s}$ (a) near the swash tip during uprush and at $t = 169.3\,\mathrm{s}$ (b) roughly two seconds after the swash tip has passed, exemplifying the issue with air content near the bed.

section 3.3.4. Finally, the verification of the best model configuration is detailed in Section 3.3.5.

3.3.1 2DV Bubble effects

The model does not describe the air/water interface directly, instead it uses a VoF approach for bookkeeping whether individual cells contain water or air. This enables the modelling of more complex surface interface shapes that, for instance, a model based on the shallow water equations cannot capture. One result of this is that bubbles can be formed. In our case, this leads to the model trapping air below the swash. Figure 3.2 shows what happens both at the swash tip and the same location roughly two seconds later. As the swash moves up the beach, sometimes small pockets of air get trapped below the swash flow. An explanation for the bubble trapping is detailed in Appendix 3.A.

Figure 3.3 shows the modelled density at the bed ρ, friction velocity u_*, surface elevation η and Shields parameter θ in time and space. The fricton velocity is related to the shear stress as

$$u_* = \frac{\tau_b}{|\tau_b|}\sqrt{\frac{|\tau_b|}{\rho}}. \tag{3.20}$$

Note that the friction velocity incorporates the direction of the shear stress, whereas the Shields parameter does not. During uprush, easily identified by the positive i.e. onshore friction velocity, the bed density shows very patchy behaviour with regions where the density is low, for instance at $x = 4\,\mathrm{m}, t = 165\,\mathrm{s}$ (here low means

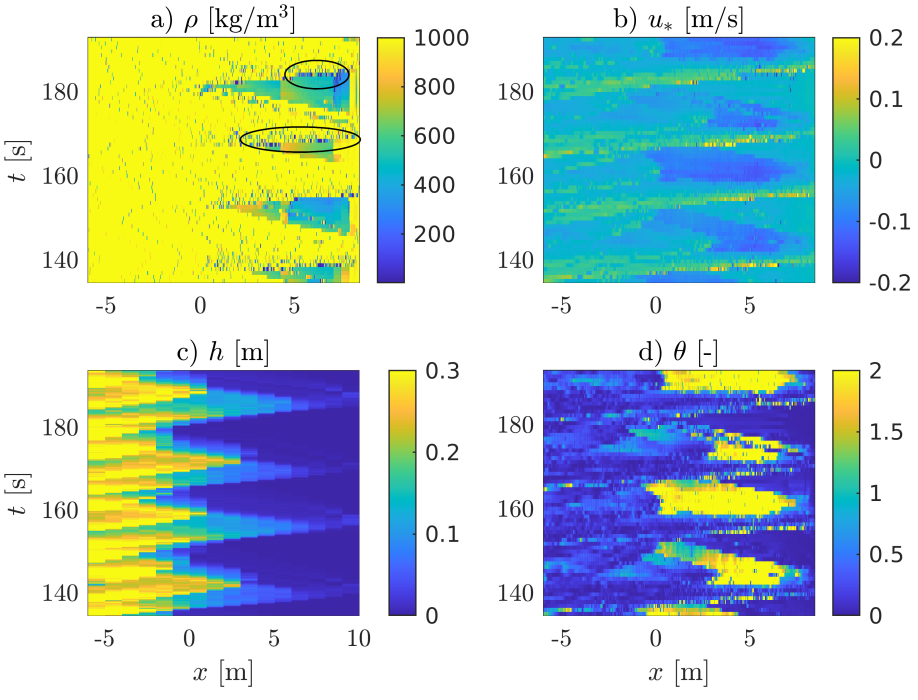

Figure 3.3
Time series of the spatial variation in (a) density at the bed, (b) friction velocity u_*, (c) water depth h and (d) Shields parameter θ from a simulation using with no bubble or turbulence modifications (Configuration A, Table 3.1). The circles in panel (a) show examples or regions where the density is low due to the presence of air at the bed below the uprush flow.

close to air density: $\rho \approx 1\,\mathrm{kg/m^3}$). In terms of the Shields parameter, the uprush also shows patchy behaviour and higher values only very localized. This is in stark contrast with the behaviour during the backwash, which displays a large patch in space and time with high Shields values.

3.3.2 Modification to remove bubbles

To investigate the impact of these bubbles, a modification to the model is introduced. This modification aims to remove bubbles that are considered unphysical. This is the case when two criteria are met simultaneously, namely that bubbles are within a distance d_b from the bed, and that the total pressure at that location is higher than P_b. This last criterion can be thought of as a distance to the free surface, where the pressure is roughly 0 Pa. Combining these criteria means that we remove bubbles that are close enough to the bed but far enough from the free surface. In other words, bubbles may be present around wave-breaking, bores or at the swash tip, but if they linger at the bed they will be removed.

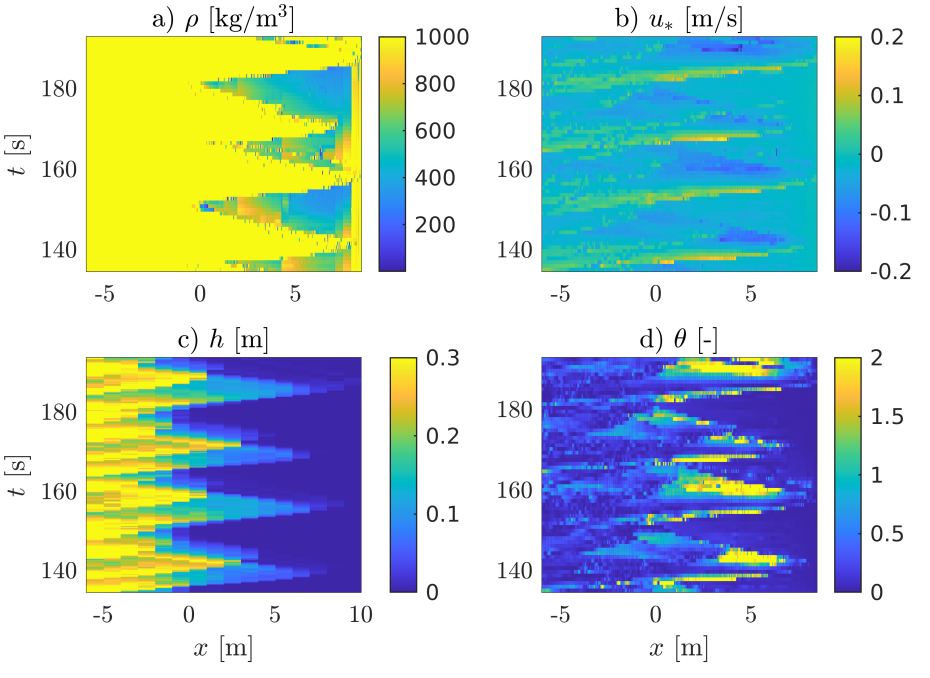

Figure 3.4
Time series of the spatial variation in (a) density at the bed, (b) friction velocity u_*, (c) water depth h and (d) Shields parameter θ from a simulation using Configuration B (Table 3.1).

The procedure to remove bubbles is straightforward. For every cell in the model that meets the criteria mentioned above, the value of α is checked. This value is then set to $\alpha = 1$, meaning the cell is forced to contain water. This means that the modification works by adding water to the model. In Section 3.5.1 the impact of this method, and other potential methods of dealing with bubbles in 2DV models are discussed.

The modification is applied in configurations B and D using the criteria $d_b = 0.05\,\text{m}$ and $P_b = 500\,\text{N/m}^2$, which corresponds to a surface elevation of roughly 5 cm. Figure 3.4 shows the results using this model (configuration B). The results are very different from the results presented where the bubbles were not removed (compare with Figure 3.3). In this case, the density is almost always close to $\rho = 1000\,\text{kg/m}^3$ underneath the submerged parts of the beach. Furthermore, the friction velocity and Shields parameter now do not display the patchiness during the uprush. Furthermore, the magnitude of the shear stress seems to have increased during uprush, and decreased during the backwash. The effect on sediment transport will be shown in Section 3.3.4.

3.3.3 Turbulence effects

To analyse the quality of sediment predictions by the model we compare them to the measurements of the OBS probes. Figure 3.5 shows the time series of the modelled sediment concentrations for all four configurations. It shows that for Configuration A, the concentrations do not correspond at all with the time series of the measured concentrations. Especially at the upper two locations, the model underestimates the magnitude of the sediment concentration during uprush (see especially panels (b-e) at $t = 137\,\mathrm{s}$ and $t = 153\,\mathrm{s}$). Furthermore, especially at locations (b) and (c), the model predicts high concentrations at the end of the backwash around $t = 163\,\mathrm{s}$.

As turbulence is an important factor in both the pick up of sediment and the ability for the flow to hold sediment in suspension, it is natural to look at how modifications to the turbulence modelling can influence the results. Larsen and Fuhrman (2018, Figure 6) show that the limiter of Wilcox (2006) has a large impact on the eddy viscosity from the point of wave-breaking for spilling breakers (Ting and Kirby, 1994). Specifically, with the limiter turned off, i.e. $\lambda_1 = 0$, the eddy viscosity was notably higher after the waves had broken. This corresponds to the original $k - \omega$ model of Wilcox (1988). However, when this turbulence model was implemented, the model became unstable when, during the process of wave-breaking, the overturning wave shape was about to touch the water surface below. Here, a layer of air was trapped between the two approaching water surfaces. In this thin air layer, the turbulent kinetic energy, and thus the eddy viscosity, rapidly increased. This destabilised the solution, leading to unphysically high flow velocities, eddy viscosities, pressures and eventually a model crash. To mitigate this, a small adaptation was applied to the turbulence model, where the turbulence production term $2\nu_t S_{ij} S_{ij}$ in Equation (3.2) was deactivated in the air phase, by multiplying it with α.

The impact of the limiter can be seen in Figure 3.6, where the instantaneous spatial distribution of the cross-shore velocity u_x, the suspended sediment concentration c and the turbulent kinetic energy k are shown during an uprush. Here the model with the Wilcox (2006) limiter , i.e. where $\lambda_1 = 0.875$, displays considerably lower turbulence levels (panels (e) and (f)). This is also seen in the sediment concentration field, which shows higher suspension levels at the swash tip when the limiter is deactivated (see panels (c) and (d), between $x = -2\,\mathrm{m}$ and $x = 0\,\mathrm{m}$).

3.3.4 Effect on sediment transport

Figures 3.5 and 3.6 shows that there are large differences in the modelled sediment concentration behaviour between the model configurations. Comparing configurations A and B suggests that the extra friction due to removed bubbles somewhat diminishes the sediment concentrations in the backwash (see panel (b) and (c) of Figure 3.5 at around $t = 162\,\mathrm{s}$). However, the concentrations are still generally too low and display the wrong timing. Compare this to the models where $\lambda_1 = 0$, i.e. models C and D, which generally produce the highest sediment concentrations,

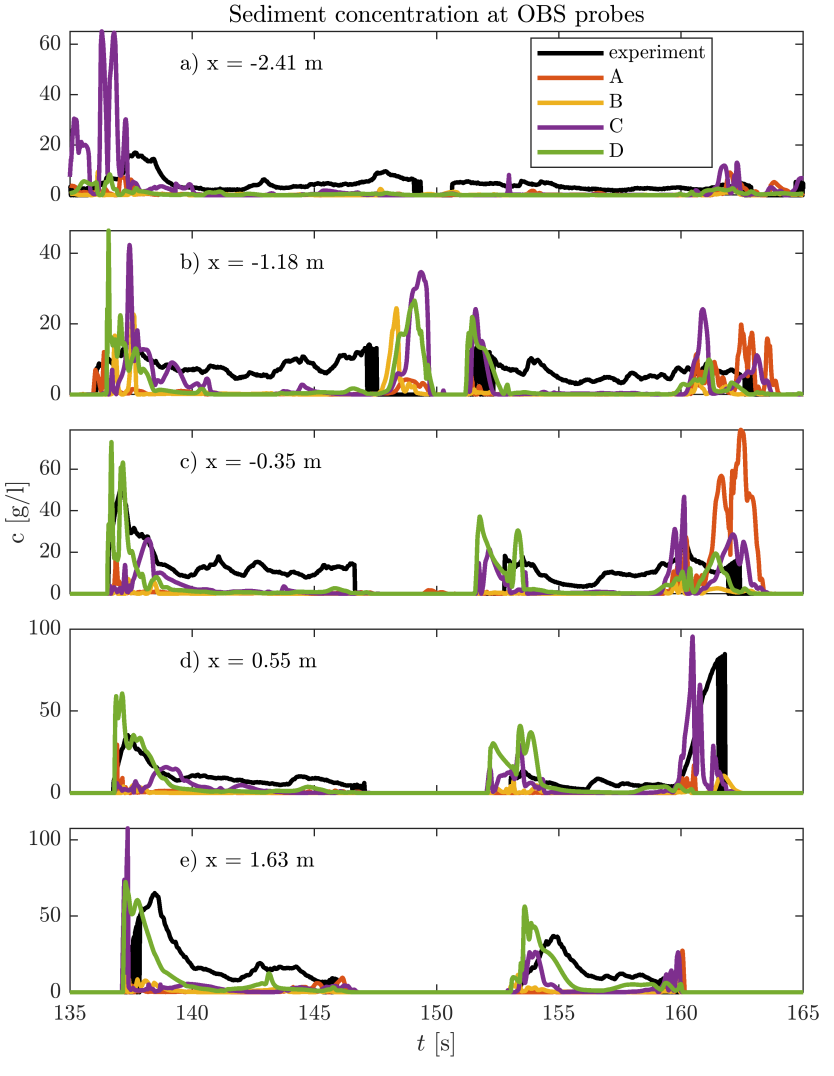

Figure 3.5
Comparison of suspended sediment concentration at the location of the OBS probes, 3 cm above the bed, for the four different model configurations. Here the measured concentrations are only shown for times when the water depth is larger than 5 cm. This figure shows two swash events.

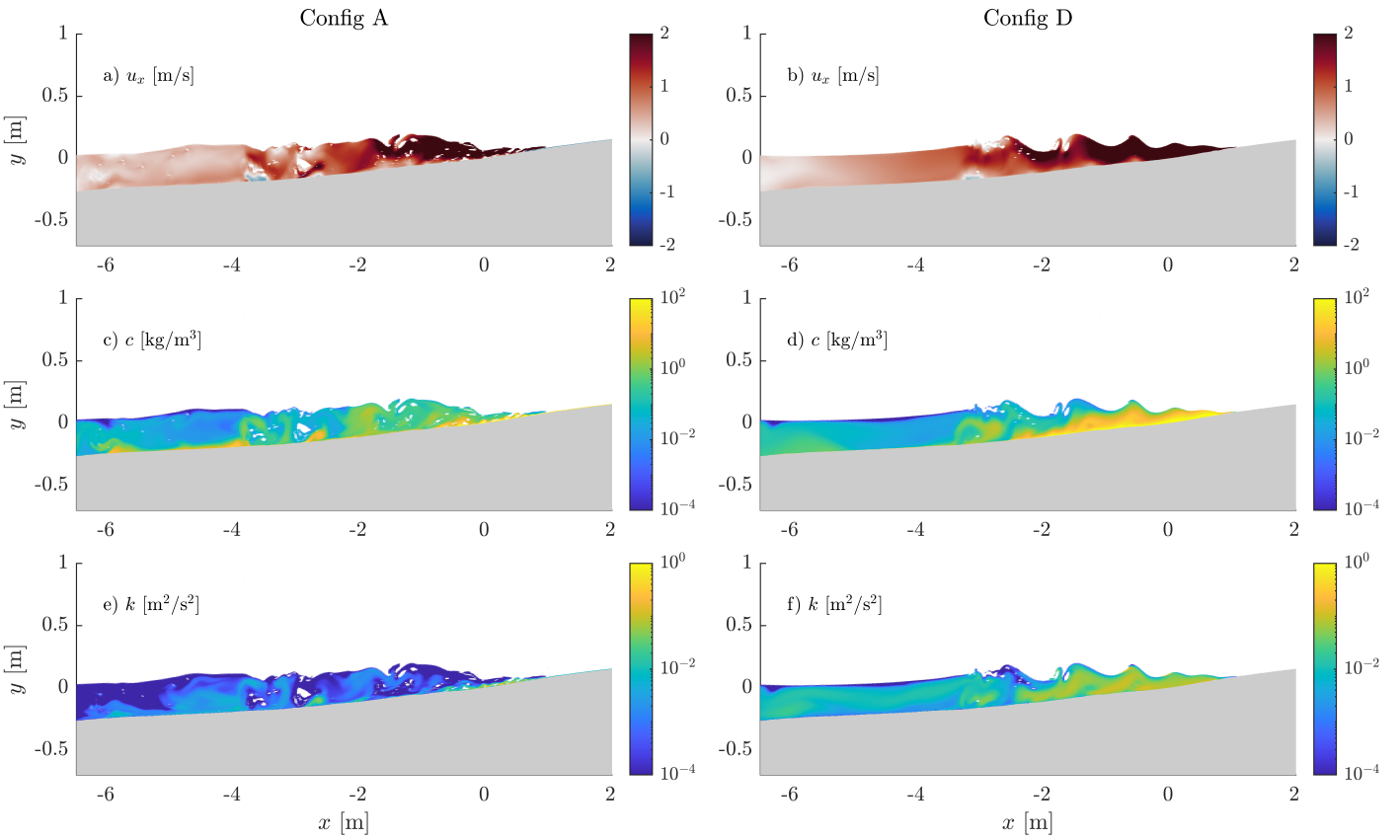

Figure 3.6
Figure showing (a,b) cross-shore flow velocities, (c,d) suspended sediment concentrations c and (e,f) turbulent kinetic energy density k for two different models during the uprush at $t = 137$ s.

except for panel (c) where the original model predicted very high concentrations in the backwash. The addition of the Wilcox (2006) limiter seems to decrease uprush transport and increase backwash transport. This can be explained by a change in bed friction, where the Wilcox (2006) limiter decreases turbulence by the breaking waves, which leads to less friction during the uprush. In turn, this means more energy is conserved making the backwash stronger.

Figure 3.7 shows time-averaged flow velocities and cross-shore sediment fluxes for all model configurations. The hydrodynamics are qualitatively very similar, displaying only minor differences, for instance around the point of wave-breaking (see Appendix 3.B for a comparison of wave gauges and flow velocities between Configurations A and D). However, there are apparent differences in the averaged suspended sediment flux. Most clearly, the direction of transport in the swash has changed from offshore for configuration A to more onshore, especially for configurations B and D. This is explained by the relative increase of friction, as in the situation where bubbles are present, the flow experiences less friction. Furthermore, the bubbles present in Configurations A and C inhibit the pickup of sediment. This makes the suspended sediment transport in Configurations B and D comparatively much stronger in the uprush. At the same time, the extra friction during the uprush means that the swash has lost energy, which explains the weaker backwash. The combination of these effects mean that, where the model configuration A predicts offshore transport in the swash, model configuration B predicts onshore transport. In other parts of the domain the differences are smaller, which is expected as the impact of bubbles was already small outside of the swash zone. A similar argument can be made for configuration C and D. The Wilcox (2006) limiter leads to decreased levels of turbulence. Therefore, in configurations C and D, turbulence levels are higher and in turn friction is higher, leading to increased sediment transport. Configuration D combines both effects that increase friction during the uprush, which explains why this leads to the most onshore sediment transport.

To confirm the visual inspection, Table 3.2 shows normalized Root Mean Square Errors (nRMSE) for all configurations at the five different OBS locations. Configuration D overall scores the best, having the lowest nRMSE at three locations. Only at locations 1 and 4 do other configurations perform better. Looking at Figure 3.5, the relatively good performance of configuration 3 at location 4 can be explained by the backwash peak around $t = 160\,\mathrm{s}$. This backwash peak is dominant in the data. For the first location, panel a), all configurations underpredict the concentration in a similar fashion, except Configuration C, and as such the difference in performance of configurations A, B and D is small.

From the results discussed above we conclude that model configuration D results in the best modelled sediment behaviour. This is the model configuration that will be used for the remaining analysis in this paper.

Table 3.2
nRMSE values of sediment concentration time-series of the five configurations compared with the measurements. The nRMSE is calculated for $T \in [135, 135 + 3T_r]$, i.e. three group repetitions, and is only calculated for points in time where measurement data exists. Here the columns correspond to the five locations and panels in Figure 3.5, and the rows correspond to the four model configurations.

	1, a)	2, b)	3, c)	4, d)	5, e)
A	0.172	0.269	0.301	0.185	0.332
B	0.162	0.249	0.248	0.143	0.223
C	0.213	0.245	0.237	0.132	0.218
D	0.167	0.221	0.222	0.150	0.208

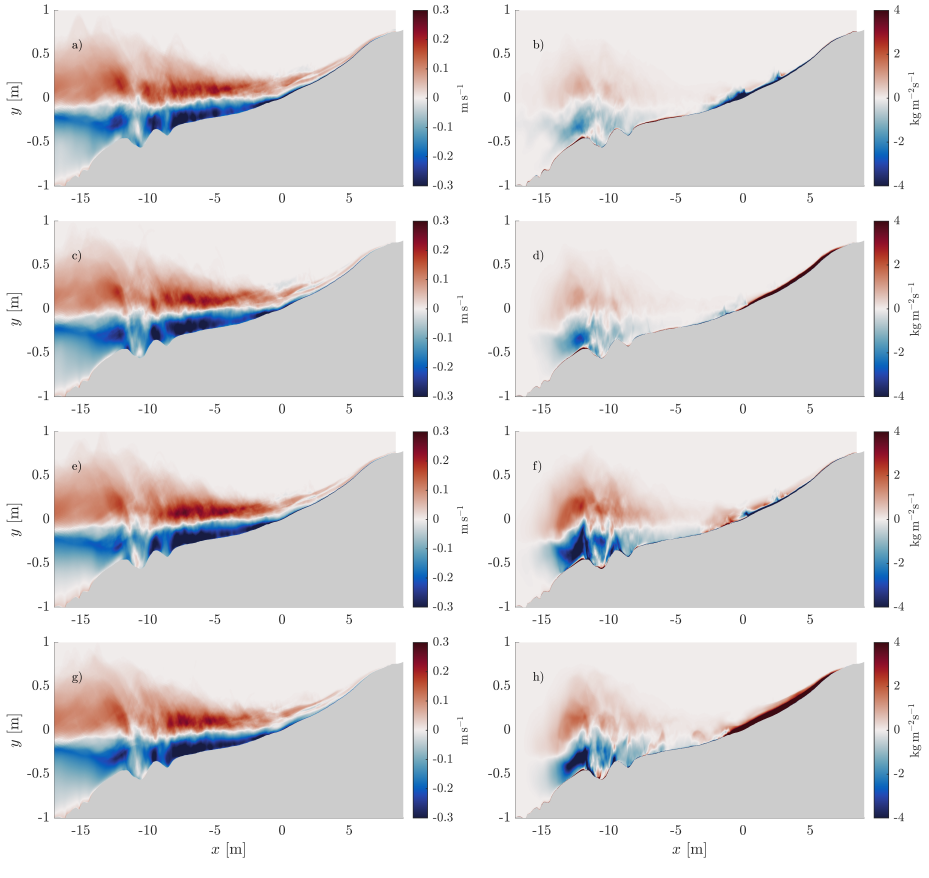

Figure 3.7
Figure showing the time-averaged cross-shore velocity (a,c,e,g) and time-averaged cross-shore suspended sediment flux (b,d,f,h) in a region of the domain $\mathcal{D}$ for three wave repetition periods starting at $t = 120\,\mathrm{s}$. Panels (a,b) show the results using model configuration A, (c,d) show configuration B, (e,f) show configuration C and (g,h) show configuration D.

Table 3.3
nRMSE values of modelled deviations from the initial water depths (η) at eight different cross-shore locations. The nRMSE values are calculated for $T \in [135\,\text{s}, 135 + 3T_r\,\text{s}]$, i.e. three group repetitions, and is normalized by the maximum measured value.

x [m]	-45.67	-21.28	-13.99	-6.3	-4.17	-1.25	0.52	2.77
nRMSE	0.155	0.094	0.143	0.207	0.211	0210	0.127	0.129

3.3.5 Final model verification

It remains to show the hydrodynamic performance of the model. As determined in Section 3.3.4, model configuration D overall reproduces the suspended sediment dynamics the best. Therefore, the hydrodynamic verification will only be presented for that model.

Figure 3.8 shows a comparison of the surface elevation time series. These are complemented with nRSME values in Table 3.3. At the three most offshore locations, the waves have not broken yet. Here, the model predicts the surface elevations very well, capturing the amplitude and shape of the waves. The largest discrepancies happen in between the wave groups where the group envelope is small. These discrepancies become smaller as the waves transform when they travel further in the flume. At the last probe location before wave breaking ($x = -13.99\,\text{m}$), the modelled waves still correspond well to the measurements. Between this probe and the next probe at $x = -6.3\,\text{m}$, the waves break. This is evident in the signal at this next probe, which is very spiky for both the measured and the modelled signals. The next two probes (at $x = -4.17\,\text{m}$ and $x = -1.25\,\text{m}$) show the surface elevation in the surf zone, offshore of the initial water line. Here intermittent effects from wave-breaking and possibly air bubbles lead to some differences in the details between the measured and modelled signals. However, the overall behaviour is well reproduced, with the two alternating wave groups showing distinct behaviour. The upper two probes (at $x = 0.52\,\text{m}$ and $x = 2.77\,\text{m}$) show that the model has correctly transformed the two wave groups into two distinct swash events, with dry periods in between. However, especially at the upper most probe, the differences become larger. Also, at $x = 0.52\,\text{m}$, the probe measures negative surface elevations at the experiments, which points to local erosion happening. This will be further discussed in Section 3.5.3.

Similarly, we compare the cross-shore flow velocities in Figure 3.9, for five locations around the initial water line, and at 3 cm above the bed. nRMSE values of these time-series can be seen in Table 3.4. Again, the model predicts the measured velocities very well. The model does show somewhat higher peak velocities at $x = -1.25\,\text{m}$ and $x = -0.46\,\text{m}$, but the general behaviour is still captured well. Above the still water line, the ADV measurements become unreliable when exposed to the air. During the wet periods, the model predicts the velocities very well, capturing even minor details in the flow at for instance $t = 130\,\text{s}$.

Overall, we conclude that the model performs well hydrodynamically. We discuss this further in Section 3.5.3.

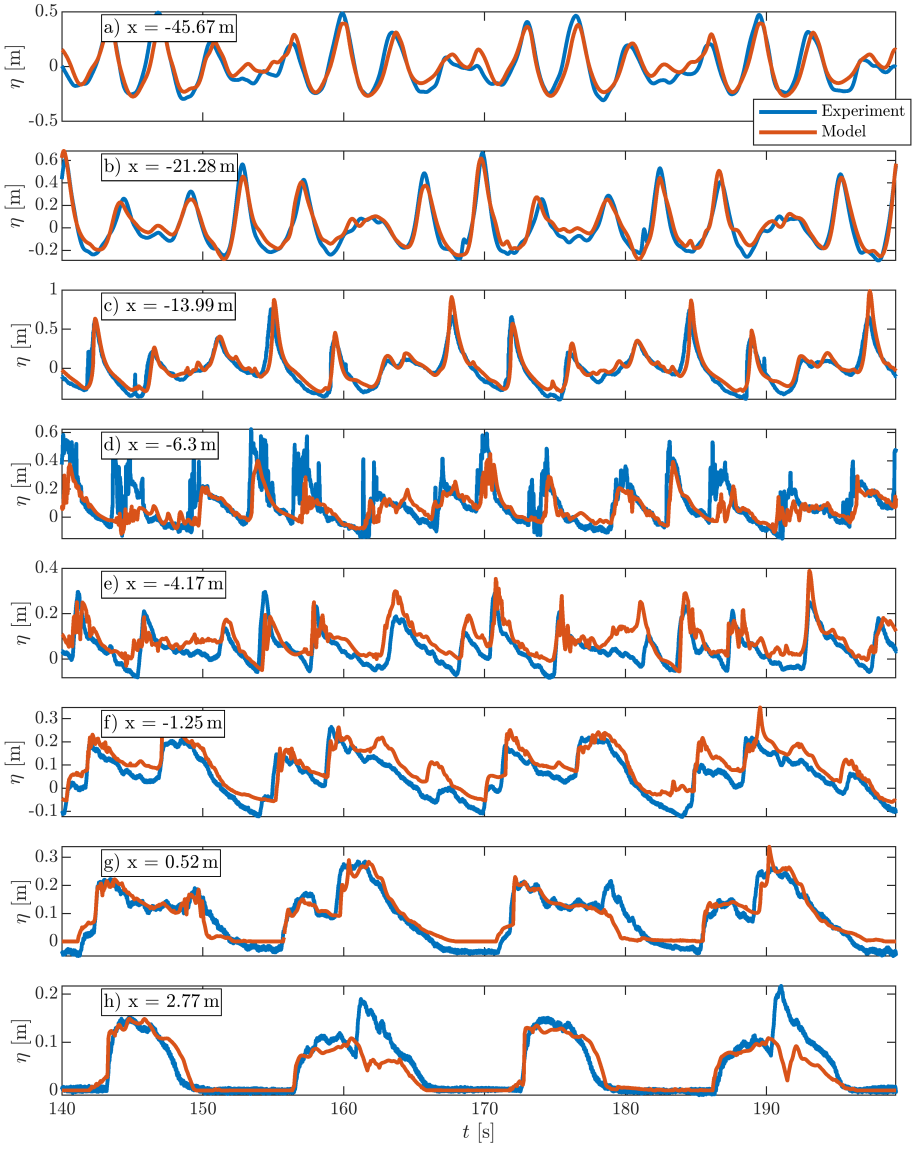

Figure 3.8
Comparison between measured and modelled surface elevations at different locations, made using model configuration D.

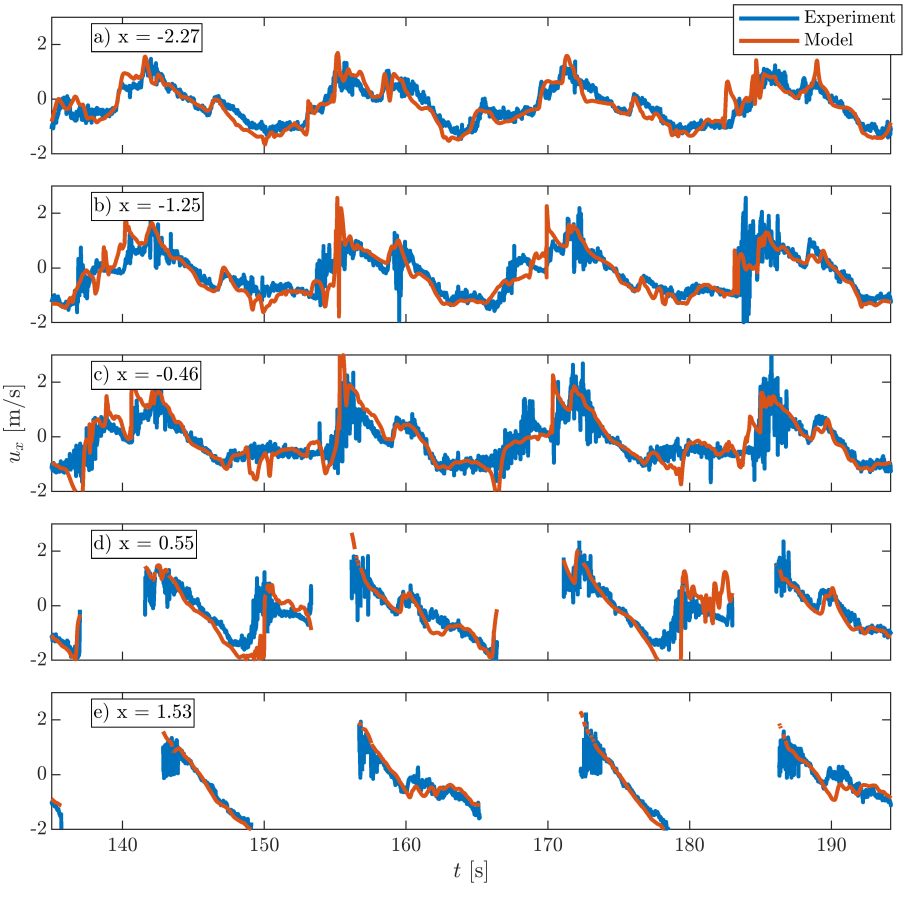

Figure 3.9
Comparison between measured and modelled velocities at 3 cm above the bed at five different cross-shore locations, made using model configuration D. In panels (d) and (e) data is omitted when the ADV probe is exposed to air.

Table 3.4
nRMSE values of modelled flow velocities 3 cm above the bed at five different cross-shore locations. The nRMSE values are calculated for $T \in [135, 135 + 3T_r]$, i.e. three group repetitions, and are normalized by the maximum measured (absolute) velocity.

x [m]	-2.27	-1.25	-0.46	0.55	1.53
nRMSE	0.536	0.357	0.369	0.465	0.537

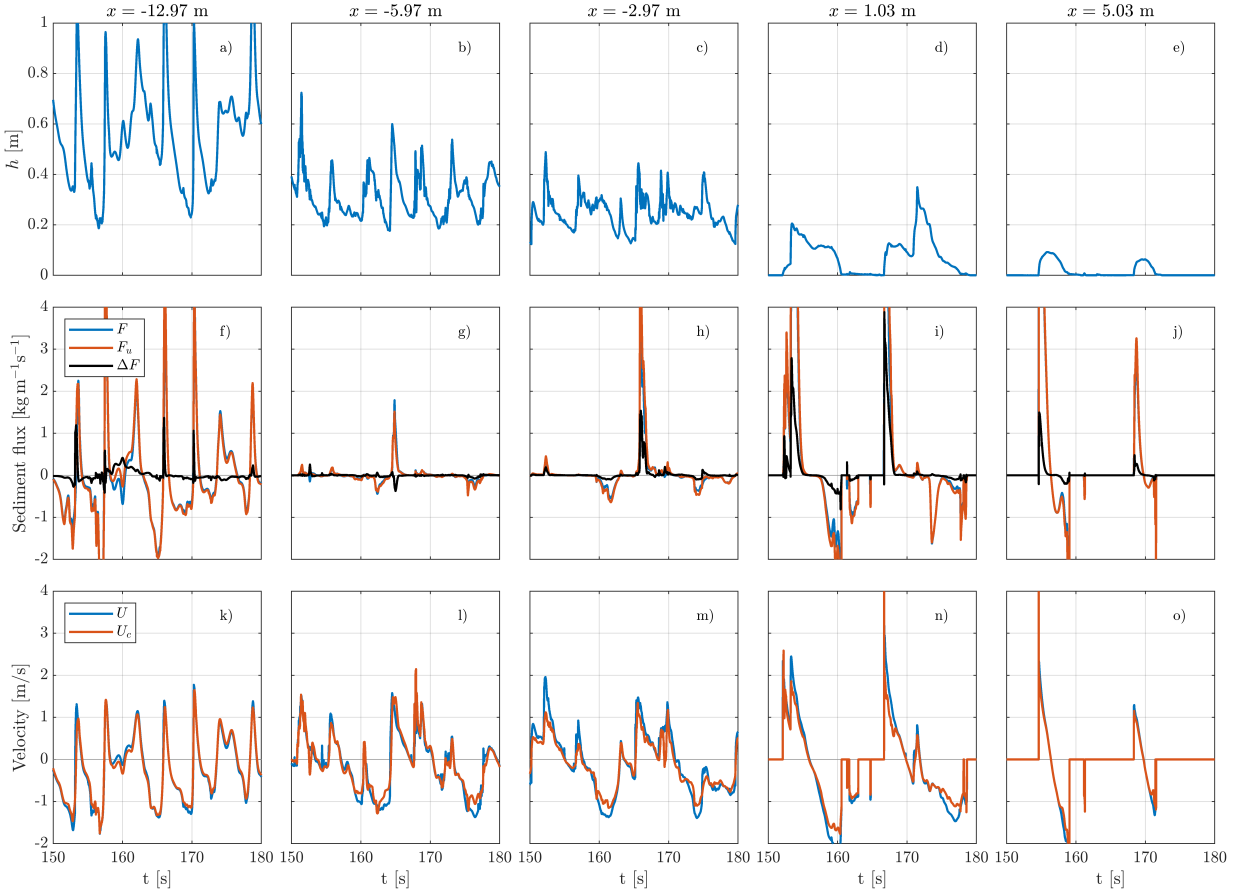

Figure 3.10
Figure showing $(a-e)$ water depth, $(f-j)$ sediment fluxes and $(k-o)$ transport velocities for five different cross-shore locations.

3.4 Transport uniformity

The results of suspended sediment transport from the previous section, e.g. Figure 3.7, show strong vertical dependence, at least when considering time-averaged suspended sediment fluxes. This section will go into more detail on the importance of these vertical dependencies.

Figure 3.10 shows time series of the suspended sediment fluxes F and F_u, as well as cross-shore velocities U and U_c at five different cross-shore locations. Furthermore, the difference between the fluxes Δ_F is shown. The most offshore location coincides with the main breaker bar. Here, compared with the other two locations offshore of the initial water line, strong sediment transport occurs, and every peak in water depth coincides with a peak in onshore-directed suspended transport. In between the peaks, sediment is transported offshore. At the two other locations below the initial water line, only one prominent peak in the fluxes is visible, showing a momentary large onshore-directed sediment flux. At the two locations located onshore of the initial water line, two strong onshore-directed flux peaks that coincide with the arrival of the swash event are visible. Furthermore, the initial swash group shows a strong backwash flux, whereas the second swash group does not show as big a backwash flux.

The velocities U and U_c also show different behaviour at the different locations. At the most offshore location, both velocities U and U_c match well. This is an indication that the vertical sediment and velocity distribution is close to uniform, or at least that for the purpose of modelling the vertical distribution is not very important. Looking at the two other locations offshore of the initial water line, the lines generally coincide well but do differ at some points in time. For instance, during the local maxima in offshore transport, $|U_c| < |U|$, indicating that the uniform flux F_u overestimates the effective advection velocity. For the uprush, there is a moment at $x = -2.97\,\mathrm{m}$, roughly at $t = 152\,\mathrm{s}$ where U_c is roughly half of U, indicating again that the uniform approximation would overestimate sediment transport. At the two most onshore locations, the same characteristics are seen, although the difference is relatively small for the most onshore location.

We can also look at how time averages of the fluxes F, F_u and the difference Δ_F vary spatially. The time-averaged quantities, averaged over three repetition periods (T_r), are shown in Figure 3.11. Here, the behaviour in the swash-zone stands out, showing overall large net onshore sediment fluxes. Here, the uniform approximation F_u leads to an overestimation of the onshore sediment flux. Another interesting observation is that when one first takes the absolute value of the difference Δ_F, the largest difference actually occurs at the position of wave-breaking, and not in the swash-zone as one might expect. This can be explained by looking at the instantaneous fluxes in Figure 3.10, where at the point of wave-breaking Δ_F displays both a positive and negative error in time. Contrast this with the two upper locations, where Δ_F is mostly positive. In short, although the differences are bigger at the point of wave-breaking, the net difference is substantially larger in the swash zone. In terms of uniformity in depth, again this points to that vertical nonuniformities are indeed important for determining the suspended sediment flux

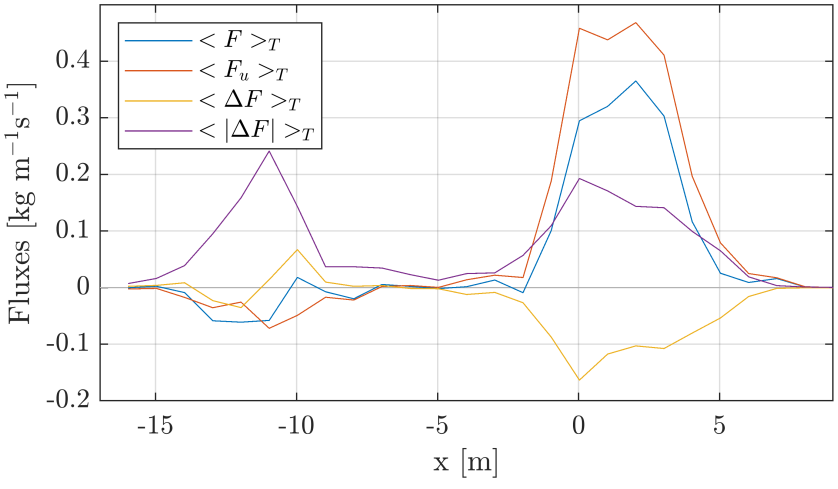

Figure 3.11
Figure showing the time-averaged fluxes F, F_u and Δ_F. Here the interval $T = [135, 135 + 3T_r]$.

in the swash zone.

3.5 Discussion

3.5.1 Dealing with bubbles

Previous research has shown that certain coastal processes are inherently 3D. For instance, there are large-scale 3D structures present around the process of wave-breaking (Dalrymple and Rogers, 2006; Tazaki et al., 2022). Furthermore, small-scale turbulence presents 3D characteristics. Complementing these, Appendix 3.A shows that also bubble break-up and rise is a 3D process that needs to be carefully considered when one models the presence of bubbles in a 2D setting.

There are many different ways one can deal with this issue. One way is accepting that a 3D model is required for the problem. This is of course in many applications not feasible. In this thesis we chose to define restrictions on where bubbles are allowed, and remove them when they are deemed unphysical. This means bubbles are removed, but a penalty to the conservation of water mass is paid. Also, the choice of criteria is not immediately clear and can therefore lead to additional model uncertainty.

To quantify the effects of the added water, a comparison is made with the total volume of water in the domain between configurations A and B. Figure 3.12 shows the evolution of the total volume in these configurations over time and the difference in volume between both configurations. The maximum difference is approximately $0.3\,\mathrm{m}^2$, which amounts to less than half a percent of the total volume. This has the

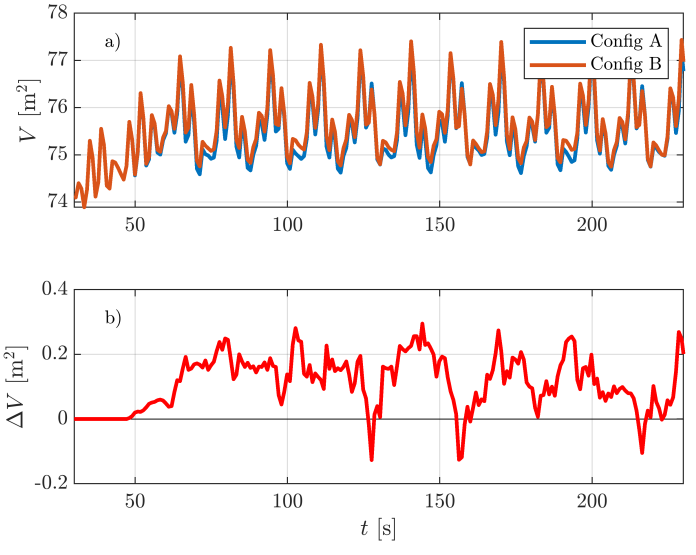

Figure 3.12
Time series of the total volume of water in the domain for Configurations A and B (panel a) and the difference between these Configurations (panel b).

effect of locally raising the water levels in the swash (see Figure 3.14 in Appendix 3.B). This can be explained by a combination of the added water mass to the domain and the increased friction in the swash for Configurations B and D leading to an increased wave setup. This also explains why the difference between the surface elevations is smaller the closer one gets to the paddle. Furthermore, the relaxation zone used to generate the waves keeps the average water level steady, meaning that the added water can leave the domain.

Alternative methods

Another way of dealing with this is to remove the air phase from the VoF implementation. This is the approach used by García-Maribona et al. (2021, 2022), which also explains the lack of air under broken bores in their results. This was until recently not available in OpenFOAM, however, a novel study has implemented such a model in the OpenFOAM environment (Qwist and Christensen, 2023). In these methods, air is not conserved which could lead to different flow behaviour where air content is important, such as breaking waves and bores. The importance of modelling air conservation is, to the knowledge of the authors, not yet understood, and is something that requires more investigation.

In our study we used the VoF method and specifically the isoAdvector implementation. There are also alternatives for determining the free surface, such as for instance the level set method. However, when this method is used, the bubbles

dissapear because these methods strictly do not conserve mass. Recent studies have introduced ways to correct this by coupling the level set method with the VoF method (Kim and Park, 2021; Xia and Kamlah, 2022). However, this means that, in effect, we are back to the situation with 2D bubbles, which we have shown show unphysical bubble rise behaviour. Alternatively, a different VoF method, such as the default MULES (Ubbink, 1997; Rusche, 2002) method can be used. This method produces smoother interfaces compared with isoAdvector and as such could pose a solution to the small bubbles. However, as detailed in Roenby et al. (2016), isoAdvector was designed precisely to generate sharp interfaces between fluids, which is physically more accurate.

Finally, one can model bubbles in a similar manner this study approaches suspended sediment, by viewing dispersed bubbles as a continuous field with a concentration, which is modelled according to a conservation law. This has previously been successfully done for breaking waves (e.g. Shi et al., 2010; Derakhti and Kirby, 2014; Castro et al., 2016), however to the authors' knowledge this has not yet been applied to simulations involving sediment transport or in the swash zone.

For modellers, the most important take-away from this discussion is that it matters how one deals with bubbles. Depending on the application, some methods are more suitable than others. For instance, 3D simulations are in many situations not suitable. For coastal applications, it could be fruitful to study the importance of air-conservation under breaking waves and bores, as methods that do not require computations in the air phase are computationally more efficient. Furthermore, the method of modelling bubbles as a dispersed phase could be a promising, physics-based approach. An analysis of these methods and their impact on sediment transport would be a valuable endeavour.

3.5.2 Turbulence

It is widely accepted that bore-related turbulence is an essential driver for sediment transport in the swash zone (e.g. Butt et al., 2004; Alsina et al., 2009; Zhu and Dodd, 2020). This is again affirmed in the present study, which shows that the limiter for the $k-\omega$ model, introduced by Wilcox (2006) in this situation leads to underpredicted sediment concentrations, and as such can be presumed to underpredict turbulent kinetic energies as well. This limiter was introduced to better capture flow separation phenomena in compressible flows in the presence of a shock (Coakley, 1983). This is a different application than water waves, which are usually modelled as incompressible and as such no shocks occur. Our results suggest that the limiter can lead to underpredicted sediment concentrations in the uprush. To definitively conclude this though, this should be investigated for more cases.

There are various studies on the suitability of RANS turbulence closures and modifications to them. For instance the study by Brown et al. (2016) analysed turbulence closures under plunging and spilling breakers. Furthermore, Devolder et al. (2018) analysed a buoyancy production modification specifically for free-

surface waves and the aforementioned Larsen and Fuhrman (2018) limiter addresses the overproduction issue many two-equation RANS turbulence closures posses. Recently, a stress-ω model by Li et al. (2022) showed that their model both improved velocity profiles in the surf zone, and resulted in larger Reynolds shear stresses in the inner surf zone.

These are important and promising results for sediment transport. However, it is not always straightforward to investigate their impact in the swash zone. Even though the goal of the present paper was not to investigate turbulence models in depth, we tried applying different flavours of turbulence models such as the Launder and Sharma (1974) $k-\epsilon$ model as implemented in Larsen and Fuhrman (2018), but also the nonlinear $k-\epsilon$ model (Shih et al., 1996) which Brown et al. (2016) ranked the best among their studies. However, these models led to unphysically large eddy viscosities and velocities, which ultimately led to unstable simulations. This makes the study of turbulence models in the swash zone, and their verification for sediment transport, very difficult to do.

3.5.3 Model performance

The comparison of the modelled hydrodynamics with the wave gauges and ADVs show that the model performs well. The performance is similar to the model study of Larsen et al. (2020), who also used a RANS and VoF model based on OpenFOAM for studying turbulence under plunging bichromatic waves, and the study of Losada et al. (2008) who used the COBRAS model. Both models show small discrepancies at the crest of the wave group envelope, and larger differences at the trough of the wave group envelope. A comparison with measurements of modelled flow velocites shows that the model performs well in this respect as well. The quality of the simulation is similar at all five locations. The largest differences happen around quick jumps in velocity. Previous studies conducting 3D simulations have shown that the flow is inherently 3D (e.g. Dalrymple and Rogers, 2006; Tazaki et al., 2022), which the 2DV model cannot capture, and could lead to some discrepancies.

The model predicts onshore-directed suspended sediment transport. This is more than in the experiment, which for this wave condition and initial bed profile show a mild accretion high in the swash. This can also be seen in Figure 3.5, where model configuration *D* shows high sediment concentrations in the uprush but low sediment concentrations in the backwash, especially at the two most onshore locations. During uprush these concentrations correspond well with the measurements, but later towards the backwash the model predicts significantly lower concentrations than the measurements. Because of this, one can assume that the model performs reasonably well in the uprush, but has more difficulty in the backwash. Given the observations of Alsina et al. (2009) and Zhu and Dodd (2020), this suggests that the model accurately captures the suspended transport due to wave-breaking related turbulence and sediment advection, which is more important in the uprush, but understimates the shear-related transport in the backwash. However, the different results from the four different configurations show that this balance is delicate and can be difficult to achieve. Currently, Configurations B

and D remove all bubbles that remain close to the bed, whereas in reality some bubbles will still be present there. This suggests that the bubble-removal in these configurations perhaps is too aggressive. However, all four configurations generally show underpredicted sediment concentrations between the onset of uprush and the end of the backwash, meaning that for all configurations sediment is not kept or brought into suspension enough at these moments. As this is the case in all four configurations, the bubble removal procedure cannot be the cause of this. Instead, turbulent mixing is the most important process in the model for keeping sediment in suspension, this could mean that turbulence is underpredicted at these moments. However, it is important to note that this is a comparison with point measurements, and that OBS probes can be sensitive to other impurities in the water such as air bubbles.

Finally, we note that the model is run for a situation where the experiments are almost at their (pseudo)-equilibrium, or at the very least show little morphological development compared with the start of the measurements. Due to minor differences between the model and the experiments, such as the different shapes of the paddles, 3D flow effects around the point of wave-breaking and nonuniformities in the alongshore direction, the model could tend to a different equilibrium than the experimental conditions. Furthermore, although bedload contributes less to the overall morphodynamics for these sediment characteristics in this model (Kranenborg et al., 2022), including bedload transport and intraswash morphodynamics in this study could improve flux predictions. The influence of this is seen in the measurements of water depths, for instance panels (f,g) in Figure 3.8, where the negative water depths show that the bed level has decreased.

3.5.4 Vertical structures

The fluxes presented in Figure 3.7 show strong vertical dependence in the time-averaged water and sediment fluxes. This is similar to the time-averaged fluxes presented by García-Maribona et al. (2022), who observed different sediment fluxes near the bed compared with higher in the water column (see Figure 14 in their paper). This is also seen on top of, and offshore from the main breaker bar in panel (h) of Figure 3.7. García-Maribona et al. (2022) further point out that because of this, one can expect depth-averaged models (called 1D models in their paper) to have difficulty predicting suspended sediment fluxes.

In Section 3.4 we analysed the uniformity of the depth-dependent sediment transport flux at various locations in the surf and swash zones. An unexpected result is that, according to our results, around the point of wave-breaking, the suspended sediment flux can be thought of as being vertically uniform without a big concession in terms of sediment flux. This is different in the swash, where even though the flows are shallow, taking nonuniformities into account is clearly needed. Given that comparatively little sediment is exchanged between the surf and the swash, this is likely a local effect in the swash zone, and thus not dependent on the advection of pre-suspended sediment from the surf zone to the swash zone. This suggests that it is very important for depth-averaged models to both take this

turbulent mixing and the vertical structures into account.

The uniform flux as defined in Eq (3.13) is an interesting approach for the inclusion of vertical nonuniformities in a depth-averaged model. However, there are important differences between this analysis and an actual implementation in a depth-averaged model. Most importantly, the velocity and sediment distributions on which the uniform flux calculation is performed are still depth dependent. For this reason, the evolution of the suspended sediment by a depth-averaged model might differ more than the comparison between fluxes here suggests. A direct comparison between the fully depth-dependent flux, and a depth-averaged sediment model where the hydrodynamic input is the same could improve these findings further, and point to improvements that can lead to better depth-averaged flux calculations that can be practically implemented in depth-averaged models. Furthermore, to implement the effective velocity approach, first a suitable parametrisation needs to be formulated.

3.6 Conclusion

A 2DV, depth-resolving model, based on the model by Kranenborg et al. (2022) and Jacobsen et al. (2014) was used to analyse the suspended sediment transport under field-scale bichromatic waves. The model was applied to the experiments of Van der Zanden et al. (2019a) and was validated using measured surface elevations, flow velocities and sediment concentrations. Here, the answers to the research questions presented in the introduction are given.

How do bubbles behave in a 2DV model and what are the modelling consequences?

It was noticed that for 2DV models, bubbles can stay near the bed, leading to decreased friction during the uprush. This in turn biases the sediment transport towards the backwash, as uprush sediment transport is inhibited and backwash transport is enhanced due to the decreased uprush friction leaving the swash with more potential energy. To investigate the origin of this issue, a comparison was made between a 2DV and 3DV model of the bubble dynamics of an inverted air/water layer, see Appendix 3.A. The models showed that bubbles rise considerably faster in a 3D model compared with a 2DV model. When these parasitic bubbles were removed from the swash zone model, the increased friction during uprush and decreased friction during backwash lead to stronger onshore net transport fluxes, improving model predictions of suspended sediment concentrations.

What is the influence of the Wilcox (2006) limiter on wave-breaking turbulence and sediment transport?

A similarly important effect on sediment transport was noticed when the effect of the Wilcox (2006) limiter on sediment transport was analysed. When this limiter was deactivated, corresponding to the original Wilcox (1988) $k-\omega$ model,

turbulence and in turn eddy viscosities were increased from the region of wave-breaking and onshore. This led to increased sediment transport, especially during uprush.

The combination of both effects mentioned above was needed to achieve adequate sediment behaviour. In fact, these adaptations lead to significantly different sediment dynamics, as shown in Figure 3.7. The same figure shows very small differences in mean flow velocities. This shows that the quality of modelled flow velocities and water depths alone are not a good enough for achieving correct sediment transport results, and that small differences in turbulence model and small quantities of parasitic bubbles near the bed can have large impacts on the quality of the sediment transport predictions.

How do vertical structures in sediment concentration and flow velocity influence the sediment transport flux?

The final validated model shows that the effect of nonuniformities in the cross-shore velocity and suspended sediment concentration have a large influence on the total sediment flux in the swash. More precisely, when uniform flow velocities and sediment concentrations were assumed, net sediment transport fluxes were overpredicted. To compensate for this, depth-averaged models would require a lower effective transport velocity compared with the depth-averaged velocity in the sediment transport calculations. These findings are in contrast with the region of intense wave-breaking where, although a large amount of sediment is being transported, these vertical nonuniformities are less important to take into account in the net flux calculations.

Acknowledgements

This work is part of the research program Shaping The Beach with project number 16130, which is financed by the Netherlands Organisation for Scientific Research (NWO), with in-kind support by Deltares. The model simulations were carried out on the Dutch national e-infrastructure with the support of SURF Cooperative.

3.A 3D vs 2D bubble effects

To better understand what happens to bubbles in the model, we set up a different model experiment solely focussed on bubble dynamics when a layer of air is present under a layer of water. We look at a domain cubic domain with sides $l = 0.1\,\mathrm{m}$. The initial condition is partitioned in three vertical layers. At the bottom there is a layer of air ($\alpha = 0$) with a thickness of $h_{air} = 0.01\,\mathrm{m}$. Next is a layer of water, with a thickness of $h_{water} = 0.07\,\mathrm{m}$. Finally, at the top there is a layer of air again.

The domain is discretised in a 2D and a 3D configuration. In both models, the x and y directions are discretised in 100 equidistant layers of cells. For the 3D case, also the z direction is discretised in 100 layers. This means that the 2D model

consists of 10 000 cells, and the 3D model consists of 1 000 000 cells. In this case the boundary conditions at the walls are slip conditions, and the atmosphere condition is the same as explained in Section 3.2.2. Finally at the bottom wall a no-slip condition is imposed. To keep these cases as simple as possible, no turbulence was modelled, meaning only the fluid viscosities contributed to the momentum diffusion.

Figure 3.13 shows the results, comparing the 2D and 3D cases. Qualitatively there is a big difference between the two solutions that is immediately visible. In the 3D case, bubbles look natural and as expected have a 3D shape to them. However, this is not possible in the 2D case, meaning that the bubbles in fact represent long cylinders, as there is only one cell in the z direction. This also means that, even though in panels (g) and (h) the solution looks similar on the boundary, the amount of air in the domain is very different, as seen in panels (e) and (f). Looking even later in the simulation at $t = 2\,\mathrm{s}$, there are still significant bubbles present in the 2D simulation, see panel (i), whereas panel (j) displays no more bubbles. Note that some air is still visible in panel (l); this air is not visible in panel (j), this is solely due to the isosurface value of $\alpha = 0.5$.

The difference between the 2D and 3D bubbles simulations show that in a 2D simulation, bubbles take much more time to reach the surface. Moreover, bubbles also stay close to the bottom for longer than in the 3D simulation. The explanation for this comes from the fact that, for the 2D situation, water has only one degree of freedom in which it can flow around the bubble. In the 3D situation, bubbles are allowed to break up, and water is allowed to flow around bubbles in two degrees of freedom. This effectively means that the friction bubbles experience in the 2D situation is much larger than in the 3D situation.

3.B Comparison between Configurations A and D

Figures 3.14 and 3.15 show comparisons of wave gauges and flow velocities between model Configurations A and D. The water levels show little difference between the configurations. This is especially true the closer one gets to the paddle. At the beach end, Configuration D produces slightly larger water depths. The flow velocities similarly show little qualitative difference. The largest differences occur when either model produces a spiky signal, which indicates presence of a bore or a similar phenomenon where velocities fluctuate rapidly. The calmer signal between these events coincide well between both model Configurations.

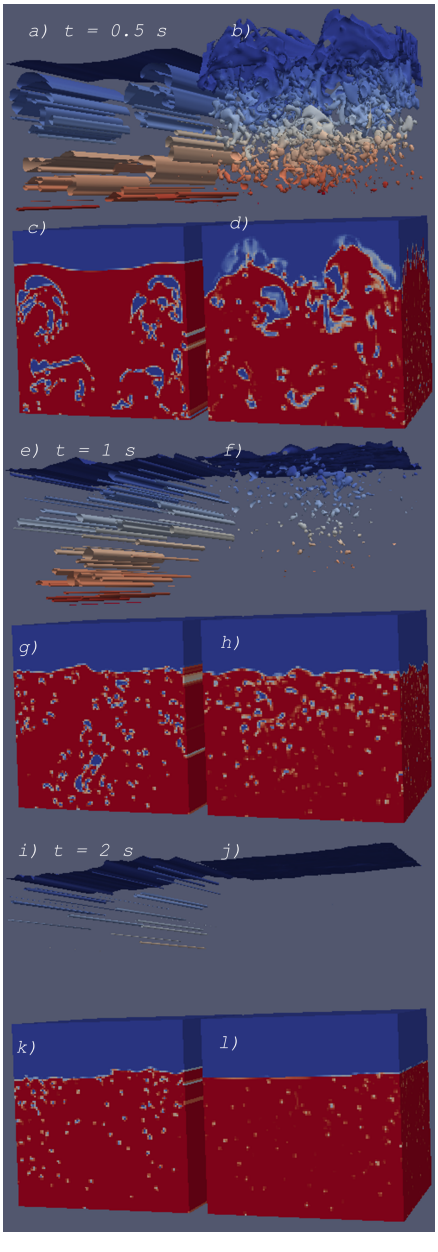

Figure 3.13
Figure showing three snapshots of the 2D and 3D models of bubbles escaping from an inverted air/water layer. Here panels (c,d,g,h,k,l) show the simulations of the α field from a side perspective. Above the blocks (panels a,b,e,f,i,j) are isosurfaces where $\alpha = 0.5$ are shown, where the colour indicates the pressure (red means relatively high pressure and blue means relatively low pressure). The left column shows the 2D results and the right column shows the 3D results. Panels (a-d) show the situation at $t = 0.5\,\mathrm{s}$, panels (e-h) show the situation at $t = 1\,\mathrm{s}$ and panels (i-l) show the situation at $t = 2\,\mathrm{s}$

.

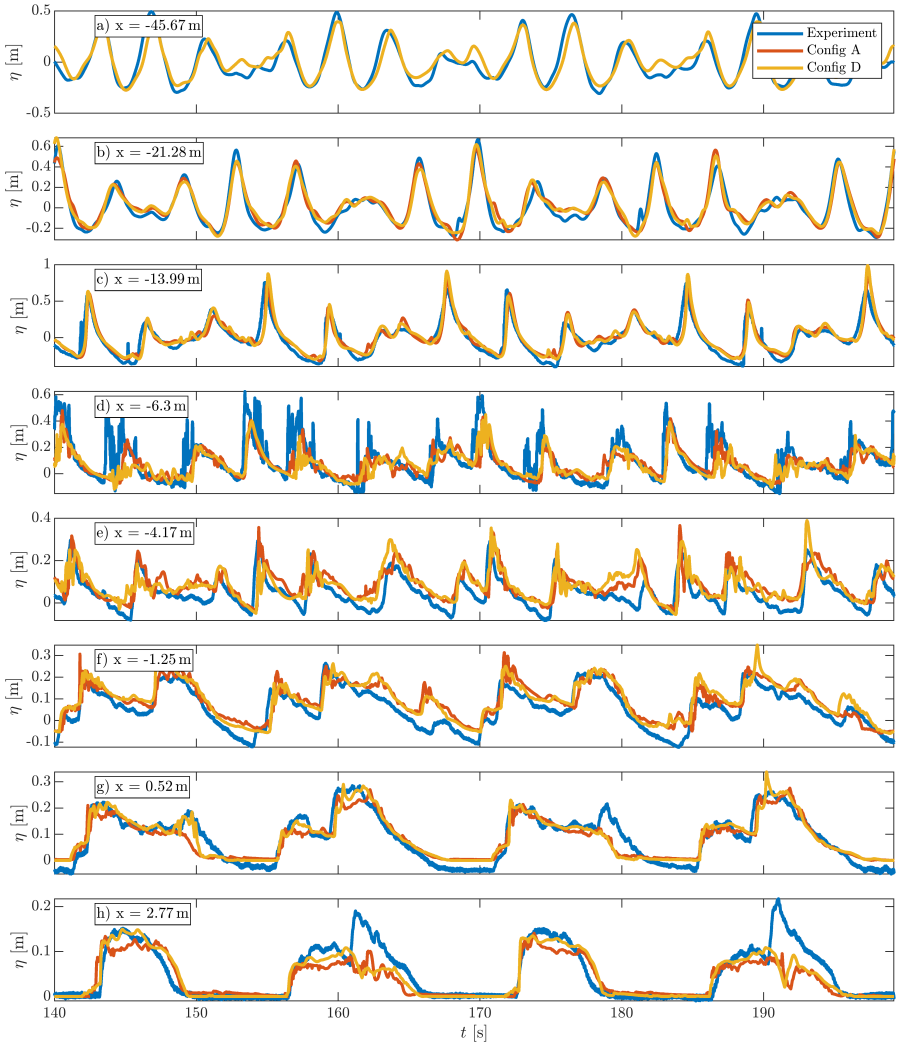

Figure 3.14
Comparison of water levels between measurements and model Configurations A and D.

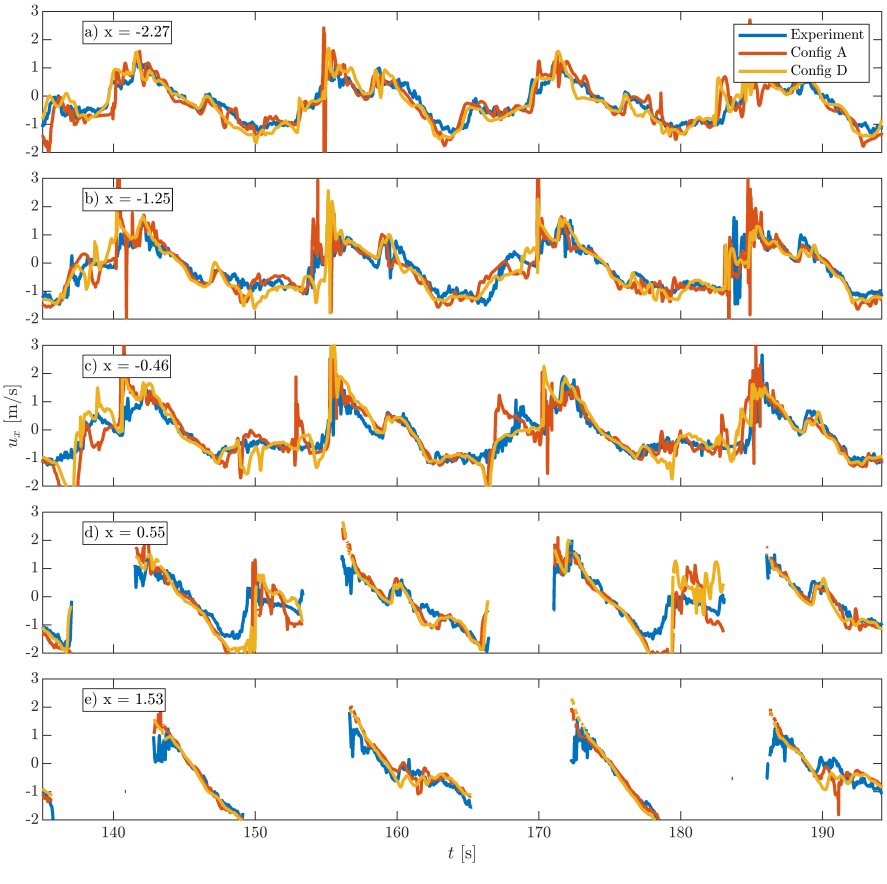

Figure 3.15
Comparison of velocities between measurements and model Configurations A and D.

Chapter 4

Measurements and modelling of pore-pressure gradients in the swash zone under large-scale laboratory bichromatic waves

This chapter has been submitted as Kranenborg, J. W. M. , Pauli, T., Jacobsen, N. G., Van der Werf, J. J., Dionisio Antonio, S., Campmans, G. H. P., Reniers, A. J. H. M., & Hulscher, S. J. M. H. ... Measurements and modelling of pore-pressure gradients in the swash zone under large-scale laboratory bichromatic waves.

Abstract

We present physical laboratory measurements of surface elevation and pore water pressures in a fine sand bed under bichromatic waves in a large-scale laboratory experiment. This was done at three cross-shore locations in the swash zone, with pressures being measured at different depths in the bed. The measurements show that the pore pressure signal decays and shifts with increased depth. These measurements are used to validate a practical model, based on the theory of Yamamoto et al. (1978) and Guest and Hay (2017). The model corresponds well with the measurements ($nRMSE < 0.2$ and $R^2 > 0.95$ for most probes) and shows that a frequency-based model can reproduce the pressures in the bed, despite the bed being exposed during dry periods. Furthermore, the model provides the opportunity to calculate pressure gradients, both throughout the bed and at the bed surface. These modelled pressure gradients at the bed surface show that the vertical pressure gradient can have an important impact on the Shields parameter, thereby influencing sediment transport.

4.1 Introduction

The swash zone is the region of the beach where waves run up and down the beach, connecting the submerged bed of the surf zone with the dry part of the beach. Here, the hydrodynamical forcing that drives sediment transport is not only controlled by what happens above the bed surface but, due to the porous nature of the sediment bed, is also influenced by interactions between the subsurface and surface flow. These interactions can manifest themselves as exchanges in mass and momentum through seepage (exfiltration and infiltration) and can ultimately influence the forcing on sediment grains, and thus affect sediment transport and morphodynamics.

For fine-grained beaches, the vertical ex-/infiltration velocities are small compared with the wave-related orbital velocities. Therefore, the effect on the overground flow is small compared with larger grains, as the small pores require larger pressure gradients to drive the flow due to the flow resistance (Masselink and Li, 2001). However, the small grains are more easily influenced by small changes in the near-bed hydrodynamics, such as for instance externally generated turbulence (Fredsøe et al., 2003). One important effect is that the seepage affects the shape of the boundary layer, which in turn influences the bed shear stress. This was studied experimentally by Conley and Inman (1994), who showed that infiltration leads to higher near-bed velocities and larger bed shear stresses (thinning of the wave boundary layer), while exfiltration had the opposite effect (thickening of the wave boundary layer). Later, Lohmann et al. (2006) investigated the role of turbulence in detail using Large Eddy Simulations. Along with similar implications for the bed shear stress as Conley and Inman (1994), they also showed that infiltration decreased turbulent flow fluctuations near the bed, whereas exfiltration increased these fluctuations. Another important effect is that local pressure gradients affects the immersed particle weight, leading to an apparent lower particle weight during exfiltration and a higher particle weight during infiltration (Baldock and Holmes, 1998; Francalanci et al., 2008). In order to arrive at an improved understanding of these contributions to the net sediment transport in the swash zone, it is important to understand how incident waves influence the pressure and pressure gradient in the top layer of the soil.

Pressure gradients in the bed result from the finite wavelength of the water waves. Their behaviour is influenced by the elasticity of the bed and the pore fluid (Biot, 1941; Yamamoto et al., 1978). This elasticity means that the pressure amplitude attenuates and the phasing shifts, strengthening with increased depth under the bed. Furthermore, at a given depth higher frequency components experience stronger attenuation and larger phase shifts than lower frequencies. This frequency-dependent attenuation and phase shifting ultimately results in gradients in the pressure field, where the strength of the attenuation and shifting is dependent on the physical properties of the bed, particularly the degree of saturation of the soil (Guest and Hay, 2017). The higher the degree of saturation, the lower the phase lag (Yamamoto et al., 1978). This degree of saturation in beaches depends on different factors, such as the depth below the surface and local

wave and tide conditions. In the swash zone, air can enter the beach during the periods when the beach is dry. Furthermore, water that infiltrates the beach is not fully saturated and carries air bubbles with every infiltration event (Heiss et al., 2014), and also biological processes within the bed can produce gas and contribute to the air content (Horn, 2002). This means that the air content of the beach, and therefore the pressure behaviour, can vary between different locations and seasons due to biological activity.

Previously, there have been measurement campaigns featuring a vertical array of pressure sensors to investigate pressure propagation in the surf and swash zones, both in the field and in laboratory environments. On natural beaches, pressure gradients have been observed in many such studies, associated with different sediment and wave characteristics (e.g. Turner and Nielsen (1997); Raubenheimer et al. (1998); Baldock et al. (2001); Pedrozo-Acuña et al. (2008); Guest and Hay (2017); Stark et al. (2022)). The measurements of Raubenheimer et al. (1998) did not show considerable phase shifting at a natural beach consisting of fine sand. However, the later studies by Pedrozo-Acuña et al. (2008) (gravel), Guest and Hay (2017), (mixed sand and gravel) and Stark et al. (2022) (medium to coarse sand) did find phase shifting in their results. Sumer et al. (2011, 2013) also measured the pressure gradients at multiple cross-shore locations for small-scale solitary and regular monochromatic waves, showing that the pressure gradients had a significant influence on the bed shear stress and sediment entrainment, also in the swash.

The recent recasting by Guest and Hay (2017) of the Yamamoto et al. (1978) model provides an elegant, one-parameter model to study the importance of phase shifting and attenuation. However, this model has not yet been used for studying pressures (and their gradients) in the swash-zone of sandy beaches. Furthermore, given the intermittent wetting and drying of the bed surface, it is unclear whether a model based on a superposition of components, each following the theory of Yamamoto et al. (1978) and Guest and Hay (2017), is valid in the swash zone at all, given that these models assume a continuously inundated and horizontal bed.

To investigate these issues, novel field-scale laboratory measurements of pore pressures at different depths were conducted, co-located with measurements of surface elevations and flow velocities. This was done for a sandy beach, similar to the Raubenheimer et al. (1998) but in a swash setting, and Sumer et al. (2011, 2013) but using larger, field-scale waves. Furthermore, since bed properties such as saturation can vary spatially, we conduct these measurements at three different cross-shore locations simultaneously. Additionally, we investigate the capability of the frequency-based analytical theory of Guest and Hay (2017) to model the pressure response at these locations, keeping in mind that the swash motion leaves the beach uncovered at times. The model can then be used to calculate pressure gradients in the top layer of the bed, which we use to investigate how vertical pressure gradients could influence the Shields number.

The paper first describes the experimental setup, analytical model and how these will be compared in Section 4.2. The results from the measurements, the model and its comparison are subsequently presented in Section 4.3. These results are then discussed in Section 4.4, after which we present the main conclusions in

Table 4.1
Location and depth of pressure sensors at the start of the measurements. Here the depth is denoted relative to the initial bed profile, in accordance with Figure 4.1.

	Location A (surf)		Location B (-)				Location C (swash)		
Sensor nr	1	2	1	2	3	4	1	2	3
Depth (m)	0.40	0.50	0.35	0.39	0.435	0.52	0.3	0.4	0.65

Section 4.5.

4.2 Methodology

4.2.1 Experiment setup

The experiments were conducted as part of the *Shaping The Beach* (Van der Werf et al., 2019) experimental campaign, at the large-scale CIEM facility of Universitat Politechnica de Catalunya in Barcelona. The flume is 100 m long, 3 m wide and 4.5 m deep and was filled with water with a depth $h_0 = 2.47\,\mathrm{m}$ at the wave paddle. The depth-coordinate z is defined positively upward from the still water line. The cross-shore coordinate x is defined positively landward from the initial shoreline position. From the paddle end, the bottom of the flume is flat for 35.5 m, where the toe of the beach is located. From this point, the beach slopes upward with an initial slope of 1:15. The initial shoreline was situated at $x = 0\,\mathrm{m}$, roughly 77 m from the paddle (see Figure 4.1). The beach consisted of fine sand with $D_{10} = 0.15\,\mathrm{mm}$, $D_{50} = 0.25\,\mathrm{mm}$ and $D_{90} = 0.37\,\mathrm{mm}$, and a density of $\rho_s = 2650\,\mathrm{kg/m^3}$.

The experiment consisted of bichromatic waves with wave heights $H_1 = H_2 = 0.3253\,\mathrm{m}$, group period $T_g = 21.37\,\mathrm{s}$ and wave periods $T_1 = 2T_g/11$, $T_2 = 2T_g/13$. The target surface elevation signal η is thus

$$\eta = H_1 \cos(2\pi t/T_1) + H_2 \cos(2\pi t/T_2), \tag{4.1}$$

where t is time. This signal is designed such that the signal repeats every two wave groups with $T_r = 2T_g$. The resulting effective short-wave frequency is $T_s = 2T_g/12 = 3.56\,\mathrm{s}$, meaning there are six waves in every wave group.

For the experiment we define z as the global vertical coordinate. Additionally, for simplicity in the equations, we introduce $\hat{z}$ to indicate the depth coordinate. With $z_b(x)$ being the location of the bed at the start of the measurements, we can thus link the coordinates with $\hat{z} = z_b - z$, such that $\hat{z} = 0\,\mathrm{m}$ corresponds to the initial bed level.

Instrumentation

The setup of the instrumentation is shown in Figure 4.1. The experiment featured an array of Acoustic Wave Gauges (AWG) for measuring the water depth, Acoustic Doppler Velocimetry probes (ADV) for measuring velocities, Pore Pressure

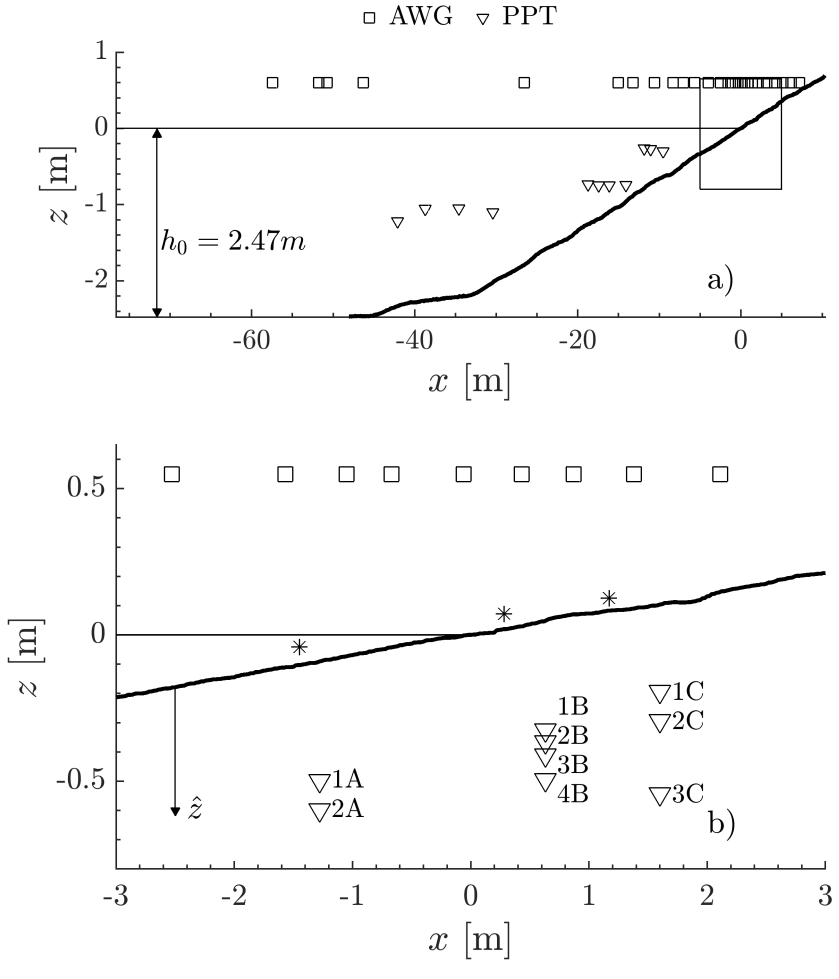

Figure 4.1
Overview of the initial bed level and instrument locations. Panel *a* shows the full flume and panel *b* shows a small section around the still water line. The squares, triangles and stars indicate the locations of wave gauges, pressure sensors and ADV's (velocity) respectively. The numbers show the indexing used to denote the different pressure sensors (see Table 4.1 for their locations). The pressure sensors in the water column in panel (a) were used for other experiments, not for measuring pore pressures.

Transducers (PPT) for measuring pressure, a profiler for measuring bed profiles before and after each run, and an array of other instruments not used in this study. The AWGs were installed in the swash zone at approximately 50 cm intervals. The measured surface elevations η are defined relative to the initial water level or, at initially dry locations, the dry bed profile as measured by the profiler (see Sanchez-Arcilla and Caceres (2018) for details on the profiler). We also define h as the total water depth. The ADVs were installed 3 cm above the local bed position at the beginning of the run. The profiler was used to measure the bed profile after each 30-minute wave session, and has a 1 cm vertical accuracy. Here it is important to consider that the profiler transect is in the middle of the flume, whereas the other probes were located closer to the flume wall. This means that there are discrepancies between the local bed levels at the probes and the measured profile.

Before the PPTs were buried, the opening of each probe was covered with a thin piece of cloth to keep sediment from entering the probe. Initially, four PPTs were buried at the three cross-shore locations, where they were attached to poles holding the probes in place. The burial depth of the probes was decided by estimating an expected profile evolution and burying them below this expected erosion level. The top three probes were spaced out by approximately 5 cm, and the lower probe was put deeper, as far as the equipment around the burial section would allow. Note that for all locations, the probes were buried at a depth where they were always covered with water to ensure continuous measurements. The precise depth of the buried sensors can be seen in Table 4.1.

Prior to the experiment analysed, multiple runs with different wave conditions were conducted, compacting the sediment. Just before the experiment run analysed in this paper, the beach was reshaped to its initial profile, during which the top layer of the beach was compacted manually. Unfortunately, due to one malfunctioning probe and two probes being exposed early in the experiments, the data from these probes is not used (these probes are not shown in Figure 4.1).

Data treatment

The acoustic wave gauges displayed spurious oscillations with a frequency of approximately 10 Hz, which was removed using a low-pass filter with a cut-off frequency of $f = 8\,\mathrm{Hz}$, similar to Van der Zanden et al. (2019a). The PPT sensors were first calibrated by filling the flume to two different water levels, measured at the paddle, ($h_{paddle} = 2.47\,\mathrm{m}$ and $h_{paddle} = 2.665\,\mathrm{m}$) and measuring the hydrostatic water pressure under these stagnant conditions. For the rest of the study we are mainly interested in the dynamic pressure $\tilde{p}$ in excess of the hydrostatic $\bar{p}$. Pressure gradients were estimated at the midpoint between two sensors by

$$\Delta\tilde{p} = \frac{\tilde{p}_{deep} - \tilde{p}_{shallow}}{\hat{\tilde{z}}_{deep} - \hat{\tilde{z}}_{shallow}}. \tag{4.2}$$

Due to the different instruments placed in the flume, the cross-shore locations of the AWG and PPT probes are not identical. To minimize the effect this has on the results, the time delay between the PPT location and its AWG probe was

estimated by measuring the time lag between neighbouring AWG probes using cross-correlation, and interpolating this time lag to the PPT location.

The ADV probes measured the velocity at a frequency of 100 Hz. The raw signal was noisy, and the dry periods interrupted the otherwise continuous signal. Therefore, the raw signal was smoothed using a Gaussian smoothing operation with a window size of 10. Furthermore, the dry periods were identified and removed from the signal.

The transient build up of pressure due to the gradual increase of the groundwater setup in the beach means that the experiments initially are not in equilibrium. Therefore, all intraswash analyses and modelling is done on a subset of the data, ranging namely $t = 1000 - 1800\,\mathrm{s}$. This interval was determined after visual inspection of the pressure time series, showing no change in mean pressure. For this reason, any build-up effects on the measured pressure and pressure gradients should be negligible.

4.2.2 Analytical model

The analytical model is based on the theory of Biot (1941), which assumes an isotropic soil-water mixture and Darcy-type porous flow. Importantly, the soil is not necessarily fully saturated, meaning that air bubbles can make the pore fluid compressible. Also the soil skeleton itself is assumed to behave as a linear elastic material. Following Biot (1941), multiple subsequent works have aimed to model stresses and pressures in the soil under waves (see Table 10.1 in Sumer and Fredsøe (2002)). Most notable are the theories by Yamamoto et al. (1978) and Hsu and Jeng (1994). The former developed a model for pore pressures and stresses for harmonic bed pressures with a bed that is infinitely deep. Hsu and Jeng (1994) expanded upon this by allowing a finite bed depth, and allowing for anisotropic Darcy flow resistance.

Our analysis has a similar approach as Guest and Hay (2017), also assuming that the shear modulus G of the porous bed is comparatively large, meaning that we assume the bed to be fully rigid in comparison with the pore fluid. We model the pressure at any arbitrary depth $\hat{z}$ as the sum of $2N + 1$ harmonic components:

$$p(\hat{z}, t) = \sum_{j=-N}^{N} p_j^*(\hat{z}) e^{it\omega_j}, \quad p(\hat{z}, t) \in \mathbb{R}, \tag{4.3}$$

where $p_j^*(\hat{z}) \in \mathbb{C}$ is the complex amplitude of wave component j at depth $\hat{z}$. Here ω_j is the angular frequency, linked to the wave number $\tilde{k}_j$ by the dispersion relation $\omega_j^2 = g\tilde{k}_j \tanh(\tilde{k}_j \bar{h})$, with $\bar{h}$ being the mean water depth where we use the average measured water depth and $g = 9.81\,\mathrm{m/s^2}$ is the gravitational acceleration. The theories of Yamamoto et al. (1978) and Hsu and Jeng (1994) give descriptions of these complex amplitudes p^* under different circumstances. We follow the description by Guest and Hay (2017) who use the approach of Yamamoto et al.

(1978) and introduce a tuning parameter a (s/m^2):

$$p_j^*(\hat{z}) = P_j^* \exp(-\tilde{k}_j' \hat{z}), \quad \tilde{k}_j' = \tilde{k}_j \left(1 + \frac{i\omega_j a}{\tilde{k}_j^2}\right)^{1/2}. \tag{4.4}$$

Here $P_j^* \in \mathbb{C}$ describes the amplitude and phase for wave component j at the bed and a is a parameter describing the elastic properties of the sand/water mixture. One can interpret a as the constant that describes the magnitude of the amplitude decay and time-lag, where larger values correspond to stronger amplitude decay and larger time-lags.

It remains to define the complex amplitudes P_j^*. We can define these using the measured surface elevations and assuming hydrostatic pressure ($p(0,t) = \rho_w g h$, with $\rho_w = 1000\text{kg/m}^3$ being the density of water), which is acceptable since the waves are shallow water waves. This gives us the relation

$$p(0,t) = \sum_{j=-N}^{N} P_j^* e^{it\omega_j}. \tag{4.5}$$

Finally, we calculate these complex amplitudes using the discrete Fourier transform.

In this study, we use the parameter a for calibration. However, this constant also has a meaningful physical definition. As described by Guest and Hay (2017), a is defined as

$$a = \frac{\gamma}{k_c}\left(n\beta + \frac{1-2\nu}{2(1-\nu)G}\right), \tag{4.6}$$

where $\gamma = \rho_w g$ is the weight of the pore fluid, k_c is the hydraulic conductivity, ν is Poisson's ratio, n is the porosity and β is the compressibility of the pore fluid. The latter is largely dependent on the air content in the beach, increasing with larger air content (Guest and Hay, 2017).

The theory above can also be applied to model pressure gradients. Given that we assumed an isotropic soil/water mixture in the first place, we can express the vertical pressure gradient as taking the vertical derivative of Equation (4.3), and using the chain rule:

$$\frac{\partial p}{\partial \hat{z}} = \sum_{j=-N}^{N} -\tilde{k}_j' p_j^*(\hat{z}) e^{it\omega_j}. \tag{4.7}$$

The Biot equations with a Darcy flow resistance are linear (assuming time-invariant material properties), so a linear superposition can be used to predict pressures for an arbitrary seabed pressure $p(0,t)$.

4.2.3 Shields parameter

We will also study the effect vertical pressure gradients have on the sediment weight in the Shields parameter θ:

$$\theta = \frac{\tau/\rho_w}{g(s-1)d}, \tag{4.8}$$

where τ is the bed shear stress and $s = \rho_s/\rho_w$ is the specific gravity of sediment, and d is the particle diameter, here chosen as $d = D_{50}$.

To investigate the influence of the pressure gradient, we use the modified Shields parameter θ' from (Sumer et al., 2011):

$$\theta' = \frac{\tau/\rho_w}{g(s-1)d - g\left(\frac{\partial p/\gamma}{\partial \hat{z}}\right)d}, \tag{4.9}$$

which models the effect of the pressure gradient on the effective submerged particle weight. In our analysis we will however not look at the Shields parameter directly, instead we recognize that

$$\theta \propto u|u|/(s-1) \tag{4.10}$$

$$\theta' \propto u|u|/\left((s-1) - \frac{\partial p/\gamma}{\partial \hat{z}}\right) \tag{4.11}$$

which enables us to analyse the effect of the added pressure gradient term, without the requirement of calculating a bed shear stress. We call the right sides in the relations (4.10) and (4.11) the transport mobility.

4.2.4 Metrics

We use two metrics to assess the model performance. We define the normalized Root-Mean-Squared-Error (nRMSE) as:

$$nRMSE = \frac{\sqrt{\frac{1}{N}\sum_i^N (y_{s,i} - y_{r,i})^2}}{s_r}, \tag{4.12}$$

where N is the number of samples, s_i is the $y_{s,i}$-th sample, $y_{r,i}$ is the ith reference value and s_r is the sample standard deviation defined as

$$s_r = \sqrt{\frac{1}{N}\sum_i^N (y_{r,i} - \bar{y_r})^2}, \tag{4.13}$$

where $\bar{y_r}$ is the mean of y_r. In the above equation, $y_{s,i}$ corresponds to modelled (sampled) values and $y_{r,i}$ refers to experimentally measured (reference) values. A low nRMSE value thus corresponds to small errors. Finally, the correlation between signals is measured using the Pearsons' correlation coefficient r^2.

4.3 Results

4.3.1 Pressure observations

Figure 4.2 shows the amplitude spectrum of the surface elevation and the measured pressure at three depths at section C. The peak corresponding to the group

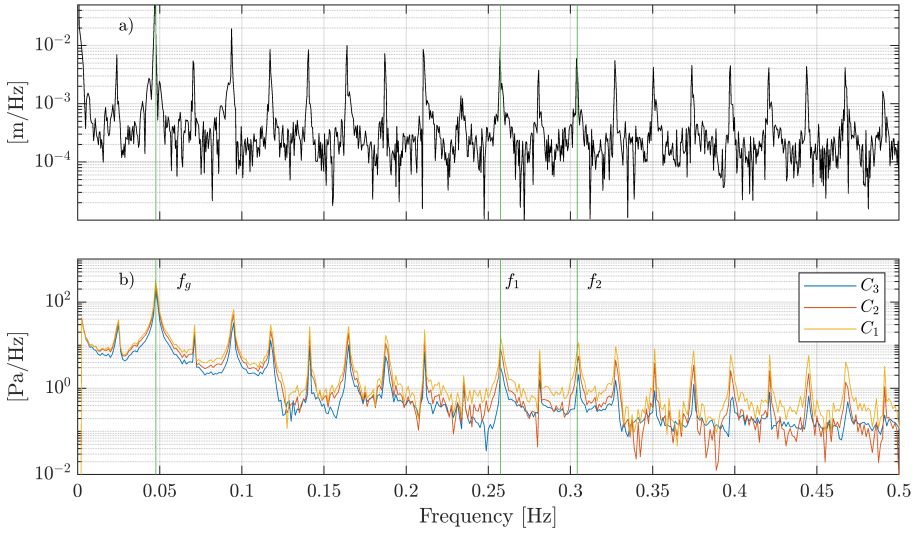

Figure 4.2
Spectrum showing the magnitude of the surface elevation (a) and the measured pressure in the bed (b) at location C. The green vertical lines show the group frequency f_g and the two bichromatic frequencies f_1 and f_2.

frequency is highest in both panels. Comparing the amplitude spectrum of the surface elevation with the pressures, we can see that the surface elevation has more high frequency content than the pressure signals. Moreover, the deeper sensors show lower amplitudes compared with the shallowest sensor, especially at higher frequencies.

The short-wave peak corresponding to T_s (corresponding to a frequency of 0.286 Hz) does not appear large compared to neighbouring peaks. Also the two peaks corresponding to the bichromatic wave components (0.257 Hz and 0.304 Hz) are not considerably larger. This can be explained by the waves transforming while travelling from the paddle to the beach, and the waves breaking prior to the wave-gauges. The other peaks are harmonics and (partially) stem from interactions between the swash and incoming waves.

Figure 4.3 shows the observed water depths h, pressure deviations $\tilde{p}$ and pressure gradients between the sensors. The figure clearly shows the difference in hydrodynamical forcing, especially between location A and locations B and C. For instance, at locations B and C it is clearly visible that the bed becomes dry for extended periods between the wave groups (i.e. between $t = 1252 - 1262\,\mathrm{s}$), whereas the dry periods at location A are considerably shorter (seen as the flat periods with $\eta = 0$). Furthermore, some waves recorded at location A are not recorded at locations B and C; for instance the middle wave group shows three distinct large peaks at location A but only one large and one small peak at locations B and C. This is probably due to wave-swash interactions in the lower swash, meaning

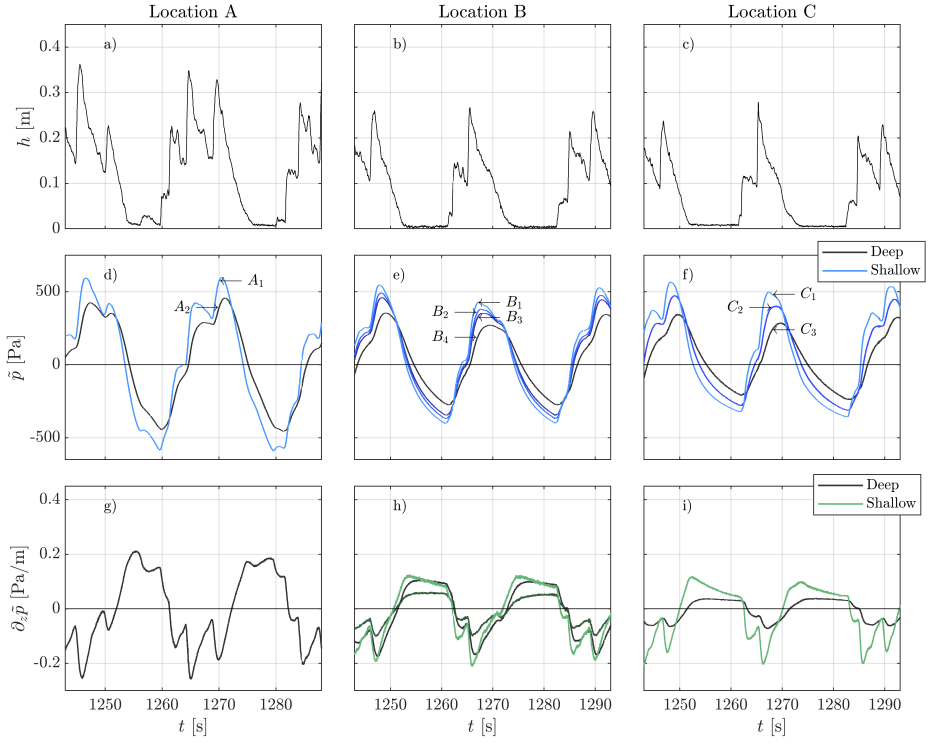

Figure 4.3
Figure showing the measured water depth (panels a to c), pressure deviation (panels d - f) and calculated pressure gradient according to Equation 4.2 (panels g - i). For panels d - i, the colours scale from the deepest sensor (dark) to the shallowest sensor (light). The arrows in panels (d-e) show the sensor corresponding to the line pointed to.

Table 4.2
Statistical metrics comparing the modelled and measured pressure signals, as well as the calculated and modelled pressure gradients (shown in between the sensors). The calibration for a is done for each location, as explained in Section 4.3.2.

	Location A		Location B				Location C		
Sensor nr	1	2	1	2	3	4	1	2	3
a (s/m^2)	25.9		37.7				39.6		
nRMSE (-)	0.223	0.178	0.186	0.185	0.197	0.199	0.129	0.101	0.432
R^2 (-)	0.95	0.98	0.97	0.97	0.96	0.96	0.99	0.99	0.93
grad nRMSE (-)	0.328		0.278	0.993	0.232		0.286	0.784	
grad R^2 (-)	0.91		0.93	0.92	0.95		0.96	0.99	

that certain waves do not reach the upper locations or that waves have merged. Comparing locations B and C, the differences in water depth are small.

The pressure response (panels d - f) show similar trends at all three locations, i.e. amplitude decay and a time lag that increases with the burial depth of the sensor. Note that at the three locations, the sensors are buried at different depths, meaning we cannot directly compare the amplitudes between the locations. Lastly the pressure gradients are calculated using Equation (4.2) and shown in panels (g - i). At all three locations we see positive pressure gradients (i.e. overpressure deeper in the bed) during the dry phase between wave groups, and negative pressure gradients during the presence of waves. Location C shows the expected behaviour according to the theory of Yamamoto et al. (1978), where the pressure gradient calculated closer to the bed surface has larger amplitude. However, at location B this does not seem to be the case as the pressure gradient between probes B2 and B3 display a smaller amplitude compared to the other two gradients. This is further discussed in Section 4.4.2.

4.3.2 Model calibration

The pressure model features one constant a that requires calibration. Since this constant is linked to physical properties of the beach that can differ per location, the calibration is done once for every cross-shore location. The calibration is based on the nRMSE values of the pressures (only pressures were used, not pressure gradients). Specifically, the individual nRMSE values, corresponding to each probe, were squared and minimized. The result of the calibration, and its corresponding nRMSE and r^2 values for both the pressure and the pressure gradients can be seen in Table 4.2. It is interesting to note that the calibration for location A, which is the most seaward location, has the lowest values of a. This will be discussed further in Section 4.4.4.

Panels a, c and e in Figure 4.4 compare the measured and modelled pressures. It is clear that the overall pressure behaviour is modelled well (see also Table 4.2). At all three locations, the modelled pressures corresponding to the shallower burial depths seem to slightly overpredict the pressures, which is most pronounced for the most shallow probe at location C. This overshoot could possibly be explained

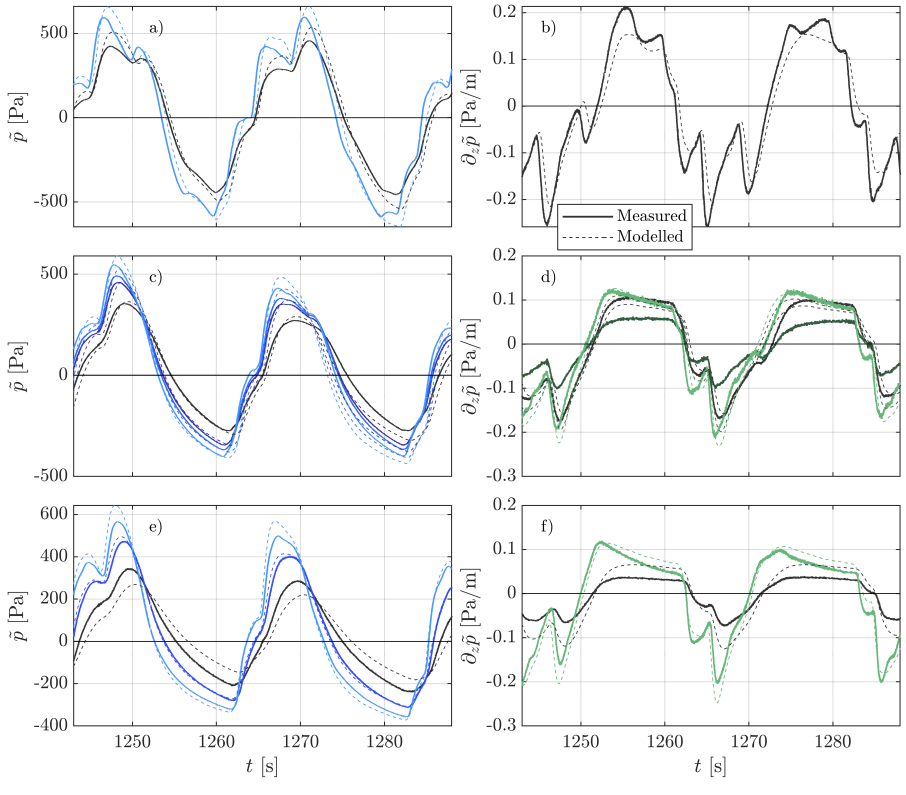

Figure 4.4
Snapshot of measured and modelled pore pressures (panels a,c,e) and estimated and modelled pressure gradients (panels b,d,f) using Equation (4.2). The continuous lines show measured results and the dashed lines show modelled results. The brightness of the colours are an indication of the depth, where the lighter colours correspond to locations closer to the bed surface. Panels a,b, c,d and e,f correspond to locations A, B and C respectively.

by the bed level changing, and is discussed further in Section 4.4.3. Furthermore, the phasing of the modelled pressures generally corresponds well to the measured signals. However, especially at location A there is a small lag between the modelled and measured signals.

Panels b, d and f show a comparison between the modelled and measured pressure gradients. Again the modelled pressure gradients correspond well to the measured gradients. Location C shows somewhat overpredicted pressure gradients, which mirrors the overpredicted amplitude of the pressure while location A shows a well-modelled pressure gradient. Location B, however, shows some anomalous behaviour where the measured pressure gradient between the middle two sensors B_2 and B_3 is much lower than the other locations. This is contrary to the expectation that larger gradients occur closer to the bed, which is mirrored in the modelled pressure gradients. In Table 4.2 it is clear that this location is associated with a relatively large error. This is further discussed in section 4.4.2.

The model captures both the quick response to the rapidly increasing water depth as a wave arrives, as well as the slow pressure decay during dry periods at Locations B and C. The same can be said for the pressure gradient behaviour, where, even though the modelled magnitude is slightly off, the pressure gradient closer to the bed surface displace more rapid decay compared with the pressure gradient deeper in the bed.

4.3.3 Applying the model

The model can be used to give insight into how specific wave frequencies influence the pressure in the bed. Panels a and b in Figure 4.5 show how the two different frequency components (a short-wave frequency and the group frequency) are transferred into the bed, and how this signal is attenuated and displaced. The higher values of a clearly lead to stronger decay and larger time lags. Also, higher frequencies are attenuated quicker compared with lower frequencies, that penetrate further through the bed with a smaller time-delay. This is because the vertical scale is dictated by k'. Panels c and d show the amplitude and phase of the pressure gradient (relative to a given pressure p_0 at the bed). It is clearly visible that higher frequency wave-components have a larger influence on the pressure gradient at the bed, however, for $\hat{z} < 0.25\,\mathrm{m}$ this reverses, and the group-frequency component penetrates further into the bed. The phase shows the same frequency dependency for the gradient as for the pressure. However, the phase at $\hat{z} = 0$ is different, namely approximately $-3\pi/4$. As Guest and Hay (2017) showed, $\varphi(\tilde{k}') \approx \pi/4$, because $i\omega a/\tilde{k} >> 1$. This means that $\varphi(-\tilde{k}') \approx -3\pi/4$.

The model provides a means to calculate pressure gradients at the bed surface by using Equation (4.7). Panels d to f in Figure 4.6 show the modelled pressure gradient, normalized with the specific weight of water $\gamma = \rho_w g$, at 1 cm below the bed. This is because the modelled signal at the bed ($z = 0$) shows some high-frequency noise which makes interpreting the signal more difficult. The pressure near the bed clearly contains more high-frequency content, due to the amplitude of the pressure gradient increasing with higher frequencies at the bed surface.

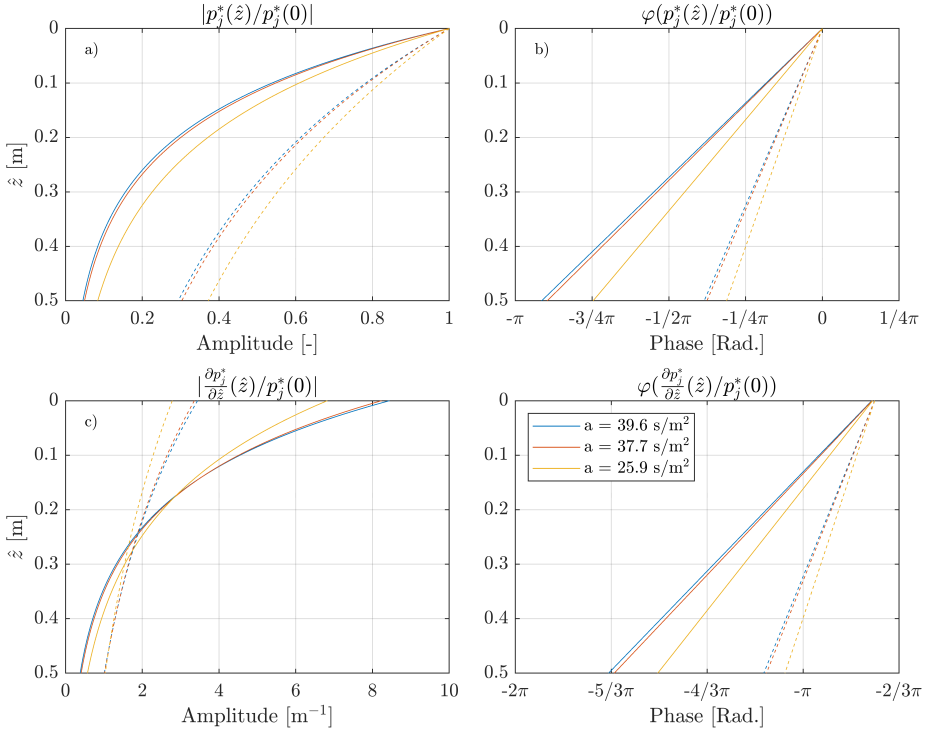

Figure 4.5
Figure showing the amplitude (a) and phase (b) of $p_j^*(\hat{z})/p_j^*(0)$ and amplitude (c) and phase (d) for $\frac{\partial p_j^*}{\partial \hat{z}}/p_j^*(0)$, for different chosen frequencies. Here the amplitude is denoted with $|.|$ and the phase with $\varphi(.)$. This is shown for the three different values of a that gave the best fit for the three sections. The continuous line corresponds to the short wave frequency $T_s = 3.56\,\mathrm{s}$ and the dashed line corresponds to the group frequency $T_g = 21.35\,\mathrm{s}$. Note, the x axes are different for different panels.

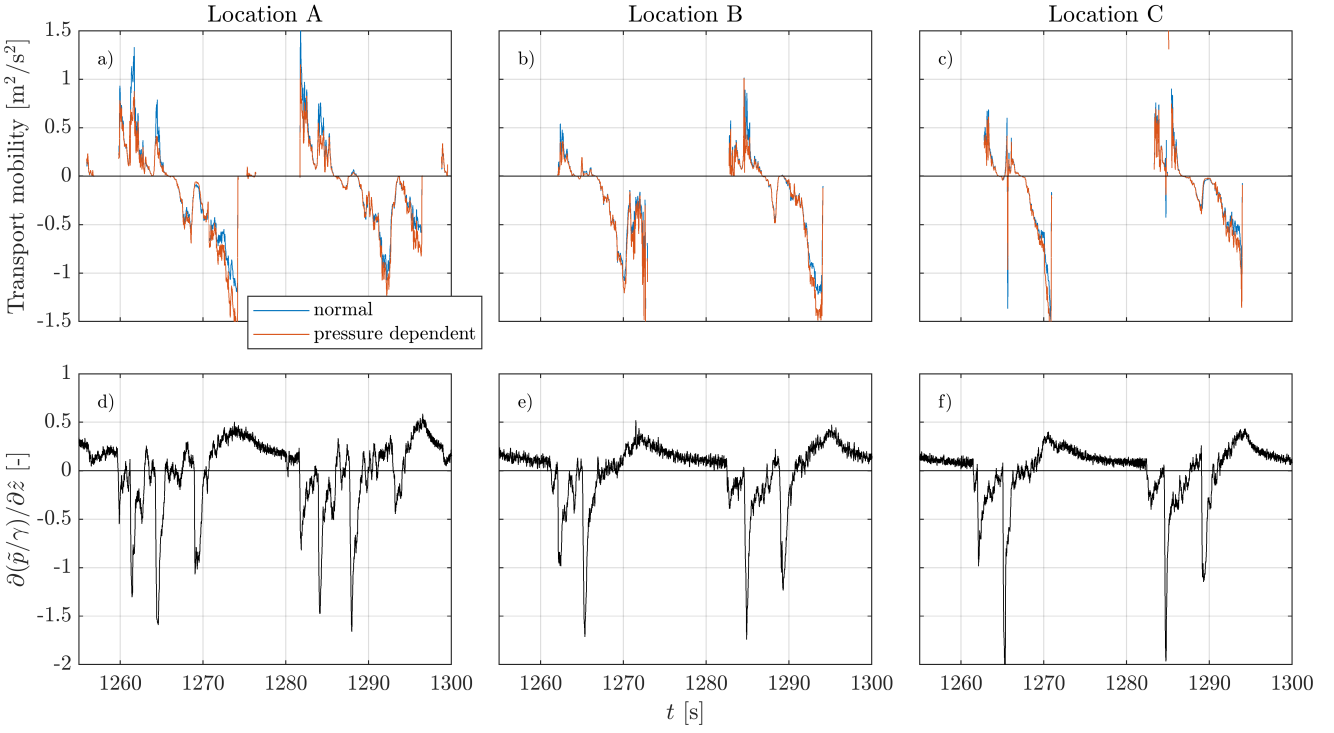

Figure 4.6
Figure showing the measured cross-shore squared velocities (panels a - c) where the blue line is the raw squared velocity and the red line incorporated the pressure correction as described in relations (4.10) and (4.11) and modelled vertical pressure gradients (panels d - f) at the three different locations. Here positive transport mobilities correspond to onshore-directed transport, and negative transport mobilities corresponds to offshore-directed transport.

At all three locations, the pressure gradient features strong negative spikes that coincide with instantaneous increases in water depth. These moments correspond to broken bores arriving at the particular location, and shows that these bores have an immediate and pronounced influence on the pressure gradient in the top layer of the soil. The maximum positive pressure gradient at the locations are roughly 0.5 (non-dimensional) for section A, and 0.4 for sections B and C. This corresponds well with the measurements of Sumer et al. (2013) who recorded similar non-dimensional pressure gradients at similar locations.

Panels a to c give an indication of the effect the pressure gradient has on the Shields parameter, by looking at the transport mobility defined by relations (4.10) and (4.11). This is shown both raw and corrected for the pressure. For both signals, positive velocities indicate a shoreward (uprush) motion. At all three sections the particle weight is increased during uprush, meaning that the effective Shields parameter is lower. Especially at location A during the uprush, the Shields parameter is momentarily almost halved due to this effect. During the backwash however, the particle weight is lower, leading to a higher off-shore directed Shields number. We will discuss these results and their limitations further in section 4.4.5.

4.4 Discussion

4.4.1 Comparison with other studies

The measurements in this study complement the findings of Guest and Hay (2017) (gravel bed with $D_{50} \approx 5\,\text{mm}$) that vertical pressure attenuation and phase shifting also play an important role for the pore-pressure behaviour in a sandy bed. Interestingly, this contradicts the findings of Raubenheimer et al. (1998), who measured pore pressure gradients on a natural beach with $D_{50} = 0.2\,\text{mm}$, very similar to the sediment used in this study. They did not find considerable phase shifts in their data. This could partially be explained by the fact that their study sampled the pressure at 2 Hz, which is considerably lower than in our study (100 Hz), and they analyzed components with frequencies of around 0.2 Hz and lower. However, the recent study of Stark et al. (2022) analyzing pore pressures on a beach consisting of medium/coarse sand confirms that phase-shifting plays an important role. This is in line with our conclusion that the pressure measurements clearly display rapid attenuation and phase shifts. We conclude that in order to understand pore-pressure fluctuations on intraswash timescales, it is important to include the effect of phase shifts and additional attenuation due to the presence of compressible gas in the pore fluid.

4.4.2 Measurement limitations

There are some limitations to the presented measurements. Due to the pressure attenuation and the burial depth of the pressure sensors, certain high-frequency or short-lived phenomena were not captured in these measurements. Sumer et al. (2011,

2013) directly measured the effect of vortices induced by wave-breaking, and their effect on the pore-pressure immediately below the bed surface. The morphodynamic variability of the bed during longer experiments makes determining a priori burial depths difficult, especially close to the bed surface. For future experiments, a setup that can be vertically adjusted during experiments such as the one by Baldock et al. (2001) might be more suited for this.

The experimental campaign experienced some challenges that influence the results. The most apparent one is the effect of scour near instruments. This is a known effect for probes mounted from above (see for instance Sumer et al. (2013).) The scour depth was measured to be $\mathcal{O}(1 - 5\,\mathrm{cm})$, depending on location. The combined effects of the scour and the overall morphodynamics meant that the top two sensors in the surf section were exposed and hence needed to be taken out. Furthermore, one sensor malfunctioned while buried. This meant that two locations had fewer sensors than originally planned (four sensors at every cross-shore location). Nonetheless, the data captured provides useful insight into the behaviour of the pore pressure around the shoreline location.

Another issue has to do with the unexpected observation that the difference in pressure between the middle two probes at location B was very low, leading to a small measured pressure gradient. This becomes more apparent when comparing this with the modelled pressure gradient (Figure 4.4, panel (d)), where the modelled pressure gradient shows the expected amplitude decay whereas the measured pressure gradient does not. Also the associated nRMSE for the pressure gradient is very large at this location. A possible explanation for this could be interference between instruments, as the instruments were installed in close proximity to each other and attached to the same pole.

4.4.3 Analytical model performance

The analytical model used in this paper gives insight into the pressure propagation from the waves into the bed. The model performs well, in the sense that it describes the pressure amplitude and phase reasonably well. This is backed up by the statistical metrics where most instruments display an nRMSE lower than 0.2 and an R^2 higher than 0.95. Only the shallowest swash probe displays considerably larger nRMSE of $0.4 - 0.6$, depending on the run. Similarly, the model reproduces the pressure gradients reasonably well, except for location B for the aforementioned reasons (see Section 4.4.2).

It is important to consider the assumptions the model relies on, and the implications for the interpretations. First and foremost, the modification of Guest and Hay (2017) assumes $G\beta' >> 0$, which means that the stiffness of the porous bed matrix should be much higher than the compressibility of the pore fluid. Here β' is the compressibility of water. In our case, $G\beta' \approx 300$, making it safe to assume that the model can be applied. Furthermore, the model assumes homogenous sediment properties, such as grain size, saturation and compactness. These might be more applicable to a laboratory environment compared with natural beaches. Nonetheless, Guest and Hay (2017) and Baldock et al. (2001) show that models

assuming vertically uniform sediment properties can accurately model the pressure behaviour in the field. Furthermore, as also mentioned by Baldock et al. (2001), because the model is based on the pressure from the surface elevation only, non-hydrostatic effects are not taken into account. Such effects have been observed in the small-scale laboratory experiments by Sumer et al. (2011, 2013), who observed that individual eddies, originated from a broken wave, can lead to large ($\mathcal{O}(\partial\gamma p/\partial\hat{z}) > 1$) positive pressure gradients near the bed surface responsible for rapid sediment suspension. These latter mentioned effects cannot be modelled using linear wave-theory and hence are not incorporated in the present study. However, if one assumes that the dynamics in the bed still can be described by linear Biot theory, a description of p_0 including the effects from nonlinear flow phenomena is sufficient.

Another assumption made by Yamamoto et al. (1978) is that the bed has an infinite depth. Since the flume has a depth of 2.5 m this assumption is clearly violated. The model by Hsu and Jeng (1994) provides a solution which incorporates a finite depth of the bed. However, this model does not allow the simplification Guest and Hay (2017) suggested. We can estimate the importance of the finite depth by investigating the amplitude of the pressure and pressure gradients for different wave components at the flume wall. Using the lowest value of a between the sections, corresponding to the lowest damping, we can estimate that $(p^*/p_0^*)\,|_{\hat{z}=2.47\mathrm{m}} = 0.008$ and $((\partial p^*/\partial\hat{z})/p_0^*)\,|_{\hat{z}=2.47\,\mathrm{m}} = 0.021\mathrm{m}^{-1}$ for the wave-group component. All higher frequency components will thus have smaller amplitudes at this depth (for the short-wave component T_s these are $(p^*/p_0^*)\,|_{\hat{z}=2.47\mathrm{m}} = 4.8\cdot10^{-6}$ and $((\partial p^*/\partial\hat{z})/p_0^*)\,|_{\hat{z}=2.47\mathrm{m}} = 3.3\cdot10^{-5}\,\mathrm{m}^{-1}$). This shows that the effect of the finite depth is small. This is especially the case closer to the bed surface and for higher frequencies. Finally, it is important to consider that the model assumes a fixed bed, whereas the bed in the experiments is not fully static. For instance, intra-swash morphodynamics can be on the order of centimetres in seconds (Van der Zanden et al., 2015). Additionally, the locally observed scour observed during the experiment means that the bed level at the locations of the probes could be somewhat lower than recorded with the profiler. This could explain why for location C, the modelled pressure had an overpredicted amplitude for the top sensor, and an underpredicted amplitude for the bottom sensor.

4.4.4 Interpretation of variability in a

The value of a at Location A differs from the considerably larger values at Location B ($a_C/a_A \approx 1.53$). Using equation (4.6), we can try to explain this difference in the value of a using physical bed properties.

For instance, one argument uses that k_c is sensitive to the local packing (Van Gent, 1995) following the relation

$$k_c \propto \frac{n^3}{(1-n)^2}. \tag{4.14}$$

Keeping everything except k_c constant, the value of a depends strongly on the

local packing. As an example, consider the porosity being $n_A = 0.40$ at Location A and $n_C = 0.35$. This would then lead to

$$\frac{1}{k_{cC}} / \frac{1}{k_{cA}} = 1.75, \tag{4.15}$$

which combined with the fact that a is inversely proportional to k_c, more than explains the ratio between a_C and a_A.

Another possible difference between the locations is the local air content in the bed. In Equation (4.6), the compressibility is determined by the saturation of the bed (Verruijt, 1969):

$$\beta = S\beta' + \frac{1-S}{P_{atm}}, \tag{4.16}$$

where P_{atm} is the atmospheric pressure at the surface level. If we keep k_c constant and change the local bed saturation, we find that lowering the air content, meaning the saturation is higher, leads to a lower value of a. This explains the lower value of a at Location A compared with B and C, as this location is more offshore located where one would expect lower air content in the bed compared to more onshore locations.

Compared to Guest and Hay (2017), the value of a in our study is an order of magnitude higher (between $a = 25\,\mathrm{s/m^2}$ and $a = 40\,\mathrm{s/m^2}$ compared to $a = 2.9\,\mathrm{s/m^2}$). Using similar arguments as above, this difference can be explained by the difference in bed composition and its effects on the hydraulic conductivity and saturation.

4.4.5 Implications for sediment transport

In the context of sediment transport, it is important to note that there is a discussion about the validity of incorporating the change to the apparent weight due to vertical pressure gradients in the Shields description (Baldock and Nielsen, 2010; Francalanci et al., 2010), particularly when it comes to bedload transport. Baldock and Nielsen (2010) argue (amongst other things) that the additional seepage-related force only acts within the bed, whereas for particles outside the bed the pressure gradient is essentially zero. However, Francalanci et al. (2010) argue that the pressure gradient does influence particle entrainment, and thus sediment transport in general. Regardless of the discussion, Baldock and Nielsen (2010) note that the vertical pressure gradient can influence the sheet flow layer and experiments by Sumer et al. (2013) show that pressure gradients can lead to rapid suspension events. Keeping these points in mind, we believe that the Shields parameter provides a useful metric to analyse the impact of pressure gradients on sediment transport.

In this paper we chose to limit the analysis to the effective particle weight using the approach of Sumer et al. (2011). Modelling the effect of vertical pressure gradients is not limited to modifying the effective sediment weight in the Shields parameter. For instance, one can modify the critical Shields stress (Cheng and

Chiew, 1999), or modify the Shields parameter to include effects on the boundary layer through infiltration, possibly in conjunction with the modified sediment weight (Conley and Inman, 1994; Anderson, 2015; Nielsen et al., 2001; Francalanci et al., 2008). This boundary layer effect has the opposite effect to the modified particle weight, leading to increased friction during uprush and decreased friction during the backwash. In fact, Lohmann et al. (2006) found this to be the dominant effect of the two, meaning that infiltration increased bed friction and exfiltration decreased bed friction. However, using any of the approaches mentioned above, the friction velocity related to the boundary layer shape, is needed. To estimate this from measurements would require even more approximations, which would lead to large uncertainties. For this reason, we stuck to the approach of modifying the effective sediment weight. Now that there exist models that can resolve the detailed flow in the swash zone and model sediment transport and morphodynamics, for example Cheng et al. (2017); Kim et al. (2019) and Kranenborg et al. (2022), numerical models can be great tools for analysing the aforementioned effects in detail, and investigate their relative importance for sediment transport under different conditions.

4.5 Conclusion

In this study we investigated the behaviour of pore pressure at different depths in the bed, under the forcing of bichromatic waves. This was done at three different locations around the still water line. The main conclusions are summarized as follows:

- New field-scale laboratory measurements of pore pressures at different depths, surface elevations and flow velocities were conducted at three different cross-shore locations in the swash zone of a sandy beach.
- The measurements clearly show that, for intraswash timescales, the pressure propagation in the bed is frequency dependent. Specifically, lower frequencies penetrate deeper into the bed and shift less, whereas higher frequencies experience more damping and larger phase shifting. This is in agreement with previous studies, e.g. Guest and Hay (2017) and Stark et al. (2022).
- An analytical model, based on the theory of Yamamoto et al. (1978) and Guest and Hay (2017), was able to reproduce the pressure and pressure gradient well for all three cross-shore locations.
- The calibrated model value a was highest for the most onshore measurement location, and the lowest for the most offshore location. This variation of a can be explained in terms of local bed packing and bed saturation.
- During the uprush, the modelled effective sediment weight is increased due to the gradients. During the backwash, the pressure gradient has the opposite effect where the submerged weight is reduced significantly.

Acknowledgments

We would like to thank prof. K.M. Wijnberg for aiding with the supervision of T. Pauli during his Msc. thesis. This work is part of the research program Shaping The Beach with project number 16130, which is financed by the Netherlands Organisation for Scientific Research (NWO), with in-kindsupport by Deltares.

Chapter 5

Discussion

In the introduction (Section 1.1), we motivated the use of a depth-resolving model by pointing out the problems with practical models using parametrisations of swash processes. Examples of such processes that were mentioned were vertical structures in the suspended sediment flux due to nonuniform flow velocities and sediment concentrations, as well as effects of turbulence. In this chapter we address limitations of the research approach, revisit the processes behind vertical structures in the swash zone and discuss further implications of pore-pressures in the swash zone.

5.1 Research approach and model performance

In this thesis, a combination of intra-wave, depth-resolved modelling and large-scale laboratory experiments have been used. The model used the Reynolds Averaged Navier Stokes (RANS) equations combined with an advection diffusion approach for suspended sediment and a bedload formula. For the experiments, regular bichromatic waves were used to investigate pore-pressure gradients in a controlled laboratory flume. In this section, we discuss the choice of modelling and experimental approach, and provide suggestions for alternative approaches.

5.1.1 Hydrodynamics

Modelling turbulence

Starting with hydrodynamics, the RANS equations split the flow into a mean and turbulent component (see Pope, 2000, for details on the decomposition and derivations). A closure model is then needed to achieve a closed system, and the choice of closure model can vastly impact the resulting flow solution (e.g. Brown et al., 2016). Regardless of turbulence closure model, the RANS approach models turbulence at all scales at once. This is different from the Large Eddy Simulation (LES) approach, where a filter is applied to the momentum equations. This filter removes turbulent scales smaller than a chosen threshold from the equations, and instead models the influence of these turbulent effects on the larger flow using a turbulence closure model. Typically, this is done by explicitly resolving the larger flow structures above the threshold and using a subgrid-scale model for the unresolved turbulence. The difference in modelled turbulent scales also means that LES is inherently 3D, whereas the RANS approach can be used in 1D, 2D and 3D settings.

In this thesis, the RANS approach is used in a 2DV setting. This has implications for the model results and how one should interpret these. As shown in Chapter 3, the rising of air bubbles in a column of water cannot be modelled correctly using a 2DV model. Furthermore, Dalrymple and Rogers (2006) showed that wave-breaking is an inherently 3D process, even when waves arrive perfectly perpendicular to the shoreline. To investigate the importance of these issues, it is very valuable to conduct 3D simulations of alongshore uniform profiles, specifically to isolate the

importance of these 3D processes associated with breaking waves. Such studies could shed light on the runup issues experienced in Chapter 2.

Effects of bubbles and turbulence on the runup

The solitary wave study in Chapter 2 displays an overpredicted runup. This is not the case for the bichromatic waves in Chapter 3, where the hydrodynamics seem to be well predicted. The latter chapter introduced two major differences to the model compared with the former chapter, namely a term in the turbulence model and the bubble modification. Figure 5.1 shows the morphological change from models using the two modifications from Chapter 3 applied to the solitary case from Chapter 2. The figure shows that the biggest differences with the Chapter 2 setup comes from the bubble modification, not from the Wilcox (2006) limiter in the turbulence model. This shows that, similar to the bichromatic case, the removal of bubbles also results in increased friction for the solitary wave case. This is especially apparent during the uprush, which leads to a shorter runup. In this case, the maximum runup for the no limiter and no bubbles case is at roughly $x = 43\,\mathrm{m}$. This can be seen in Figure 5.1 where after $x = 43\,\mathrm{m}$ there is no or only little morphological change. The other two cases show runup maxima of $x = 47\,\mathrm{m}$ (default) and $x = 49\,\mathrm{m}$ (no limiter), respectively. This shows that the turbulence limiter, in this case, does not lead to an improved runup prediction, and that the improvement of the runup prediction can be attributed to the removal of bubbles.

Still, the improved model predicts a larger maximum runup than the maximum runup of 38.5 m in the experiments. This can possibly be due to infiltration effects. Even though these are usually deemed very small for sandy beaches (Masselink and Li, 2001), the long time between the solitary waves (15 minutes) means that the bed was relatively dry compared with a beach that is inundated every few seconds. This difference could be important as water infiltrates more easily into a dry bed (Horn, 2002). However, using the current model implementation this could not be investigated further.

An important sidenote here is that Chapter 2 showed that the roughness parameter was not a good tuning factor to get satisfactory model results. Increasing roughness artificially beyond reasonable bounds led to seemingly improved hydrodynamic predictions when looking at large scale metrics of the hydrodynamics, such as the runup. However, this can mask the underlying issue, in this case bubbles failing to rise in a 2DV setup. This should caution the modeller not to be too eager to tune models to global metrics, such as the runup, that do not incorporate crucial local flow details such as turbulence or bubbles near the bed.

5.1.2 Sediment dynamics

Effects of high sediment concentrations

The passive scalar approach is an efficient way of modelling suspended sediment transport due to its one-way dependence on the flow. However, at higher concentrations one can question the validity of assuming no effects from sediment grains

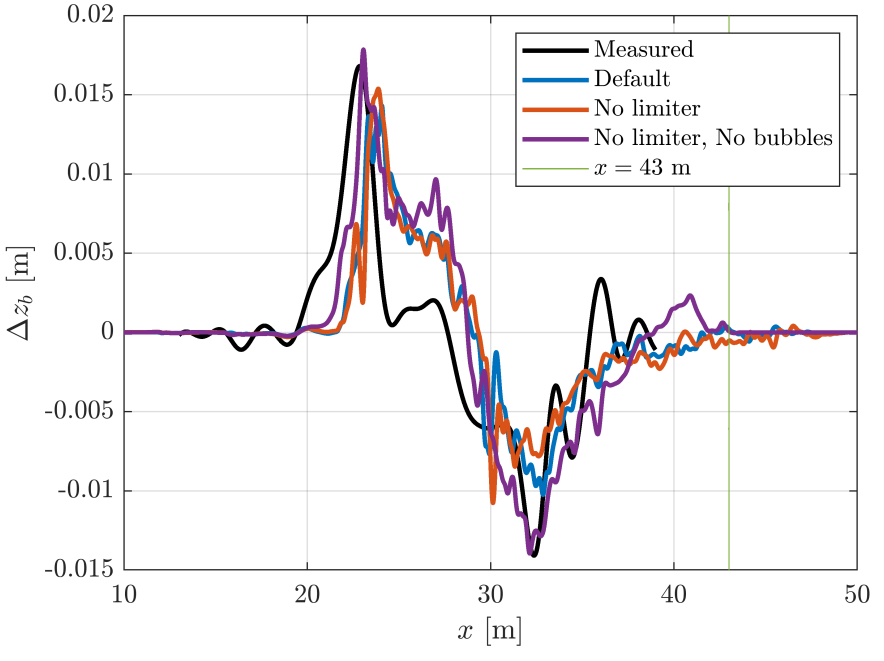

Figure 5.1
Comparison of morphological change after one solitary wave: the model setup from Chapter 2 (Default) and two models that include the turbulence and bubble modifications from Chapter 3. The results are shown relative to the measured profile change after three waves, rescaled to only one solitary wave. All model results are from models using the isoAdvector approach and the Engelund and Fredsoe (1976) reference concentration model. The vertical green line shows the maximum runup by the model including the turbulence and bubble modifications.

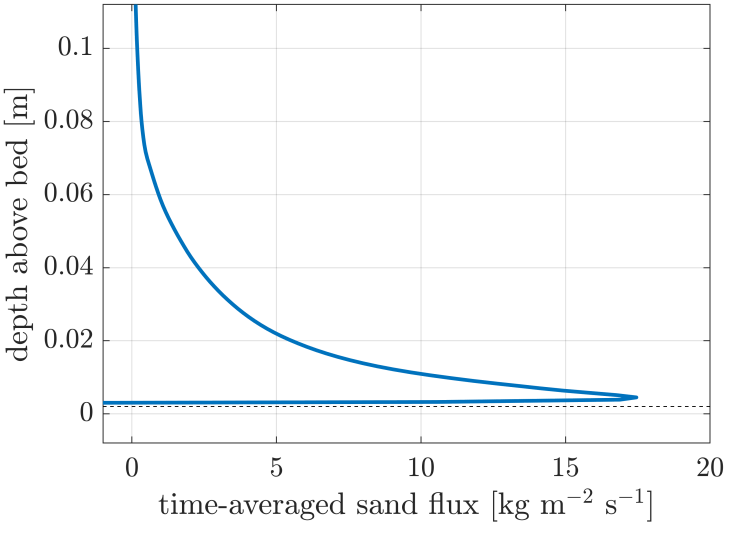

Figure 5.2
The time-averaged sediment transport flux just onshore from the initial shoreline (at $x = 0.03\,\mathrm{m}$) for the RESIST case from Chapter 3. The dashed line shows the reference height where the reference concentration is applied.

on the flow. Figure 5.2 shows that the majority of sediment transport in the model occurs very close to the bed, where sediment concentrations typically are high. Therefore, it is important to discuss possible ramifications of using a passive scalar approach in a setting with high sand concentrations.

The modelled concentrations in Chapters 2 and 3 reach up to at least 30% volumetric concentration. Taking a density of sand, $\rho_s = 2650\mathrm{kg/m}^3$ and water $\rho_w = 1000\mathrm{kg/m}^3$. This means that the effective density of the mixture is $\rho_m = 1495\mathrm{kg/m}^3$, which amounts to an increase of almost 50% over the density of water. Simultaneously, the effective viscosity changes in mixtures with high sediment concentrations (Boyer et al., 2011).

At these high near-bed sediment concentrations one can expect the passive scalar assumption to become invalid. For instance, high sediment concentrations also affect turbulence (Hjelmfelt and Mockros, 1966), and lead to hindered settling effects (Van Rijn, 2007). Kranenburg et al. (2014) applied extra damping terms to the standard $k - \epsilon$ turbulence model when studying sheet flow sediment transport. A similar modification was used by Kim et al. (2019) and Delisle et al. (2022) in their recent 2DV studies of sheet flow on the crest of a breaker bar. All these studies use the Euler-Euler approach. However, one can add the effect of sand concentration on turbulence also in a passive scalar setting.

Given the relative simplicity of the passive-scalar approach, the model performs rather well, especially in Chapter 3. This can partially be attributed to the power

of the well-tuned empirical models for the reference concentration. These empirical models do indirectly incorporate these effects in their calibration parameters, as they calculate a reference concentration very close to the bed based on the instantaneous Shields parameter. However, even if a local reference concentration is well modelled, for sediment transport predictions to be accurate, the advection and mixing of sediment also needs to be modelled well. The fact that the model is able to predict concentrations reasonably well with such a passive scalar approach is noteworthy, and shows that the model incorporates the most important processes relevant to sediment suspension and transport.

Implementation of the bed boundary condition

The present implementation of the model poses strong restrictions on the cell size near the bed. The reference concentration needs to be applied close to $z_a = 2D_{50}$ above the bed. The present model does this by modelling suspended sediment on a subset of the total mesh, where an integer number of layers below the reference height are removed. This means that, close to the bed, the maximum cell size is the reference height, which for grain sizes used in this thesis amounts to $z_a \approx 0.5\,\mathrm{mm}$. This is a tiny distance, leading to small cells near the bed, much smaller than would be required to resolve the boundary layer sufficiently. This also means that, if one wants to keep cell widths around $\mathcal{O}(cm)$ parallel to the bed, the aspect ratio close to the bed can become very large. This is undesirable for numerical reasons, but also negatively impacts the accuracy of the free surface modelling (Jacobsen, 2011). There are alternatives to this approach. García-Maribona et al. (2021) instead use a concept of cell openness to define whether a cell (and its faces on the bed interface) is part of the bed. However, for accurate boundary treatment it can be beneficial to have bed-parallel cells, something which their approach does not allow for. Another alternative is to use larger cells and calculate a representative concentration, or pickup, from an assumed concentration profile. This latter method has the benefit of increasing model efficiency and improving the aspect ratio of the cells in the process, but it does come at a cost of near-bed resolution. This is the method Quezada et al. (2019) used in their study using the REEF3D model. A similar method is also employed in Delft3D (Lesser et al., 2004).

5.1.3 Experiments versus real beach systems

In this thesis, the model is applied to two laboratory experiments. These were chosen for specific reasons. The solitary wave dataset (used in Chapter 2) by Young et al. (2010) provided a relatively simple hydrodynamic situation without complicated wave-swash interactions. The experiments provided detailed measurements of hydrodynamics as well as sediment dynamics and morphodynamics. The wave height is 60 cm, which is high compared with otherwise similar experiments (e.g. Sumer et al., 2011). This made it an attractive dataset for initial validations of the model. For the study of the importance of turbulence, bubbles and vertical

structures in the sediment flux, a more representative wave condition, which for instance features wave-swash interaction, was needed. Here, we chose the RESIST dataset as described in Van der Zanden et al. (2019a), which featured bichromatic waves. Again, the experiment measured detailed time series of hydrodynamics and sediment transport, and also measured morphodynamics every 30 minutes.

These experiments are different from the dynamics of real beaches in multiple crucial ways. One such important difference lies in the wave characteristics. Real beaches show wave climates that are irregular and can generally consist of different components with different individual characteristics. Furthermore, on real beaches waves are usually not strictly perpendicular to the beach, and the beach front itself can be curved. In other words, the strictly cross-shore flow present in this thesis is not generally representative of natural conditions. Another important difference with field experiments, or experiments featuring irregular waves, is that the total sediment transport can, under certain conditions, largely be controlled by a few strong events (Masselink et al., 2009). Therefore, it is important for models to be able to replicate this behaviour well, in order to both predict sediment transport rates correctly, but also to be able to learn the processes that drive these extreme events. In principle, it is reasonable to expect that depth-resolving models do not have more trouble simulating irregular wave scenarios. Nevertheless, it is prudent to verify this.

Overall, to improve confidence in the model it should be verified for more cases. Similarly to the study of Brown et al. (2016) who analysed the performance of different RANS turbulence models for spilling and plunging breakers respectively, sediment transport and morphodynamic performance can also differ for different wave conditions. Furthermore, apart from laboratory experiments, it is important to also validate and compare models with data from real natural beaches. The alongshore component should, in principle, not be an issue, as a similar model also based on the work by Jacobsen et al. (2014) has been applied in 3D settings (e.g. Li et al., 2021). Actually, one could reasonably expect the model to perform better in 3D conditions since the inherent 3D nature of the hydrodynamics (for instance bubble rise) can be captured more accurately.

5.2 Vertical uniformity of suspended transport

Intraswash depth-averaged models for sediment transport typically implement suspended sediment transport using a depth-averaged advection approach (we disregard diffusion here for ease of analysis) of this form or similar:

$$\frac{\partial hC}{\partial t} + \frac{\partial hCU}{\partial x} = (\mathscr{E} - \mathscr{D}). \tag{5.1}$$

Here h is the water depth, C and U the depth-averaged sediment concentration and velocity and $\mathscr{E}$ and $\mathscr{D}$ are the erosion and deposition rates. Some models (for example Pritchard and Hogg, 2003) that use this approach incorporate vertical structures in the deposition by making $\mathscr{D}$ a function of the near-bed concentration

C_b instead of C. This requires a model to calculate C_b, which uses, to some extent, an assumption or a model for the vertical structure of C. However, these structures enter not only in the deposition, but also influence the cross-shore transport of sediment, i.e. the second term in Eq. (5.1).

The importance of vertical nonuniformities for the sediment transport flux is investigated in Chapter 3. Such nonuniformities can mean that prematurely integrating or averaging the concentration and flow velocities predict faulty sediment fluxes (see Figure 5.3). Figure 5.4 shows similar results, but for the Young et al. (2010) case. Interestingly, for the solitary wave it seems that the uniform assumption holds rather well. In this section, the vertical dependence of sediment transport is discussed by means of investigating the difference between the solitary and the bichromatic cases.

5.2.1 Turbulence, pre-suspended sediment and wave-swash interactions

There are multiple processes that warrant discussing here. One such process is pre-suspended sediment. This is sediment that was brought in suspension by previous waves (or more generally, earlier suspension events), that has not yet settled to the bed. This sediment is then readily available for transport by following waves. This occurs for instance in the bichromatic case from Chapter 3, which displays a cloud of sediment that is more or less kept in suspension around the point of wave breaking. This means that pre-suspended sediment is readily available to be transported onshore. However, this is happening relatively far offshore from the swash zone, and Figure 3.7 shows very little exchange of sediment between the surf zone and the swash zone. Furthermore, the largest error in the flux in Figure 5.3 occurs further onshore from this point, around $x = 0\,\mathrm{m}$. Therefore, pre-suspended sediment is probably not key in explaining the importance of vertical structures.

Another candidate process, or rather family of processes, are the wave-swash interactions. These have been investigated experimentally, for instance by two consecutive dambreaks interacting (Chen et al., 2016), but also for more complex wave conditions in the lab (Erikson et al., 2005; Cáceres and Alsina, 2012; Alsina et al., 2018) and on real beaches (Hughes and Moseley, 2007). By definition, no wave-swash interactions are present for the solitary wave case. These do happen for bichromatic waves, and as such one could think they are suitable to explain the difference in importance of vertical structures. However, wave-swash interactions can increase sediment suspension and turbulence which actually leads to increased vertical uniformity. This is the same line of reasoning as used in Chapter 3 to argue that the uniform flux approximation works relatively well in the breaker zone. Furthermore, looking at panel (c) in Figure 3.4, the strongest interactions happen further onshore than the location where the uniform flux assumption F_u produces the largest error. Therefore, wave-swash interactions themselves are not a satisfactory explanation for the nonuniformities in the sediment flux.

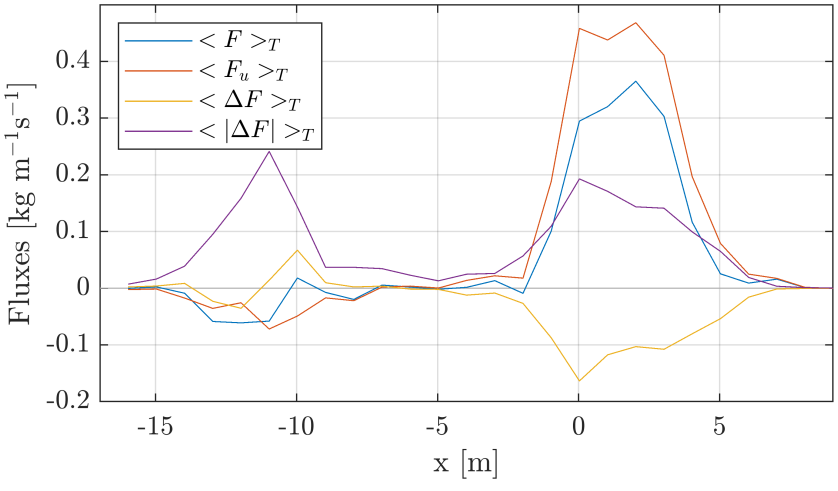

Figure 5.3
Copied Figure 3.10 from Chapter 3, showing the time-averaged fluxes F (including vertical structures), F_u (vertically averaged) and Δ_F (difference) for the bichromatic waves case. Here, $< . >$ denotes a time-averaging operation over the interval $T = [135, 135 + 3T_r]$.

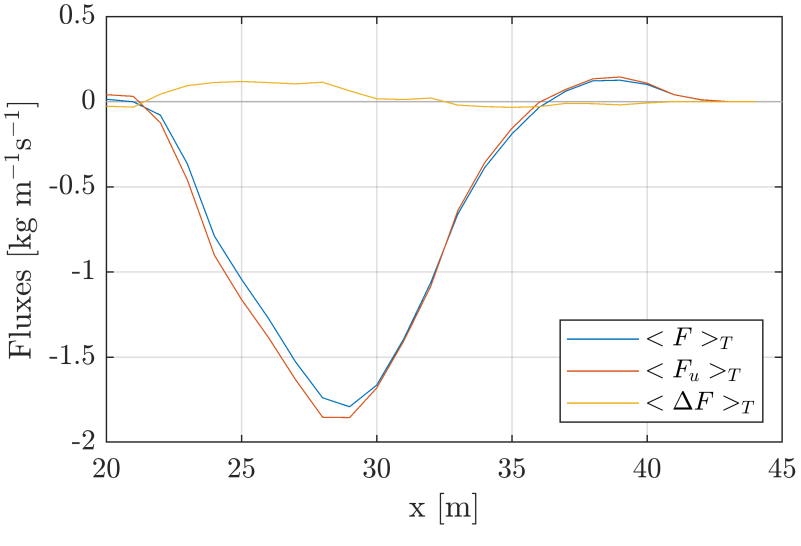

Figure 5.4
Time-averaged sediment fluxes F (including vertical structures), F_u (vertically averaged) and Δ_F (difference) for the Young et al. (2010) case, modelled using a model that includes the turbulence and bubble modifications from Chapter 3. Here the time interval is $T = 50\,\mathrm{s}$, which is the full duration of the simulation.

5.2.2 Vertical mixing

Instead of turning to complex flow phenomena for an explanation, the solution might present itself in a relatively simple explanation. The line of reasoning goes as follows: close to the bed the sediment concentration is generally higher than higher in the water column. The flow velocity displays the opposite behaviour, where the flow close to the bed experiences the bed friction more directly and thus moves slower (slower than the depth-averaged velocity). This means that when calculating the transport flux, the high sediment concentration near the bed is not transported as efficiently as the sediment higher up in the water column. This effect is stronger for flows that experience relatively little mixing. This can also be more important for sand consisting of coarser grains, which experiences stronger settling compared with turbulent mixing.

The swash flow produced by the solitary wave displays a strong backwash compared to the uprush. This backwash is also rather shallow which means that the sediment is distributed over the full water column more uniformly than in a deeper flow. This mixing leads to a relatively uniform sediment distribution. Given that in the Young et al. (2010) case the backwash dominates the overall transport, the uniform approximation performs rather well. The bichromatic waves generally do not produce these long uninterupted backwashes. Furthermore, the transport is not as backwash dominated, and the thicker uprush transports more sediment compared to the solitary wave case. This means that, for the bichromatic case, the sediment cannot mix over the whole water column, and thus the uniform approximation is less applicable.

The proposed mechanism above is rather simple and builds upon concepts that are already used in certain depth-averaged models such as the sediment adaptation time in the approach of Galappatti and Vreugdenhil (1985). Therefore, one could possibly account for the nonuniformity in the sediment flux in a similar way. This does not mean that pre-suspended sediment or wave-swash interactions are unimportant for sediment transport. However, the vertical nonuniformity of the suspended flux does not necessarily stem from such processes.

5.2.3 Implications for swash transport modelling

Masselink and Puleo (2006) highlight the distinction between net transport rates and the uprush and backwash transport. Measurements have shown that the flux of net transport, uprush transport minus backwash transport, can be orders of magnitude smaller than the individual uprush and backwash transport fluxes. This has important implications for intraswash models. If one aims to apply models to longer time-series than only a handful of waves, it is important to not only predict the instantaneous transport rates well. Tiny systematic differences between the uprush and backwash transport fluxes compound over time into a large net transport.

In this light, the significance of the results above become apparent. Although, in many locations the results show that the depth-averaged flux approximation is a

good approximation, the small errors present due to a uniform assumption become relevant over longer time-scales. This is especially true close to equilibrium beach profiles, where net transport rates are nearly zero but instantaneous transport rates are still high. For this reason, the inclusion of the vertical dependence of sediment transport could be especially important for long-term modelling.

Previous studies have attempted to differentiate the flow and transport in the backwash and uprush by modifying the friction coefficient between the two phases (Masselink et al., 2005). The downside of this approach is that it is not immediately clear which processes are responsible, and that it differentiates the swash into being strictly in an uprush or backwash state. Vertical structures could provide the modeller with such physics-based parameters to tune the uprush and backwash transport respectively. For instance, including effects of wave-breaking turbulence provides the modeller with a physics-based process that predominantly affects the uprush. This opens the door to tuning not only instantaneous fluxes, but also net fluxes using a physics-based approach.

5.3 Porous bed effects

An important characteristic of the swash zone is its interaction with the groundwater system. For beaches consisting of coarser material such as gravel, the exchange of water through the beach is important to consider due to its porosity (McCall et al., 2014). This is less important for sandy beaches where the much lower hydraulic conductivity limits the amount of water exchange (Masselink and Li, 2001). Instead, pore-pressure effects take over. This section discusses how the impact of pore-pressures on sediment can be modelled using depth-resolving models, and how models can be used to analyse pore-pressure behaviour in more detail.

5.3.1 Two opposing effects

This thesis considers two processes, namely the change of the boundary layer shape and the effective particle weight. The former effect happens when small infiltration or exfiltration fluxes make the boundary layer thinner or thicker. This makes the velocity gradient steeper or milder affecting the shear stress, but also influences other flow characteristics such as turbulent fluctuations (Lohmann et al., 2006). The effective particle weight refers to the force resulting from integrating a vertical pressure gradient over the particle surface (see e.g. Schippers et al., 2017). As discussed in Chapter 4, these two effects result in opposing tendencies for sediment transport. The boundary layer effect increases the shear stress during the uprush and decreases the shear stress during the backwash. The effective weight has the opposite effect. As such understanding the relative balance between these two processes is crucial.

Depth-resolving models can here provide a good tool to investigate this. One can use a similar model as in this thesis, which only models the flow above the surface. With this approach the effects of pore-pressures can for instance be parametrised

in the Shields parameter using the approaches of Nielsen et al. (2001) and Conley and Inman (1994). To make this work the CFD, model needs to be coupled to a model for pore-pressure gradients at the bed, such as the model presented in Baldock et al. (2001).

A different approach is to model the 2DV subsurface flow explicitly. This was done by Schippers et al. (2017), who coupled a RANS model to a Darcy flow model in the bed. Alternatively, one can include the porosity in the RANS equations directly, as for instance done by Torres-Freyermuth et al. (2013). Finally, the aforementioned two-phase Euler-Euler models also provide a method for modelling these effects in a 2DV setting.

The two opposing effects can over longer time-scales influence the net sediment transport in the swash. This is important to consider in the context of wave-averaged net transport. Similar to the discussion in Section 5.2.3, a small change in instantaneous transport can have large ramifications for long term net transport. An important distinction is that pressure gradients are difficult to model without relying on measurements due to the large influence of the hydraulic conductivity, which can vary greatly for similar sediment grain sizes (see the discussion in Section 4.4.4).

5.3.2 Nonhydrostatic effects

Chapter 4 used an analytical model to calculate pore pressure gradients in the bed. This model relies on a pressure time-series at the bed interface. These pressures were calculated by assuming hydrostatic pressure, and thus were based on only the local water depth. The results demonstrate that this works well on the scale of individual waves, however, for processes happening on shorter time and spatial scales this might not be sufficient. Examples of such a processes are the wave-breaking induced coherent vortices discussed by Sumer et al. (2013) or flow phenomena related to wave-swash interactions. Both these phenomena influence sediment transport.

There are different methods to investigate these processes. In an experimental setting this could possibly be done by measuring the pressures at the bed as well. However, as explained in Chapter 3, a moving bed makes such experiments very difficult due to changing morphologies and scour around instruments. Instead, CFD models can provide a detailed description of the flow near and in the bed.

Chapter 6

Conclusions and Recommendations

6.1 Conclusions

To what extent can a depth-resolving model predict intra-swash sand transport and morphodynamics and which processes are necessary to account for?

The model in this thesis is based on the depth-resolving morphodynamic model *sediMorph* by Jacobsen et al. (2014), which originally was designed for modelling breaker bar morphodynamics. In order to apply the model to the swash zone, a number of modifications were necessary. First, Chapter 2 shows the need for numerically stable calculations of the reference concentration. Furthermore, the isoAdvector model improves hydrodynamic predictions by modelling a sharper interface between air and water compared to the standard MULES model.

Apart from these improvements, two modifications related to the physics needed to be made. First, the rising behaviour of small bubbles cannot be modelled using a standard 2DV implementation. In the swash zone, this means that bubbles linger in the flow for too long, thereby decreasing the friction between the flow and the bed. This leads to overpredicted runup lengths, and underpredicted sediment transport, especially in the uprush. When these bubbles are artificially removed in the flow, the uprush transport improves considerably. Furthermore, the predictions of the runup are improved significantly. Second, the impact of the Wilcox (2006) limiter for the $k-\omega$ turbulence model was investigated. This limiter leads to decreased wave-breaking induced turbulence. When this limiter was applied, time-series of computed sediment concentration show unphysical spiky behaviour, and a general underprediction of the amount of sediment in suspension. This shows that sediment is not kept in suspension correctly if the important mobilising effects of turbulence are not accounted for.

The final model predicts water depths and velocities well. Sediment transport and morphodynamics remain more challenging. The model correctly predicted erosion for the solitary wave case, however, even with the modifications mentioned above the modelled location of deposition lies slightly onshore of the measured location. The location of the erosion agrees well with the experiment. The results for the bichromatic waves show a similar trend. Again, the hydrodynamics are predicted well but the reproduction of the measured sediment concentrations are worse. The final model, including the modifications mentioned above, captures some of the qualitative characteristics of the sediment concentration time-series. For this qualitative match both the bubbles needed to be removed and the wave-breaking turbulence needed to be present by switching of the limiter.

How do depth-dependent processes in the water column determine sediment transport in the swash zone?

The vertical nonuniformities in flow velocity and sediment concentration have a large impact on the overall sediment transport flux. If one does not take these

into account, one can observe large overpredictions of the sediment flux (up to 50%, see Figure 3.11. These vertical nonuniformities are most important in the swash zone around the initial still water line. The strong vertical flow (and as such strong vertical mixing) in the wave-breaking region means that the approximation of a vertically uniform sediment flux holds quite well. This means that, even if depth-averaged models can per definition not model such vertical flow velocities, a depth-averaged approach to sediment transport could still predict reasonable sediment fluxes in this region.

An important process influencing the vertical structures in both the flow and sediment concentrations is turbulence. This re-emphasizes the importance of including a description of turbulence in swash zone models. This is especially important in the uprush.

How do pore pressure gradients behave in the swash zone, and how can they influence sediment mobility?

Vertical pore pressures at the bed interface can have a significant impact on the Shields parameter. These pressure gradients arise from the incoming waves and bores that induce a pressure gradient in the bed. Combined with the elasticity of the pore water and the bed material, the pressure signal attenuates and shifts. This becomes stronger at deeper positions in the bed. This attenuation can be modelled well by an analytical model that calculates the attenuation and shifting for each frequency component. Furthermore, the model shows that at different locations around the initial water line, the strength of the shifting and attenuation varies. This can be attributed to variations in bed saturation and bed packing.

The net effect on sediment mobility was investigated through the concept of effective sediment weight. This is the difference in weight sediment particles experience when a pressure gradient is applied over them. During uprush, the gradients increased the sediment weight, thereby decreasing the sediment mobility. During the backwash, the opposite effect happens.

Synthesis

The goal of the thesis is to improve understanding of depth-dependent processes in the swash zone and their impact on sediment transport and morphodynamics. This is achieved using a combination of detailed numerical modelling (Chapters 2 and 3) and laboratory experiments (Chapter 4). The laboratory experiments (Chapter 4) have shown that vertical pressure gradients occur within the bed of sandy beaches. These pressure gradients influence the mobility of sediment grains in the bed. We showed that an analytical model was successful in modelling the pressure gradients at different locations around the initial shoreline.

The numerical investigations have also led to multiple new insights. For instance, turbulence induced in the wave breaking process is crucial in understanding the sediment concentrations in the uprush. Furthermore, we showed that 2DV models that use the VoF method for discriminating between air and water need to take

care in modelling air bubbles. These bubbles can linger close to the bed which leads to faulty bed shear stress and sediment concentration predictions. Furthermore, the numerical studies have led to improvements for detailed CFD models, such as a stabilised implementation of boundary conditions for high Peclet numbers. Finally, the final model shows that vertical structures in the cross-shore sediment flux are especially important, and that this is especially the case in the swash zone compared with the surf zone.

6.2 Recommendations

The recommendations below are, apart from the work presented in this thesis, also based on presentations by and discussions with other researchers. The recommendations are organised in different subgroups, namely the development of detailed models, other research applications and the application of detailed models in practice.

6.2.1 Depth-resolving model development

Define standards and best practices for detailed wave models

In the domain of coastal research, there is as of yet no agreed upon best practice for modelling hydrodynamics. The study by Larsen et al. (2019), on the effect that different numerical settings have on wave propagation modelled by a RANS model, shows that choices regarding discretisation and timestep size had a big impact on modelled flow velocities and surface elevations. Similarly, the many different methods of dealing with the free surface interface as discussed in Chapter 3 mean that a modeller has even more decisions to make are setting up a model. The review paper of Briganti et al. (2016) showed some examples of models for the swash zone of different complexities, however, this review did not touch upon the subtleties involved in detailed modelling using, for instance, the RANS and LES approaches. In the field of airflow simulations in and around buildings, Blocken (2018) provided a comprehensive review of the use of CFD approaches. He also argues for the importance of best practice guidelines for using these models. As was put forth over four decades ago by Leonard (1979), bad numerics and knowledge thereof can greatly inhibit research into flow physics. Therefore, a thorough review and a set of guidelines for the use of detailed CFD for waves would be very beneficial and enable better use of CFD in research.

Investigate the effect of choice of turbulence models on sediment transport and morphodynamics

There are different studies that investigate the accuracy of turbulence models and modifications thereof in the surf and swash zones (Brown et al., 2016; Devolder et al., 2018; Larsen and Fuhrman, 2018; Li et al., 2022). These studies typically use measured velocity profiles, be it instantaneous or time-averaged, to determine

which turbulence model achieves best performance. However, when the end goal of the model relates to sediment dynamics and morphodynamics instead of purely hydrodynamics, the same turbulence models may not produce the best morphodynamic results. This could be explained by different aspects of turbulence being important for the undertow or sediment transport respectively. For instance, small differences in the bed shear stress due to turbulence can lead to large differences in local sediment concentrations, whereas this could only have a mild influence on the flow locally. For this reason, it is valuable to investigate how different turbulence models affect predictions of morphodynamics.

6.2.2 Research applications

Parametrise the effect of turbulence on sediment transport for depth-averaged models

This thesis demonstrates the importance of accounting for the mobilising effect of wave-breaking induced turbulence during uprush. As discussed in that chapter, this has already been investigated in the context of depth-averaged models in studies by Alsina et al. (2009), Jongedijk (2017) and Zhu and Dodd (2020). In these studies, accounting for bore-induced turbulence increased the onshore transport significantly. However, still many depth-averaged models do not readily include the possibility to model turbulence, as well as its effect on sediment. Although modelling turbulence can be complex, it also provides an opportunity to provide a physics-based alternative to the procedure of tuning the sediment transport differently for the uprush and backwash as shown in Masselink et al. (2005).

Parametrise vertical nonuniformities in sediment transport formulations for depth-averaged models

This thesis shows that velocities and sediment concentrations can vary strongly over the whole water column. Therefore, Chapter 3 introduces the effective transport velocity U_c. This is only one way one can envision to account for vertical nonuniformities. The strength in an approach like this ultimately lies in the ability to model the effective velocity using a physics based model, preferably based on information a depth-averaged model can provide. To do this, accurate predictions of turbulence (or at the very least eddy viscosity and sediment mixing) are necessary. The depth-resolving model can be used to produce more data under different wave and beach conditions, from which process-based transport formulations accounting for nonuniformities can be developed.

Investigate effect of pore pressures on sediment mobility in detailed morphodynamic models

The implementation of the depth-resolving model in this thesis does not account for effects pertaining to infiltration, or any other exchange of water and momentum through the bed interface. Chapter 4 in this thesis, together with previous research

by for instance Sumer et al. (2013) and Stark et al. (2022), show that this can be very important for understanding sediment transport. The depth-resolving model could be extended by an analytical model similar to the one presented in Chapter 4. However, one could also couple a more detailed porous flow model as for instance done by Schippers et al. (2017). This more detailed approach would also provide the possibility to study the effect of the groundwater table on sediment transport. This has previously been done mostly using observations of field studies (Horn, 2002), but this can also be done using detailed depth-resolving models.

Investigate wave-swash interactions numerically

Since the type of wave-swash interaction can have a large influence on sediment transport (Cáceres and Alsina, 2012), it is important to better understand their dynamics. For instance, Dionísio António et al. (2022) found that the beach shape has a large influence on the type and strength of these interactions. Detailed numerical models can play an important role in two ways. First, they can be used to understand when different interactions happen. As mentioned, many studies characterise these interactions qualitatively, however, in reality the interactions present a spectrum. Numerical models provide a cheaper way of investigating this a broader parameter space compared with experiments. Furthermore, detailed models can give more insight into how these interactions influence sediment fluxes, and how the beach shape influences the type and strength of interactions.

Equilibria, and the beach as a dynamical system

There exist different approaches for modelling swash morphodynamics on longer, practical timescales (Chen et al., 2023). One way to achieve this is using an equilibrium slope and assuming that the local dynamics evolve towards this equilibrium. Chen et al. (2023) show that this approach can achieve accurate morphodynamical predictions as long as the equilibrium beach profile is known. However, this means that a high quality predictive model of the equilibrium slope is necessary. Currently, no generally applicable model with satisfying performance exists.

Nonlinear systems involving fluid dynamics often exhibit multiple equilibria, bifurcations and sometimes chaos (Dijkstra et al., 2014). Techniques from the studies of dynamic systems have been applied to morphodynamic modelling of marine systems (Schuttelaars and Zitman, 2022), but to the author's knowledge, they have not been used to analyse beach systems. More research on the beach as a dynamical system, aiming to understand its equilibria and asymptotic behaviour, could together with information from detailed numerical models contribute substantially to understanding the beach system as a whole.

6.2.3 Practical model applications

Model effects of different nourishment scenarios using detailed morphological models

Around the world, beaches are being nourished to mitigate erosion. The model has previously been applied to investigate different possible nourishments around a bar (Jacobsen and Fredsoe, 2014a). Similar studies can now be done for nourishments on the beach. Although CFD is costly, it can provide detailed insight into flow processes occurring at specific scenarios.

Investigate effects of structures on or near the beach using detailed morphological models

One of the big benefits of the finite volume method is the flexibility one has in the geometry and mesh. This makes it relatively straightforward to investigate hard structures around sandy beaches. As previously mentioned, scour around monopiles is already being investigated with a very similar model (Li et al., 2019). The model can also be applied to investigate how protective measures such as seawalls interact with the beach morphodynamics.

Bibliography

Aagaard, T., Brinkkemper, J., Christensen, D. F., Hughes, M. G., & Ruessink, G. (2021). Surf Zone Turbulence and Suspended Sediment Dynamics— A Review. *Journal of Marine Science and Engineering*, *9*(11), 1300, https://doi.org/10.3390/jmse9111300.

Alsina, J. M., Falchetti, S., & Baldock, T. E. (2009). Measurements and modelling of the advection of suspended sediment in the swash zone by solitary waves. *Coastal Engineering*, *56*(5-6), 621–631, https://doi.org/10.1016/j.coastaleng.2009.01.007.

Alsina, J. M., Van der Zanden, J., Cáceres, I., & Ribberink, J. S. (2018). The influence of wave groups and wave-swash interactions on sediment transport and bed evolution in the swash zone. *Coastal Engineering*, *140*, 23–42, https://doi.org/10.1016/j.coastaleng.2018.06.005.

Anderson, W. P. (2015). Coastal Groundwater. *Coastal Environments and Global Change*, (pp. 128–148)., https://doi.org/10.1002/9781119117261.ch6.

Bakhtyar, R., Barry, D. A., Yeganeh-Bakhtiary, A., Li, L., Parlange, J. Y., & Sander, G. C. (2010). Numerical simulation of two-phase flow for sediment transport in the inner-surf and swash zones. *Advances in Water Resources*, *33*(3), 277–290, https://doi.org/10.1016/j.advwatres.2009.12.004.

Bakhtyar, R., Brovelli, A., Barry, D. A., & Li, L. (2011). Wave-induced water table fluctuations, sediment transport and beach profile change: Modeling and comparison with large-scale laboratory experiments. *Coastal Engineering*, *58*(1), 103–118, https://doi.org/10.1016/j.coastaleng.2010.08.004.

Bakhtyar, R., Ghaheri, A., Yeganeh-Bakhtiary, A., & Barry, D. A. (2009). Process-based model for nearshore hydrodynamics, sediment transport and morphological evolution in the surf and swash zones. *Applied Ocean Research*, *31*(1), 44–56, https://doi.org/10.1016/j.apor.2009.05.002.

Baldock, T. E., Baird, A. J., Horn, D. P., & Mason, T. (2001). Measurements and modeling of swash-induced pressure gradients in the surface layers of a sand beach. *Journal of Geophysical Research: Oceans*, *106*(C2), 2653–2666, https://doi.org/10.1029/1999jc000170.

Baldock, T. E. & Holmes, P. (1998). Seepage effects on sediment transport by waves and currents. In *Proceedings of the Coastal Engineering Conference*, volume 3 (pp. 3601–3614). Reston, VA: American Society of Civil Engineers. ISSN: 08938717.

Baldock, T. E. & Nielsen, P. (2010). Discussion of "Effect of Seepage-Induced Nonhydrostatic Pressure Distribution on Bed-Load Transport and Bed Morphodynamics" by Simona Francalanci, Gary Parker, and Luca Solari. *Journal of Hydraulic Engineering*, *136*(1), 77–79, https://doi.org/10.1061/(asce)hy.1943-7900.0000015.

Biot, M. A. (1941). General theory of three-dimensional consolidation. *Journal of Applied Physics*, *12*(2), 155–164, https://doi.org/10.1063/1.1712886.

Blenkinsopp, C. E., Turner, I. L., Masselink, G., & Russell, P. E. (2011). Swash zone sediment fluxes: Field observations. *Coastal Engineering*, *58*(1), 28–44, https://doi.org/10.1016/j.coastaleng.2010.08.002.

Blocken, B. (2018). LES over RANS in building simulation for outdoor and indoor applications: A foregone conclusion? *Building Simulation*, *11*(5), 821–870, https://doi.org/10.1007/s12273-018-0459-3.

Bosboom, J., Mol, M., Reniers, A. J. H. M., Stive, M. J. F., & de Valk, C. F. (2020). Optimal sediment transport for morphodynamic model validation. *Coastal Engineering*, *158*, 103662, https://doi.org/10.1016/j.coastaleng.2020.103662.

Boudet, J. (2011). Finite volume methods. In *Computational Fluid Dynamics* (pp. 1–24). Berlin, Heidelberg: Springer Berlin Heidelberg.

Boyer, F., Guazzelli, E., & Pouliquen, O. (2011). Unifying suspension and granular rheology. *Physical Review Letters*, *107*(18), 188301, https://doi.org/10.1103/PhysRevLett.107.188301.

Briganti, R., Dodd, N., Incelli, G., & Kikkert, G. (2018). Numerical modelling of the flow and bed evolution of a single bore-driven swash event on a coarse sand beach. *Coastal Engineering*, *142*(October), 62–76, https://doi.org/10.1016/j.coastaleng.2018.09.006.

Briganti, R., Torres-Freyermuth, A., Baldock, T. E., Brocchini, M., Dodd, N., Hsu, T. J., Jiang, Z., Kim, Y., Pintado-Patiño, J. C., & Postacchini, M. (2016). Advances in numerical modelling of swash zone dynamics. *Coastal Engineering*, *115*(May), 26–41, https://doi.org/10.1016/j.coastaleng.2016.05.001.

Brown, S. A., Greaves, D. M., Magar, V., & Conley, D. C. (2016). Evaluation of turbulence closure models under spilling and plunging breakers in the surf zone. *Coastal Engineering*, *114*, 177–193, https://doi.org/10.1016/j.coastaleng.2016.04.002.

Butt, T., Russell, P., Puleo, J., Miles, J., & Masselink, G. (2004). The influence of bore turbulence on sediment transport in the swash and inner surf zones. *Continental Shelf Research*, *24*(7-8), 757–771, https://doi.org/10.1016/j.csr.2004.02.002.

Castro, A. M., Li, J., & Carrica, P. M. (2016). A mechanistic model of bubble entrainment in turbulent free surface flows. *International Journal of Multiphase Flow*, *86*, 35–55, https://doi.org/10.1016/j.ijmultiphaseflow.2016.07.005.

Cebeci, T. & Chang, K. C. (1978). Calculation of incompressible rough-wall boundary-layer flows. *AIAA Journal*, *16*(7), 740–746, https://doi.org/10.2514/3.7571.

Chappelear, J. E. (1962). Shallow-water waves. *Journal of Geophysical Research (1896-1977)*, *67*(12), 4693–4704, https://doi.org/10.1029/JZ067i012p04693.

Chauchat, J., Cheng, Z., Nagel, T., Bonamy, C., & Hsu, T. J. (2017). SedFoam-2.0: A 3-D two-phase flow numerical model for sediment transport. *Geoscientific Model Development*, *10*(12), 4367–4392, https://doi.org/10.5194/gmd-10-4367-2017.

Chen, B. T., Kikkert, G. A., Pokrajac, D., & Dai, H. J. (2016). Experimental study of bore-driven swash-swash interactions on an impermeable rough slope. *Coastal Engineering*, *108*, 10–24, https://doi.org/10.1016/j.coastaleng.2015.10.010.

Chen, W., Van der Werf, J. J., & Hulscher, S. J. M. H. (2023). A review of practical models of sand transport in the swash zone. *Earth-Science Reviews*, *238*, 104355, https://doi.org/10.1016/j.earscirev.2023.104355.

Chen, W., Van Gent, M. R. A., Warmink, J. J., & Hulscher, S. J. M. H. (2020). The influence of a berm and roughness on the wave overtopping at dikes. *Coastal Engineering*, *156*, https://doi.org/10.1016/j.coastaleng.2019.103613.

Chen, W., Warmink, J. J., Van Gent, M. R. A., & Hulscher, S. J. M. H. (2022). Numerical investigation of the effects of roughness, a berm and oblique waves on wave overtopping processes at dikes. *Applied Ocean Research*, *118*, 102971, https://doi.org/10.1016/j.apor.2021.102971.

Cheng, N. S. & Chiew, Y. M. (1999). Incipient sediment motion with upward seepage. *Journal of Hydraulic Research*, *37*(5), 665–681, https://doi.org/10.1080/00221689909498522.

Cheng, Z., Hsu, T. J., & Calantoni, J. (2017). SedFoam: A multi-dimensional Eulerian two-phase model for sediment transport and its application to momentary bed failure. *Coastal Engineering*, *119*, 32–50, https://doi.org/10.1016/j.coastaleng.2016.08.007.

Christoffersen, G. (2019). *Laboratory scale CFD simulation of wave breaking and sediment transport*. PhD thesis, DTU, Copenhagen.

Coakley, T. J. (1983). Turbulence modeling methods for the compressible Navier-Stokes equations. https://doi.org/10.2514/6.1983-1693.

Conley, D. C. & Inman, D. L. (1994). Ventilated oscillatory boundary layers. *Journal of Fluid Mechanics*, *273*(C6), 261–284, https://doi.org/10.1017/S002211209400193X.

Cáceres, I. & Alsina, J. M. (2012). A detailed, event-by-event analysis of suspended sediment concentration in the swash zone. *Continental Shelf Research*, *41*, 61–76, https://doi.org/10.1016/j.csr.2012.04.004.

Dalrymple, R. A. & Rogers, B. D. (2006). Numerical modeling of water waves with the SPH method. *Coastal Engineering*, *53*(2-3), 141–147, https://doi.org/10.1016/j.coastaleng.2005.10.004.

Darwish, M. S. & Moukalled, F. (2003). TVD schemes for unstructured grids. *International Journal of Heat and Mass Transfer*, *46*(4), 599–611, https://doi.org/10.1016/S0017-9310(02)00330-7.

Deigaard, R., Fredsøe, J., & Hedegaard, I. B. (1986). Suspended Sediment in the Surf Zone. *Journal of Waterway, Port, Coastal, and Ocean Engineering*, *112*(1), 115–128, https://doi.org/10.1061/(asce)0733-950x(1986)112:1(115).

Delisle, M. P. C., Kim, Y., Mieras, R. S., & Gallien, T. W. (2022). Numerical investigation of sheet flow driven by a near-breaking transient wave using SedFoam. *European Journal of Mechanics, B/Fluids*, *96*, 51–64, https://doi.org/10.1016/j.euromechflu.2022.07.002.

Derakhti, M. & Kirby, J. T. (2014). Bubble entrainment and liquid-bubble interaction under unsteady breaking waves. *Journal of Fluid Mechanics*, *761*, 464–506, https://doi.org/10.1017/jfm.2014.637.

Deshpande, S. S., Anumolu, L., & Trujillo, M. F. (2012). Evaluating the performance of the two-phase flow solver interFoam. *Computational Science and Discovery*, *5*(1), 14016, https://doi.org/10.1088/1749-4699/5/1/014016.

Desombre, J., Morichon, D., & Mory, M. (2013). RANS v 2-f simulation of a swash event: Detailed flow structure. *Coastal Engineering*, *71*, 1–12, https://doi.org/10.1016/j.coastaleng.2012.07.001.

Devolder, B., Troch, P., & Rauwoens, P. (2018). Performance of a buoyancy-modified k-ω and k-ω SST turbulence model for simulating wave breaking under regular waves using OpenFOAM®. *Coastal Engineering*, *138*(August 2017), 49–65, https://doi.org/10.1016/j.coastaleng.2018.04.011.

Dijkstra, H. A., Wubs, F. W., Cliffe, A. K., Doedel, E., Dragomirescu, I. F., Eckhardt, B., Gelfgat, A. Y., Hazel, A. L., Lucarini, V., Salinger, A. G., Phipps, E. T., Juan, S. U., Schuttelaars, H., Tuckerman, L. S., & Thiele, U. (2014). Numerical bifurcation methods and their application to fluid dynamics: Analysis beyond simulation. *Communications in Computational Physics*, *15*(1), 1–45, https://doi.org/10.4208/cicp.240912.180613a.

Dionísio António, S., Van der Werf, J. J., Horstman, E. M., Cáceres, I., Alsina, J. M., Van der Zanden, J., & Hulscher, S. J. M. H. (2022). Influence of beach slope on morphological changes and sediment transport under irregular waves (submitted).

Engelund, F. & Fredsoe, J. (1976). A sediment transport model for straight alluvial channels. *Hydrology Research*, *7*(5), 293–306, https://doi.org/10.2166/nh.1976.0019.

Engsig-Karup, A. P., Bingham, H. B., & Lindberg, O. (2009). An efficient flexible-order model for 3D nonlinear water waves. *Journal of Computational Physics*, *228*(6), 2100–2118, https://doi.org/10.1016/j.jcp.2008.11.028.

Erikson, L., Larson, M., & Hanson, H. (2005). Prediction of swash motion and run-up including the effects of swash interaction. *Coastal Engineering*, *52*(3), 285–302, https://doi.org/10.1016/j.coastaleng.2004.12.001.

Fernandez-Mora, A., Ribberink, J. S., Van der Zanden, J., Van der Werf, J. J., & Jacobsen, N. G. (2017). RANS-VOF modeling of hydrodynamics and sand transport under full-scale non-breaking and breaking waves. In P. Lynett (Ed.), *Coastal Engineering Proceedings*, volume 1 (pp.29). United States: Coastal Engineering Research Council. Issue: 35 ISSN: 0589-087X.

Francalanci, S., Parker, G., & Solari, L. (2008). Effect of Seepage-Induced Nonhydrostatic Pressure Distribution on Bed-Load Transport and Bed Morphodynamics. *Journal of Hydraulic Engineering*, *134*(4), 378–389, https://doi.org/10.1061/(asce)0733-9429(2008)134:4(378).

Francalanci, S., Parker, G., & Solari, L. (2010). Closure to "Effect of Seepage-Induced Nonhydrostatic Pressure Distribution on Bed-Load Transport and Bed Morphodynamics" by Simona Francalanci, Gary Parker, and Luca Solari. *Journal of Hydraulic Engineering*, *136*(1), 79–82, https://doi.org/10.1061/(asce)hy.1943-7900.0000160.

Fredsøe, J. & Deigaard, R. (1992). *Mechanics of Coastal Sediment Transport*, volume 3. WORLD SCIENTIFIC. Series Title: Advanced Series on Ocean Engineering Publication Title: Coastal Engineering Issue: 1-2 ISSN: 03783839.

Fredsøe, J., Sumer, B. M., Kozakiewicz, A., Chua, L. H., & Deigaard, R. (2003). Effect of externally generated turbulence on wave boundary layer. *Coastal Engineering*, *49*(3), 155–183, https://doi.org/10.1016/S0378-3839(03)00032-2.

Fuhrman, D. R., Dixen, M., & Jacobsen, N. G. (2010). Physically-consistent wall boundary conditions for the k-turbulence model. *Journal of Hydraulic Research*, *48*(6), 793–800, https://doi.org/10.1080/00221686.2010.531100.

Galappatti, G. & Vreugdenhil, C. B. (1985). Un modèle de transport solide en suspension intégré sur la verticale. *Journal of Hydraulic Research*, *23*(4), 359–377, https://doi.org/10.1080/00221688509499345.

García-Maribona, J., Lara, J. L., Maza, M., & Losada, I. J. (2021). An efficient RANS numerical model for cross-shore beach processes under erosive conditions. *Coastal Engineering*, *170*, 103975, https://doi.org/10.1016/j.coastaleng.2021.103975.

García-Maribona, J., Lara, J. L., Maza, M., & Losada, I. J. (2022). Analysis of the mechanics of breaker bar generation in cross-shore beach profiles based on numerical modelling. *Coastal Engineering*, *177*, 104172, https://doi.org/10.1016/j.coastaleng.2022.104172.

Guest, T. B. & Hay, A. E. (2017). Vertical structure of pore pressure under surface gravity waves on a steep, megatidal, mixed sand-gravel-cobble beach. *Journal of Geophysical Research: Oceans*, *122*(1), 153–170, https://doi.org/10.1002/2016JC012257.

Heiss, J. W., Ullman, W. J., & Michael, H. A. (2014). Swash zone moisture dynamics and unsaturated infiltration in two sandy beach aquifers. *Estuarine, Coastal and Shelf Science*, *143*, 20–31, https://doi.org/10.1016/j.ecss.2014.03.015.

Higuera, P., Liu, P. L., Lin, C., Wong, W. Y., & Kao, M. J. (2018). Laboratory-scale swash flows generated by a non-breaking solitary wave on a steep slope. *Journal of Fluid Mechanics*, *847*, 186–227, https://doi.org/10.1017/jfm.2018.321.

Hjelmfelt, A. T. & Lenau, C. W. (1970). Nonequilibrium Transport of Suspended Sediment. *Journal of the Hydraulics Division*, *96*(7), 1567–1586, https://doi.org/10.1061/jyceaj.0002567.

Hjelmfelt, A. T. & Mockros, L. F. (1966). Motion of discrete particles in a turbulent fluid. *Applied Scientific Research*, *16*(1), 149–161, https://doi.org/10.1007/BF00384062.

Horn, D. P. (2002). Beach groundwater dynamics. *Geomorphology*, *48*(1-3), 121–146, https://doi.org/10.1016/S0169-555X(02)00178-2.

Horn, D. P. (2006). Measurements and modelling of beach groundwater flow in the swash-zone: a review. *Continental Shelf Research*, *26*(5), 622–652, https://doi.org/10.1016/j.csr.2006.02.001.

Hsu, J. R. C. & Jeng, D. S. (1994). Wave-induced soil response in an unsaturated anisotropic seabed of finite thickness. *International Journal for Numerical and Analytical Methods in Geomechanics*, *18*(11), 785–807, https://doi.org/10.1002/nag.1610181104.

Hughes, M. G. & Moseley, A. S. (2007). Hydrokinematic regions within the swash zone. *Continental Shelf Research*, *27*(15), 2000–2013, https://doi.org/10.1016/j.csr.2007.04.005.

Incelli, G., Dodd, N., Blenkinsopp, C. E., Zhu, F., & Briganti, R. (2016). Morphodynamical modelling of field-scale swash events. *Coastal Engineering*, *115*, 42–57, https://doi.org/10.1016/j.coastaleng.2015.09.006.

Jacobsen, N. G. (2011). *A Full Hydro- and Morphodynamic Description of Breaker Bar Development*. PhD thesis, Technical University of Denmark. Publication Title: PhD Thesis ISBN: 978-87-90416-64-5.

Jacobsen, N. G. (2015). Mass conservation in computational morphodynamics: Uniform sediment and infinite availability. *International Journal for Numerical Methods in Fluids*, *78*(4), 233–256, https://doi.org/10.1002/fld.4015.

Jacobsen, N. G. & Fredsoe, J. (2014a). Cross-Shore Redistribution of Nourished Sand near a Breaker Bar. *Journal of Waterway, Port, Coastal, and Ocean Engineering*, *140*(2), 125–134, https://doi.org/10.1061/(asce)ww.1943-5460.0000233.

Jacobsen, N. G. & Fredsoe, J. (2014b). Formation and development of a breaker bar under regular waves. Part 2: Sediment transport and morphology. *Coastal Engineering*, *88*, 55–68, https://doi.org/10.1016/j.coastaleng.2014.01.015.

Jacobsen, N. G., Fredsoe, J., & Jensen, J. H. (2014). Formation and development of a breaker bar under regular waves. Part 1: Model description and hydrodynamics. *Coastal Engineering*, *88*, 182–193, https://doi.org/10.1016/j.coastaleng.2013.12.008.

Jacobsen, N. G., Fuhrman, D. R., & Fredsøe, J. (2012). A wave generation toolbox for the open-source CFD library: OpenFoam®. *International Journal for Numerical Methods in Fluids*, *70*(9), 1073–1088, https://doi.org/10.1002/fld.2726.

Jacobsen, N. G., Van Gent, M. R. A., Capel, A., & Borsboom, M. (2018). Numerical prediction of integrated wave loads on crest walls on top of rubble mound structures. *Coastal Engineering*, *142*(October), 110–124, https://doi.org/10.1016/j.coastaleng.2018.10.004.

Jasak, H. (1996). Error Analysis and Estimation for the finite volume method with applications to fluid flows. Thesis submitted for the degree of doctor. Department of Mechanical Engineering, Imperial College of Science. *Imperial College of Science, Technology and Medicine*, *M*(June), 394.

Jongedijk, C. E. (2017). *Improving XBeach non-hydrostatic model predictions of the swash morphodynamics of intermediate-reflective beaches*. PhD thesis, Delft University of Technology, the Netherlands. Publication Title: TU Delft.

Kim, H. & Park, S. (2021). Coupled level-set and volume of fluid (Clsvof) solver for air lubrication method of a flat plate. *Journal of Marine Science and Engineering*, *9*(2), 1–18, https://doi.org/10.3390/jmse9020231.

Kim, Y., Mieras, R. S., Cheng, Z., Anderson, D., Hsu, T. J., Puleo, J. A., & Cox, D. (2019). A numerical study of sheet flow driven by velocity and acceleration skewed near-breaking waves on a sandbar using SedWaveFoam. *Coastal Engineering*, *152*, 103526, https://doi.org/10.1016/j.coastaleng.2019.103526.

Kim, Y., Zhou, Z., Hsu, T. J., & Puleo, J. A. (2017). Large eddy simulation of dam-break-driven swash on a rough-planar beach. *Journal of Geophysical Research: Oceans*, *122*(2), 1274–1296, https://doi.org/10.1002/2016JC012366.

Kranenborg, J. W. M., Campmans, G. H. P., Jacobsen, N. G., Van der Werf, J. J., Reniers, A. J. H. M., & Hulscher, S. J. H. M. (2022). Depth-Resolved Modelling of Intra-Swash Morphodynamics Induced by Solitary Waves. *Journal of Marine Science and Engineering*, *10*(9), 1175, https://doi.org/10.3390/jmse10091175.

Kranenburg, W. M., Hsu, T. J., & Ribberink, J. S. (2014). Two-phase modeling of sheet-flow beneath waves and its dependence on grain size and streaming. *Advances in Water Resources*, *72*, 57–70, https://doi.org/10.1016/j.advwatres.2014.05.008.

Lanckriet, T. & Puleo, J. A. (2015). A semianalytical model for sheet flow layer thickness with application to the swash zone. *Journal of Geophysical Research: Oceans*, *120*(2), 1333–1352, https://doi.org/10.1002/2014JC010378.

Lara, J. L., Ruju, A., & Losada, I. J. (2011). Reynolds averaged Navier-Stokes modelling of long waves induced by a transient wave group on a beach. *Proceedings of the Royal Society A: Mathematical, Physical and Engineering Sciences*, *467*(2129), 1215–1242, https://doi.org/10.1098/rspa.2010.0331.

Larsen, B. E. & Fuhrman, D. R. (2018). On the over-production of turbulence beneath surface waves in Reynolds-averaged Navier-Stokes models. *Journal of Fluid Mechanics*, *853*, 419–460, https://doi.org/10.1017/jfm.2018.577.

Larsen, B. E., Fuhrman, D. R., Baykal, C., & Sumer, B. M. (2017). Tsunami-induced scour around monopile foundations. *Coastal Engineering*, *129*(August), 36–49, https://doi.org/10.1016/j.coastaleng.2017.08.002.

Larsen, B. E., Fuhrman, D. R., & Roenby, J. (2019). Performance of interFoam on the simulation of progressive waves. *Coastal Engineering Journal*, *61*(3), 380–400, https://doi.org/10.1080/21664250.2019.1609713.

Larsen, B. E., Van der A, D. A., Van der Zanden, J., Ruessink, G., & Fuhrman, D. R. (2020). Stabilized RANS simulation of surf zone kinematics and boundary layer processes beneath large-scale plunging waves over a breaker bar. *Ocean Modelling*, *155*, 101705, https://doi.org/10.1016/j.ocemod.2020.101705.

Launder, B. E. & Sharma, B. I. (1974). Application of the energy-dissipation model of turbulence to the calculation of flow near a spinning disc. *Letters in Heat and Mass Transfer*, *1*(2), 131–137, https://doi.org/10.1016/0094-4548(74)90150-7.

Leonard, P. B. (1979). Finite Element Methods for Convection Dominated Flows. *American Society of Mechanical Engineers, Applied Mechanics Division, AMD*, *34*, 1–17.

Lesser, G. R., Roelvink, J. A., Van Kester, J. A. T. M., & Stelling, G. S. (2004). Development and validation of a three-dimensional morphological model. *Coastal Engineering*, *51*(8-9), 883–915, https://doi.org/10.1016/J.COASTALENG.2004.07.014.

Li, J., Fuhrman, D. R., Kong, X., Xie, M., & Yang, Y. (2021). Three-dimensional numerical simulation of wave-induced scour around a pile on a sloping beach. *Ocean Engineering*, *233*, 109174, https://doi.org/10.1016/j.oceaneng.2021.109174.

Li, J., Qi, M., & Fuhrman, D. R. (2019). Numerical modeling of flow and morphology induced by a solitary wave on a sloping beach. *Applied Ocean Research*, *82*(October 2018), 259–273, https://doi.org/10.1016/j.apor.2018.11.007.

Li, Y., Larsen, B. E., & Fuhrman, D. R. (2022). Reynolds stress turbulence modelling of surf zone breaking waves. *Journal of Fluid Mechanics*, *937*, 7, https://doi.org/10.1017/jfm.2022.92.

Li, Y., Ong, M. C., Fuhrman, D. R., & Larsen, B. E. (2020). Numerical investigation of wave-plus-current induced scour beneath two submarine pipelines in tandem. *Coastal Engineering*, *156*, 103619, https://doi.org/10.1016/j.coastaleng.2019.103619.

Lohmann, I. P., Fredsøe, J., Sumer, B. M., & Christensen, E. D. (2006). Large Eddy Simulation of the ventilated wave boundary layer. *Journal of Geophysical Research: Oceans*, *111*(6), C06036, https://doi.org/10.1029/2005JC002946.

Losada, I. J., Lara, J. L., Guanche, R., & Gonzalez-Ondina, J. M. (2008). Numerical analysis of wave overtopping of rubble mound breakwaters. *Coastal Engineering*, *55*(1), 47–62, https://doi.org/10.1016/j.coastaleng.2007.06.003.

Mancini, G., Briganti, R., McCall, R., Dodd, N., & Zhu, F. (2021). Numerical modelling of intra-wave sediment transport on sandy beaches using a non-hydrostatic, wave-resolving model. *Ocean Dynamics*, *71*(1), 1–20, https://doi.org/10.1007/s10236-020-01416-x.

Masselink, G., Evans, D., Hughes, M. G., & Russell, P. (2005). Suspended sediment transport in the swash zone of a dissipative beach. *Marine Geology*, *216*(3), 169–189, https://doi.org/10.1016/j.margeo.2005.02.017.

Masselink, G. & Li, L. (2001). The role of swash infiltration in determining the beachface gradient: A numerical study. *Marine Geology*, *176*(1-4), 139–156, https://doi.org/10.1016/S0025-3227(01)00161-X.

Masselink, G. & Puleo, J. A. (2006). Swash-zone morphodynamics. *Continental Shelf Research*, *26*(5), 661–680, https://doi.org/10.1016/j.csr.2006.01.015.

Masselink, G., Russell, P., Turner, I., & Blenkinsopp, C. (2009). Net sediment transport and morphological change in the swash zone of a high-energy sandy beach from swash event to tidal cycle time scales. *Marine Geology*, *267*(1-2), 18–35, https://doi.org/10.1016/j.margeo.2009.09.003.

Mathieu, A., Cheng, Z., Chauchat, J., Bonamy, C., & Hsu, T. J. (2022). Numerical investigation of unsteady effects in oscillatory sheet flows. *Journal of Fluid Mechanics*, *943*, 7, https://doi.org/10.1017/jfm.2022.405.

McCall, R. T., Masselink, G., Poate, T. G., Roelvink, J. A., & Almeida, L. P. (2015). Modelling the morphodynamics of gravel beaches during storms with XBeach-G. *Coastal Engineering*, *103*, 52–66, https://doi.org/10.1016/j.coastaleng.2015.06.002.

McCall, R. T., Masselink, G., Poate, T. G., Roelvink, J. A., Almeida, L. P., Davidson, M., & Russell, P. E. (2014). Modelling storm hydrodynamics on gravel beaches with XBeach-G. *Coastal Engineering*, *91*, 231–250, https://doi.org/10.1016/j.coastaleng.2014.06.007.

Mory, M., Abadie, S., Mauriet, S., & Lubin, P. (2011). Run-up flow of a collapsing bore over a beach. *European Journal of Mechanics, B/Fluids*, *30*(6), 565–576, https://doi.org/10.1016/j.euromechflu.2010.11.005.

Nielsen, P., Robert, S., Møller-Christiansen, B., & Oliva, P. (2001). Infiltration effects on sediment mobility under waves. *Coastal Engineering*, *42*(2), 105–114, https://doi.org/10.1016/S0378-3839(00)00051-X.

Niemann, S. L. (2004). *Modelling of Sand Dunes in Steady and Tidal Flow*. Kgs. Lyngby, Denmark: Technical University of Denmark.

Paulsen, B. T., Bredmose, H., & Bingham, H. B. (2014). An efficient domain decomposition strategy for wave loads on surface piercing circular cylinders. *Coastal Engineering*, *86*, 57–76, https://doi.org/10.1016/j.coastaleng.2014.01.006.

Pedrozo-Acuña, A., Simmonds, D. J., & Reeve, D. E. (2008). Wave-impact characteristics of plunging breakers acting on gravel beaches. *Marine Geology*, *253*(1-2), 26–35, https://doi.org/10.1016/j.margeo.2008.04.013.

Pintado-Patiño, J. C., Torres-Freyermuth, A., Puleo, J. A., & Pokrajac, D. (2015). On the role of infiltration and exfiltration in swash zone boundary layer dynamics. *Journal of Geophysical Research: Oceans*, *120*(9), 6329–6350, https://doi.org/10.1002/2015JC010806.

Pope, S. B. (2000). *Turbulent Flows*, volume 21. Cambridge University Press. Publication Title: European Journal of Mechanics - B/Fluids Issue: 1.

Pourteimouri, P., Campmans, G. H. P., Wijnberg, K. M., & Hulscher, S. J. M. H. (2022). A numerical study on the impact of building dimensions on airflow patterns and bed morphology around buildings at the beach. *Journal of Marine Science and Engineering*, *10*(1), 13, https://doi.org/10.3390/jmse10010013.

Pritchard, D. & Hogg, A. J. (2003). Suspended sediment transport under seiches in circular and elliptical basins. *Coastal Engineering*, *49*(1-2), 43–70, https://doi.org/10.1016/S0378-3839(03)00046-2.

Puleo, J. A., Beach, R. A., Holman, R. A., & Allen, J. S. (2000). Swash zone sediment suspension and transport and the importance of bore-generated turbulence. *Journal of Geophysical Research: Oceans*, *105*(C7), 17021–17044, https://doi.org/10.1029/2000jc900024.

Puleo, J. A. & Torres-Freyermuth, A. (2016). The second international workshop on swash-zone processes. *Coastal Engineering*, *115*, 1–7, https://doi.org/10.1016/j.coastaleng.2015.09.007.

Quezada, M., Tamburrino, A., & Niño, Y. (2019). Numerical study of the hydrodynamics of waves and currents and their effects in pier scouring. *Water (Switzerland)*, *11*(11), 2256, https://doi.org/10.3390/w11112256.

Qwist, J. R. K. & Christensen, E. D. (2023). Development and implementation of a Direct Surface Description method for free surface flows in OpenFOAM. *Coastal Engineering*, *179*, 104227, https://doi.org/10.1016/j.coastaleng.2022.104227.

Raubenheimer, B., Elgar, S., & Guza, R. T. (1998). Estimating Wave Heights from Pressure Measured in Sand Bed. *Journal of Waterway, Port, Coastal, and Ocean Engineering*, *124*(3), 151–154, https://doi.org/10.1061/(asce)0733-950x(1998)124:3(151).

Reniers, A. J. H. M., Gallagher, E. L., MacMahan, J. H., Brown, J. A., Van Rooijen, A. A., Van Thiel De Vries, J. S. M., & Van Prooijen, B. C. (2013). Observations and modeling of steep-beach grain-size variability. *Journal of Geophysical Research: Oceans*, *118*(2), 577–591, https://doi.org/10.1029/2012JC008073.

Roenby, J., Bredmose, H., & Jasak, H. (2016). A computational method for sharp interface advection. *Royal Society Open Science*, *3*(11), 160405, https://doi.org/10.1098/rsos.160405.

Roulund, A., Sumer, B. M., Fredsøe, J., & Michelsen, J. (2005). Numerical and experimental investigation of flow and scour around a circular pile. *Journal of Fluid Mechanics*, *534*, 351–401, https://doi.org/10.1017/S0022112005004507.

Ruffini, G., Briganti, R., Alsina, J. M., Brocchini, M., Dodd, N., & McCall, R. (2020). Numerical Modeling of Flow and Bed Evolution of Bichromatic Wave Groups on an Intermediate Beach Using Nonhydrostatic XBeach. *Journal of Waterway, Port, Coastal, and Ocean Engineering*, *146*(1), 04019034, https://doi.org/10.1061/(asce)ww.1943-5460.0000530.

Rusche, H. (2002). Computational Fluid Dynamics of Dispersed Two-Phase Flows at High Phase Fractions. *PhD Thesis*, *1*(December), 335.

Sanchez-Arcilla, A. & Caceres, I. (2018). An analysis of nearshore profile and bar development under large scale erosive and accretive waves. *Journal of Hydraulic Research*, *56*(2), 231–244, https://doi.org/10.1080/00221686.2017.1315748.

Schippers, M. M. A., Jacobsen, N. G., Soupy Dalyander, P., Nelson, T., & McCall, R. (2017). Incipient motion of sand-oil agglomerates. *Coastal Dynamics*, *1*(011), 1290–1301.

Schuttelaars, H. M. & Zitman, T. J. (2022). Morphodynamic Modelling in Marine Environments: Model Formulation and Solution Techniques. In *The Mathematics of Marine Modelling* (pp. 243–285). Springer, Cham.

Shi, F., Kirby, J. T., & Ma, G. (2010). Modeling quiescent phase transport of air bubbles induced by breaking waves. *Ocean Modelling*, *35*(1-2), 105–117, https://doi.org/10.1016/j.ocemod.2010.07.002.

Shih, T. H., Zhu, J., & Lumley, J. L. (1996). Calculation of wall-bounded complex flows and free shear flows. *International Journal for Numerical Methods in Fluids*, *23*(11), 1133–1144, https://doi.org/10.1002/(SICI)1097-0363(19961215)23:11<1133::AID-FLD456>3.0.CO;2-A.

Soulsby, R. (1997). *Dynamics of marine sands: a manual for practical applications*. Telford. Publication Title: Dynamics of marine sands: a manual for practical applications.

Stark, N., Mewis, P., Reeve, B., Florence, M., Piller, J., & Simon, J. (2022). Vertical pore pressure variations and geotechnical sediment properties at a sandy beach. *Coastal Engineering*, *172*, 104058, https://doi.org/10.1016/j.coastaleng.2021.104058.

Sumer, B. M. & Fredsøe, J. (2002). *The Mechanics of Scour in the Marine Environment*, volume 17. WORLD SCIENTIFIC. Series Title: Advanced Series on Ocean Engineering Publication Title: Coastal Engineering Issue: 1 ISSN: 03783839.

Sumer, B. M., Guner, H. A. A., Hansen, N. M., Fuhrman, D. R., & Fredsøe, J. (2013). Laboratory observations of flow and sediment transport induced by plunging regular waves. *Journal of Geophysical Research: Oceans*, *118*(11), 6161–6182, https://doi.org/10.1002/2013JC009324.

Sumer, B. M., Sen, M. B., Karagali, I., Ceren, B., Fredsøe, J., Sottile, M., Zilioli, L., & Fuhrman, D. R. (2011). Flow and sediment transport induced by a plunging solitary wave. *Journal of Geophysical Research: Oceans*, *116*(1), 1–15, https://doi.org/10.1029/2010JC006435.

Tazaki, T., Harada, E., & Gotoh, H. (2022). Numerical investigation of sediment transport mechanism under breaking waves by DEM-MPS coupling scheme. *Coastal Engineering*, *175*, 104146, https://doi.org/10.1016/j.coastaleng.2022.104146.

Ting, F. C. K. & Kirby, J. T. (1994). Observation of undertow and turbulence in a laboratory surf zone. *Coastal Engineering*, *24*(1-2), 51–80, https://doi.org/10.1016/0378-3839(94)90026-4.

Torres-Freyermuth, A., Puleo, J. A., & Pokrajac, D. (2013). Modeling swash-zone hydrodynamics and shear stresses on planar slopes using Reynolds-Averaged Navier-Stokes equations. *Journal of Geophysical Research: Oceans*, *118*(2), 1019–1033, https://doi.org/10.1002/jgrc.20074.

Turner, I. L. & Nielsen, P. (1997). Rapid water table fluctuations within the beach face: Implications for swash zone sediment mobility? *Coastal Engineering*, *32*(1), 45–59, https://doi.org/10.1016/s0378-3839(97)00015-x.

Ubbink, O. (1997). *Numerical prediction of two fluid systems with sharp interfaces*. PhD thesis, Imperial College of Science, Technology and Medicine, London. Issue: January 1997 ISBN: 9781605586397 ISSN: 00219991.

Van Bergeijk, V. (2022). *Over the dike top: modelling the hydraulic load of overtopping waves including transitions for dike cover erosion*. PhD thesis, University of Twente, Enschede, The Netherlands. https://doi.org/10.3990/1.9789036553414, Publication Title: PhD Thesis, University of Twente, Water Engineering and Management, Enschede, The Netherlands ISBN: 9789036553414.

Van der A, D. A., Van der Zanden, J., O'Donoghue, T., Hurther, D., Cáceres, I., McLelland, S. J., & Ribberink, J. S. (2017). Large-scale laboratory study of breaking wave hydrodynamics over a fixed bar. *Journal of Geophysical Research: Oceans*, *122*(4), 3287–3310, https://doi.org/10.1002/2016JC012072.

Van der Werf, J., Dionísio António, S., Kranenborg, J., Vermeulen, B., Campmans, G., van der Zanden, J., Ribberink, J., Reniers, A., & Hulscher, S. (2019). Shaping The Beach: Cross-Shore Sand Transport in the Swash Zone. *Coastal Structures 2019*, (pp. 851–861)., https://doi.org/10.18451/978-3-939230-64-9_080.

Van der Zanden, J., Alsina, J. M., Cáceres, I., Buijsrogge, R. H., & Ribberink, J. S. (2015). Bed level motions and sheet flow processes in the swash zone: Observations with a new conductivity-based concentration measuring technique (CCM+). *Coastal Engineering*, *105*, 47–65, https://doi.org/10.1016/j.coastaleng.2015.08.009.

Van der Zanden, J., Cáceres, I., Eichentopf, S., Ribberink, J. S., Van der Werf, J. J., & Alsina, J. M. (2019a). Sand transport processes and bed level changes induced by two alternating laboratory swash events. *Coastal Engineering*, *152*, 103519, https://doi.org/10.1016/j.coastaleng.2019.103519.

Van der Zanden, J., Van der A, D. A., Hurther, D., Cáceres, I., O'Donoghue, T., & Ribberink, J. S. (2016). Near-bed hydrodynamics and turbulence below a large-scale plunging breaking wave over a mobile barred bed profile. *Journal of Geophysical Research: Oceans*, *121*(8), 6482–6506, https://doi.org/10.1002/2016JC011909.

Van der Zanden, J., Van der A, D. A., Thorne, P. D., O'Donoghue, T., & Ribberink, J. S. (2019b). Sand suspension and fluxes by wave groups and equivalent monochromatic waves. *Continental Shelf Research*, *179*, 85–104, https://doi.org/10.1016/j.csr.2019.04.005.

Van Gent, M. R. A. (1995). Porous Flow through Rubble-Mound Material. *Journal of Waterway, Port, Coastal, and Ocean Engineering*, *121*(3), 176–181, https://doi.org/10.1061/(asce)0733-950x(1995)121:3(176).

Van Rijn, L. C. (2007). Unified View of Sediment Transport by Currents and Waves. II: Suspended Transport. *Journal of Hydraulic Engineering*, *133*(6), 668–689, https://doi.org/10.1061/(asce)0733-9429(2007)133:6(668).

Van Rijn, L. C., Ribberink, J. S., Van der Werf, J., & Walstra, D. J. R. (2013). Coastal sediment dynamics: recent advances and future research needs. *Journal of Hydraulic Research*, *51*(5), 475–493, https://doi.org/10.1080/00221686.2013.849297.

Van Rijn, L. C., Tonnon, P. K., & Walstra, D. J. R. (2011). Numerical modelling of erosion and accretion of plane sloping beaches at different scales. *Coastal Engineering*, *58*(7), 637–655, https://doi.org/10.1016/j.coastaleng.2011.01.009.

Verruijt, A. (1969). Elastic storage of aquifers. In *Flow through porous media* (pp. 331–376). Academic Press.

Walstra, D. J. R., Van Rijn, L. C., Van Ormondt, M., Brière, C., & Talmon, A. M. (2007). The Effects of Bed Slope and Wave Skewness on Sediment Transport and Morphology. In *Coastal Sediments '07*, volume 40926 (pp. 137–150). Reston, VA: American Society of Civil Engineers. Issue: January 2016.

Wilcox, D. C. (1988). Reassessment of the scale-determining equation for advanced turbulence models. *AIAA Journal*, *26*(11), 1299–1310, https://doi.org/10.2514/3.10041.

Wilcox, D. C. (2006). *Turbulence Modeling for CFD (3rd edition)*. DWC Industries, Inc.

Wilcox, D. C. (2008). Formulation of the k-ω turbulence model revisited. *AIAA Journal*, *46*(11), 2823–2838, https://doi.org/10.2514/1.36541.

Wright, L. D. & Short, A. D. (1984). Morphodynamic variability of surf zones and beaches: A synthesis. *Marine Geology*, *56*(1-4), 93–118, https://doi.org/10.1016/0025-3227(84)90008-2.

Xia, H. & Kamlah, M. (2022). Modelling Droplet Evaporation with an Improved Coupled Level Set and Volume of Fluid (i-CLSVoF) Framework. *Proceedings of the World Congress on Mechanical, Chemical, and Material Engineering*, https://doi.org/10.11159/htff22.127.

Yamamoto, T., Koning, H. L., Sellmeijer, H., & Van Hijum, E. V. (1978). On the response of a poro-elastic bed to water waves. *Journal of Fluid Mechanics*, *87*(1), 193–206, https://doi.org/10.1017/S0022112078003006.

Young, Y. L., Xiao, H., & Maddux, T. (2010). Hydro- and morpho-dynamic modeling of breaking solitary waves over a fine sand beach. Part I: Experimental study. *Marine Geology*, *269*(3-4), 107–118, https://doi.org/10.1016/j.margeo.2009.12.009.

Zhou, Z., Hsu, T. J., Cox, D., & Liu, X. (2017). Large-eddy simulation of wave-breaking induced turbulent coherent structures and suspended sediment transport on a barred beach. *Journal of Geophysical Research: Oceans*, *122*(1), 207–235, https://doi.org/10.1002/2016JC011884.

Zhu, F. & Dodd, N. (2015). The morphodynamics of a swash event on an erodible beach. *Journal of Fluid Mechanics*, *762*, 110–140, https://doi.org/10.1017/jfm.2014.610.

Zhu, F. & Dodd, N. (2020). Swash zone morphodynamic modelling including sediment entrained by bore-generated turbulence. *Advances in Water Resources*, *146*, 103756, https://doi.org/10.1016/j.advwatres.2020.103756.

Zyserman, J. A. & Fredsøe, J. (1994). Data Analysis of Bed Concentration of Suspended Sediment. *Journal of Hydraulic Engineering*, *120*(9), 1021–1042, https://doi.org/10.1061/(asce)0733-9429(1994)120:9(1021).

List of common symbols

$\cdot_{BC}$	Quantity on boundary	[-]
$\cdot_{C}$	Quantity in cell	[-]
$\cdot_{N}$	Quantity in neighbour cell	[-]
$\cdot_{Ng}$	Quantity in neighbour ghost cell	[-]
$\cdot_{P}$	Quantity in parent cell	[-]
$\bar{\cdot}$	Ensamble average	[-]
$< . >_T$	Average over time interval T	[-]
a	calibration coefficient	$[\mathrm{sm}^{-2}]$
A	Reference height	[m]
c	Sediment concentration	[-]
c	Sediment concentration	$[\mathrm{Kg\,m}^{-3}]$
C	Depth-integrated	$[\mathrm{Kg\,m}^{-2}]$
c_0	Reference concentration	$[\mathrm{m}^3\mathrm{m}^{-3}]$
d	Particle diameter	[m]
D	Domain depth	[m]
D_{50}	Median grain size	[m]
e	error	[-]
F	Sediment flux	$[\mathrm{Kg\,m}^{-1}\mathrm{s}^{-1}]$
F_f	Flux of passive scalar over face f	$[\mathrm{s}^{-1}]$
F_U	Uniform sediment flux	$[\mathrm{Kg\,m}^{-1}\mathrm{s}^{-1}]$
g	Gravitational acceleration	$[\mathrm{ms}^{-1}]$
H	Wave height	[m]
h	Water depth	[m]
h_0	Initial deep water depth	[m]
$\bar{h}$	Mean water depth	[m]
I_{ero}	Integral erosion volume	$[\mathrm{m}^2]$
I_{dep}	Integral deposition volume	$[\mathrm{m}^2]$
I_{dz}	Integral bed level change	$[\mathrm{m}^2]$
k	Turbulent kinetic energy	$[\mathrm{m}^2\mathrm{s}^{-2}]$
k_c	Hydraulic conductivity	$[\mathrm{ms}^{-1}]$
K	Diffusion coefficient	$[\mathrm{m}^2\mathrm{s}^{-1}]$
K	Eddy viscosity	$[\mathrm{m}^2\mathrm{s}^{-1}]$
$\tilde{k}_j$	Wave number	$[\mathrm{m}^{-1}]$
K_N	Nikuradse roughness height	[m]
L	Domain length	[m]
n	Porosity	[-]

$\boldsymbol{n}$	Normal vector	[-]
p^*	Excess pressure over hydrostatic potential	[Pa]
p_j^*	Complex pressure component j	[Pa]
$\bar{p}$	Hydrostatic pressure	[Pa]
$\tilde{p}$	Dynamic pressure in excess of hydrostatic	[Pa]
Pe	Cell Peclet number	[-]
Pe_L	Peclet number	[-]
R^2	Pearson correlation coefficient	[-]
s	Specific gravity of sand	[-]
S_f	Face area	[m]
S_{ij}	mean strain rate tensor	[s^{-1}]
t	time	[s]
T	Time interval	[s]
T_{gr}	Wave group period	[s]
T_r	Wave repetition period	[s]
T_s	Short-wave period	[s]
$\boldsymbol{u}$	velocity	[ms^{-1}]
U	Depth-averaged velocity	[ms^{-1}]
U_c	Effective transport velocity	[ms^{-1}]
u_c	Cell velocity normal to boundary face	[ms^{-1}]
u_x	Cross-shore velocity	[ms^{-1}]
u_i	Velocity component i	[ms^{-1}]
u_i'	Fluctuating velocity component i	[ms^{-1}]
u_*	Friction velocity	[ms^{-1}]
V	Cell volume	[m^2]
V_i^*	Weighted volume of bed level change in cell i	[m^3]
V_i	Volume of bed level change in cell i	[m^3]
w	Interpolation weights	[-]
w_l	Linear interpolation weights	[-]
w_s	Settling velocity	[ms^{-1}]
x	Cross-shore coordinate	[m]
x_i	Cross-shore coordinate i	[m]
y	Vertical coordinate	[m]
y_a	Reference height	[m]
y_b	Bed level	[m]
z	Vertical coordinate	[m]
z	Distance above bed	[m]
$\hat{z}$	Downwards vertical coordinate relative to initial bed	[m]
z_a	Reference height	[m]
z_b	Bed level	[m]

α	VoF volume fraction field	[-]
β	Compressibility of pore fluid	[-]
γ	Passive scalar	[-]
γ	Pore fluid weight	$[\mathrm{Kg\,m^{-2}s^{-2}}]$
Δ	cell width normal to boundary face	[m]
Δ_F	Flux difference	$[\mathrm{Kg\,m^{-1}s^{-1}}]$
Δ_U	Velocity difference	$[\mathrm{m}s^{-1}]$
Δz_b	Bed level change relative to initial morphology	[m]
δ_{ij}	Kronecker delta	[-]
η	Deviation from initial water level	[m]
η	Surface elevation	[m]
λ_1	Turbulence limiter	[-]
λ_2	Turbulence limiter	[-]
θ	Shields number	[-]
θ'	Pressure-modified Shields number	[-]
μ	Dynamic molecular viscosity	$[\mathrm{Kg\ m^{-1}s^{-1}}]$
ν	Kinematic viscosity	$[\mathrm{m^2s^{-1}}]$
ν	Poisson ratio	[-]
ν_t	Eddy viscosity	$[\mathrm{m^2s^{-1}}]$
ρ	Density	$[\mathrm{Kg\,m^{-3}}]$
ρ	Water density	$[\mathrm{Kg\,m^{-3}}]$
ρ_s	Sand density	$[\mathrm{Kg\,m^{-3}}]$
ρ_w	Water density	$[\mathrm{Kg\,m^{-3}}]$
τ	Reynolds stress	$[\mathrm{m^2s^{-2}}]$
τ_b	Bed shear stress	[Pa]
ψ	Scheme weights	[-]
ω	Specific rate of dissipation	$[\mathrm{s^{-1}}]$
ω_j	Angular frequency	$[\mathrm{s^{-1}}]$

List of publications

Peer-reviewed journal publications

- **Kranenborg, J.W.M.**, Campmans, G.H.P., Jacobsen, N.G., van der Werf, J.J., Reniers, A.J.H.M., & Hulscher, S.J.M.H. (2022). Depth-Resolved Modelling of Intra-Swash Morphodynamics Induced by Solitary Waves. Journal of marine science and engineering, 10(9), 1-23. [1175].

Conference papers and abstracts

- **Kranenborg, J.W.M.**, Campmans, G.H.P., van der Werf, J.J., Jacobsen, N.G., McCall, R.T., Reniers, A.J.H.M., & Hulscher, S.J.M.H. (2019). Numerical modelling of the swash zone. 61-61. Abstract from NCK-DAYS 2019, Enkhuizen, Netherlands.

- van der Werf, J.J, Dionisio Antonio, S., **Kranenborg, J.W.M.**, Vermeulen, B., Campmans, G., van der Zanden, J., Ribberink, J., Reniers, A.J.H.M., & Hulscher, S.J.M.H. (2019). Shaping The Beach: Cross-Shore Sand Transport in the Swash Zone. In N. Goseberg, & T. Schlurmann (Eds.), Coastal Structures 2019 Bundesanstalt für Wasserbau.

- **Kranenborg, J.W.M.** , Campmans, G.H.P., van der Werf, J.J., Reniers, A.J.H.M., & Hulscher, S.J.M.H. (2019). Depth-Resolving vs Depth-Averaged Modelling of Swash Zone Hydrodynamics. In N. Goseberg, & T. Schlurmann (Eds.), Coastal Structures 2019 Bundesanstalt für Wasserbau.

- **Kranenborg, J.W.M.**, Campmans, G.H.P., Jacobsen, N.G., van der Werf, J.J., Reniers, A.J.H.M., & Hulscher, S.J.M.H. (2020). A depth-resolving model for intraswash hydrodynamics and sediment transport. 55-55. Abstract from NCK Days 2020, Texel, Netherlands.

- **Kranenborg, J.W.M.**, Campmans, G.H.P., Jacobsen, N.G., van der Werf, J.J., McCall, R.T., Reniers, A.J.H.M., & Hulscher, S.J.M.H. (2020). Rans modelling of cross-shore sediment transport and morphodynamics in the Swash-zone. In P. Lynett (Ed.), Proceedings of virtual Conference on Coastal

Engineering, 2020 (International Conference Proceedings of Coastal Engineering; Vol. 36).

- **Kranenborg, J.W.M.**, Pauli, T., Dionisio Antonio, S., Campmans, G.H.P., Jacobsen, N.G., van der Werf, J.J., Reniers, A.J.H.M., & Hulscher, S.J.M.H. (2021). Large-scale laboratory measurements of the pore pressure response to bichromatic waves in the swash zone. 31. Abstract from NCK Days 2021, Netherlands.

- **Kranenborg, J.W.M.**, Pauli, T., Dionisio Antonio, S., Jacobsen, N.G., van der Werf, J.J., McCall, R.T., Campmans, G.H.P., Reniers, A.J.H.M., Wijnberg, K.M., & Hulscher, S.J.M.H. (2021). Laboratory measurements and modelling of pore pressures in the swash zone. 31. Abstract from Coastal Dynamics Conference 2021, 28 June-2 July 2021, Delft University of Technology.

- **Kranenborg, J.W.M.**, Campmans, G.H.P., van der Werf, J.J., Jacobsen, N.G., McCall, R.T., Reniers, A.J.H.M., & Hulscher, S.J.M.H. (2022). Depth-resolved modelling of water and sediment fluxes in the swash zone. 33-33. Abstract from NCK Days 2022, Enschede, Netherlands.

- **Kranenborg, J.W.M.**, Campmans, G.H.P., van der Werf, J.J., McCall, R.T., Jacobsen, N.G., Reniers, A.J.H.M., & Hulscher, S.J.M.H. (2022). Depth-resolved modelling of suspended sediment in the surf and swash zones. In M. Ortega-Sánchez (Ed.), Proceedings 39th IAHR World Congress, 19-24 June 2022, Granada, Spain IAHR.

- **Kranenborg, J.W.M.**, McCall, R.T., Reniers, A.J.H.M., Campmans, G.H.P., van der Werf, J.J., & Hulscher, S.J.M.H. (2022). The Importance of Vertical Structures in Determining the Cross-Shore Flux of Suspended Sediment in the Swash Zone. n A. I. Stamou, & V. Tsihrintzis (Eds.), 7th IAHR Europe Congress: Innovative water management in a changing climate: September 7-9, 2022, Athens, Greece: Abstract book (pp. 108-109).

- **Kranenborg, J.W.M.**, Campmans, G.H.P., van der Werf, J.J., McCall, R.T., Reniers, A.J.H.M., & Hulscher, S.J.M.H. (2022). Depth-resolved modelling of sediment fluxes under bichromatic waves in the swash zone. Abstract from 38th International Conference on Coastal Engineering, ICCE 2022, Sydney, Australia.

Other contributions

- **Kranenborg J.W.M.** Campmans, G.H.P., van der Werf, J.J., McCall, R.T., Reniers, A.J.H.M., & Hulscher, S.J.M.H. (2022). Modelling sediment transport under breaking waves on the beach. Burgers Symposium (2022), Lunteren, The Netherlands.

About the author

Joost Willem Martijn Kranenborg was born in Utrecht on 22 April. After living in Tilburg for ten years, he moved to Uppsala in Sweden, where he graduated from Rosendalsgymnasiet in 2013. The same year, Joost started his studies in Engineering physics at the faculty of Engineering at Lund University. During 2017, He attended a semester at the Technical University of Munich as an erasmus exchange student. In June 2018 he concluded his Msc thesis at the centre for mathematical sciences on the topic of parallel asynchronous time integration of coupled systems.

In september 2018 Joost moved back to the Netherlands to pursue a Phd at the Marine and Fluvial Systems group at the University of Twente. Here, he used a combination of detailed fluid dynamics modelling techniques and laboratory experiments to study how sand is transported in the swash zone.

Joost defended his thesis on 29 June, 2023 at the University of Twente in Enschede.

The presented research in this thesis was carried out at the Water Engineering and Management (WEM) department, Civil Engineering, University of Twente, The Netherlands.

This work is part of the research programme Shaping the beach, with project number 16130, which is financed by the Netherlands Organisation for Scientific Research (NWO) with an in-kind contribution by Deltares.